


January 2012

Synthesis and Characterization of Nanocomposites for Electrochemical Capacitors

Farah Alvi

University of South Florida, falvi@mail.usf.edu

Follow this and additional works at: <http://scholarcommons.usf.edu/etd>

 Part of the [American Studies Commons](#), [Nanoscience and Nanotechnology Commons](#), and the [Oil, Gas, and Energy Commons](#)

Scholar Commons Citation

Alvi, Farah, "Synthesis and Characterization of Nanocomposites for Electrochemical Capacitors" (2012). *Graduate Theses and Dissertations*.

<http://scholarcommons.usf.edu/etd/3948>

This Dissertation is brought to you for free and open access by the Graduate School at Scholar Commons. It has been accepted for inclusion in Graduate Theses and Dissertations by an authorized administrator of Scholar Commons. For more information, please contact scholarcommons@usf.edu.

Synthesis and Characterization of Nanocomposites for Electrochemical Capacitors

by

Farah Alvi

A dissertation submitted in partial fulfillment
of the requirements for the degree of
Doctor of Philosophy
Department of Electrical Engineering
College of Engineering
University of South Florida

Co-Major Professor: Ashok Kumar, Ph.D.
Co-Major Professor: Elias K. Stefanakos, Ph.D.
Yogi Goswami, Ph.D.
Andrew Hoff, Ph.D.
Jing Wang, Ph.D.
Abdul Malik, Ph.D.
Manoj K. Ram, Ph.D.

Date of Approval:
February 20, 2012

Keywords: Supercapacitor, Conducting Polymer, Graphene, Electrochemistry, Columbic Efficiency

Copyright © 2012, Farah Alvi

DEDICATION

This dissertation is dedicated to my dearest and respected uncle Dr Ashraf Ali for his ever incredible support and sincere guidance. For my mother Bushira Aslam and in the memory of my late Father Muhammad Aslam who supported me all the way since the beginning of my studies, and has been a great source of motivation and inspiration throughout my PhD. For my loving daughter Sahab Alvi for all her cherished love and whose presence gave me the strength and joy to culminate my dream. Finally, this dissertation is dedicated to all those who believe in the miracle of learning.

ACKNOWLEDGMENTS

First of all I would like to express my deep gratitude and sincere thanks to my major professor Dr. Ashok Kumar, Director of NREC (Nanotechnology Research & Education Center) at the University of South Florida, who has supported me fully, with all guidance, facilities, materials, insights, and infrastructure to successfully accomplish the challenges in my research. I am forever indebted and thankful to Professor Kumar for giving me this excellent opportunity. I wish to express my sincere appreciation to my Co-Major Professor Dr. Elias Stefanakos, and my committee members Dr. Yogi Goswami, Dr. Andrew Hoff, Dr. Jing Wang, and Dr. Abdul Malik for their valuable time, encouragement and professional aid to me.

I owe special thanks to Dr. Manoj K. Ram. I will never forget his patience, accessibility, guidance and care for me. Thank you to Dr. Muhammad Rahman for serving as the chair of my doctoral defense. I am also thankful to the Materials group: H. Gomez, P. Villaba, M. Ladanvo, P.A. Basnayak, S. Ketkar, A. Zama, Deepak, the NREC staff, especially Robert Tufts and Dr. Yusuf Emirov, and the Electrical Engineering department staff, and many other people, for all of their sincere support. I also owe my loving and sincere thanks to my brothers for their sincere mentorship, and my aunt and my relatives for all of their support, encouragement, patience and love during my Ph.D. The financial support for this dissertation work came from the NSF research award CMMI # 0728100 and the NSF research award ECCS # 1066643.

TABLE OF CONTENTS

LIST OF TABLES	iv
LIST OF FIGURES	v
ABSTRACT	x
CHAPTER 1: INTRODUCTION	1
1.1 Overview	1
1.2 History and Current Status of Supercapacitor	4
1.3 Energy Storage Principles of Supercapacitor	5
1.3.1 Electrical Double Layer Capacitor (EDLC).....	7
1.3.2 PseudoCapacitor	10
1.3.2.1 Types of Pseudocapacitors.....	13
1.3.3 Hybrid Capacitor	15
1.4 Electrode Materials for Supercapacitor	15
1.4.1 Activated Carbon	17
1.4.2 Carbon Aerogels	18
1.4.3 Carbon Nanotubes (CNTs).....	19
1.4.4 Transition Metal Oxides.....	20
1.4.5 Conducting Polymers.....	21
1.5 Target of Research	22
CHAPTER 2: AROMATIC BASED CONDUCTING POLYMER NANOCOMPOSITE FOR ELECTROCHEMICAL CAPACITOR	25
2.1 Introduction.....	25
2.2 Experimental Procedure	27
2.3 Materials	28
2.4 Synthesis Method	29
2.4.1 Chemical Polymerization Method	29
2.4.2 Physical and Structural Characterization	30
2.4.2.1 Transmission Electron Microscopy (TEM)	31
2.4.2.2 Scanning Electron Microscopy (SEM).....	33
2.4.2.3 X-Ray Diffraction(XRD).....	35
2.4.2.4 FTIR Spectroscopy.....	37
2.4.2.5 Raman Spectroscopy	39
2.5 Electrode Preparation and Cell Assembly of Supercapacitor.....	41
2.6 Electrochemical Characterization	43
2.6.1 Cyclic Voltammetry(CV).....	43

2.6.2 Electrochemical Impedance Spectroscopy (EIS)	46
2.6.3 Galvanostatic Charge & Discharge	49
2.7 Summary.....	53
CHAPTER 3: INFLUENCE OF GRAPHENE COMPOSITION ON G-PANI BASED ELECTROCHEMICAL CAPACITOR.....	54
3.1 Introduction.....	54
3.2 Experiment.....	55
3.3 Structural Characterization	56
3.3.1 Scanning Electron Microscopy (SEM)	56
3.3.2 Transmission Electron Microscopy (TEM).....	57
3.3.3 XRD	58
3.3.4 Raman Spectroscopy.....	59
3.4 Electrochemical Evaluation	60
3.4.1 Electrode Preparation.....	60
3.4.2 Capacitance Evaluation of G-PANI Films with Different Composition of Graphene.....	61
3.4.2.1 CV	61
3.4.2.2 Four Probe Measurement.....	68
3.4.2.3 Ragone Plot.....	70
3.4.2.4 Electrochemical Impedance Spectroscopy (EIS)	71
3.5 Capacitance Evaluation with Different Thicknesses of G-PANI Film	74
3.5.1 Electrochemical Impedance Spectroscopy (EIS)	76
3.6 Summary.....	81
CHAPTER 4: INFLUENCES OF ELECTROLYTES AND SOLVENTS ON G- PANI BASED ELECTROCHEMICAL CAPACITOR.....	82
4.1 Capacitance Evaluation with Different Electrolytes for G-PANI Film	84
4.1.1 Electrochemical Impedance Spectroscopy (EIS)	92
4.2 Influence of Electrolyte Concentration on G-CPs Film	93
4.3 Capacitance Evaluation of G-PANI Film with Different Solvents.....	98
4.4 Summary.....	106
CHAPTER 5: HETEROCYCLIC BASED CONDUCTING POLYMER NANOCOMPOSITE FOR ELECTROCHEMICAL CAPACITOR.....	107
5.1 Experimental.....	108
5.1.1 Synthesis of G-PTh Nanocomposite Material.....	108
5.1.2 Structural Characterization of G-PTh Films	110
5.1.2.1 Scanning Electron Microscope (SEM) and Transmission Electron Microscope (TEM) Studies	110
5.1.2.2 Raman Studies.....	113
5.1.2.3 FTIR	114
5.1.2.4 X-Ray Diffraction.....	115
5.1.3 Electrochemical Measurements.....	116
5.1.3.1 Electrode Preparation and Electrochemical Setup	116

5.1.3.2 Capacitance Evaluation of G-PTh Film.....	116
5.1.3.3 Impedance Study.....	123
5.2 Summary.....	125
CHAPTER 6: EFFECT OF SUBSTITUTES IN HETEROCYCLIC BASED CONDUCTING POLYMER.....	
6.1 Synthesis of G-PEDOT	127
6.2 Results and Discussion	129
6.2.1 Characterization of G-PEDOT	129
6.2.2 FTIR.....	131
6.2.3 Raman Spectroscopy.....	132
6.2.4 XRD	133
6.3 Electrochemical Measurements	134
6.3.1 Electrode Fabrication	134
6.3.2 Capacitance Evaluation of G-PEDOT Electrodes	134
6.4 Summary.....	143
CHAPTER 7: CONCLUSION.....	
7.1 Electrochemical Capacitor.....	144
7.2 Future Work and Limitations.....	147
REFERENCES	149
APPENDIX A: PERMISSIONS	159

LIST OF TABLES

Table 1. Detailed parametric comparison of capacitor, supercapacitor and battery	5
Table 2. Advantages and disadvantages of electrical double layer capacitor and pseudocapacitor	12
Table 3. List of chemicals used in this dissertation.....	28
Table 4. Diffusion coefficients of polyaniline nanocomposites.	45
Table 5. Specific capacitance for PANI, graphene, G-PANI (10:90, 50:50, 90:10) nanocomposites.....	63
Table 6. Conductivity of PANI, G-PANI (10:90, 50:50, 90:10) nanocomposites.....	69
Table 7. Specific capacitance versus G-PANI (50:50) thickness at a scan rate of 5 mV/s	75
Table 8. Specific capacitance comparison of G-PANI (50:50) nanocomposites in aqueous, organic and IL at scan rate of 5 mV/s.....	86
Table 9. Specific capacitance comparison of G-PANI (50:50) nanocomposites in (H ₂ SO ₄) concentrations (0.1M, 2M and 4M) at 5 mV/s.....	95

LIST OF FIGURES

Figure 1. Ragone plot comparison of several electrical energy storage devices with combustion engine	2
Figure 2. Differences in the configuration of the three types of capacitor.....	3
Figure 3. Electrochemical double layer energy storage mechanism.	8
Figure 4. Electrochemical model describing the extension of double layers from the electrode surface into bulk of liquid electrolyte	9
Figure 5. Difference in electric double layer and pseudocapacitance	11
Figure 6. Types of supercapacitor	16
Figure 7. Schematic of carbon family in 0-dimensional fullerene, 1-dimensional carbon nanotube, 2-dimensional graphene, 3-dimensional graphite.	17
Figure 8. Chemical structure of polyaniline consists of quinoid and benzenoid rings.	26
Figure 9. Flow diagram of the experimental procedure	27
Figure 10. Schematic of polyaniline nanocomposites materials	30
Figure 11. TEM images of the (a) G-PANI (b) ZnO-PANI (c) G/ZnO-PANI (d) RuO ₂ -PANI nanocomposites.....	33
Figure 12. SEM images of the (a) G-PANI (b) ZnO-PANI (c) G/ZnO-PANI (d) RuO ₂ -PANI nanocomposites.....	34
Figure 13. XRD pattern of the G-PANI, ZnO-PANI G/ZnO-PANI, RuO ₂ -PANI nanocomposites	37
Figure 14. FTIR spectra of the G-PANI, ZnO-PANI,G/ZnO-PANI, RuO ₂ -PANI nanocomposites	39
Figure 15. Raman spectra of the G-PANI, ZnO-PANI, G/ZnO-PANI, RuO ₂ -PANI nanocomposites	41

Figure 16. Schematic of supercapacitor electrodes for electrochemical measurements	42
Figure 17. CV responses of (a) ZnO-PANI (b) G/ZnO-PANI (c) RuO ₂ -PANI (d) G-PANI at scan rates (5, 20, 50,100 mV/s) (e) Scan rate versus specific capacitance.....	47
Figure 18. EIS analysis of (a) ZnO-PANI, G/ZnO-PANI, RuO ₂ -PANI, G-PANI and (b) G/ZnO-PANI, RuO ₂ -PANI , G-PANI.	49
Figure 19. (a) Charging & discharging profile and (b) cycle numbers versus specific capacitance of polyaniline nanocomposites.....	52
Figure 20. SEM images of (a) PANI (b) graphene and (c) G-PANI10 (d) G-PANI50 (e) G-PANI90	57
Figure 21. TEM images of (a) graphene (b) PANI (c) G-PANI10 (d) G-PANI50 (e) G-PANI90.....	58
Figure 22. XRD spectra of PANI, and G-PANI (10:90, 50:50, 90:10) nanocomposites.....	59
Figure 23. Raman spectra of PANI, and G-PANI (10:90, 50:50, 90:10) nanocomposites.....	60
Figure 24. (a) CV profile of PANI, graphene, and G-PANI (10:50:90) nanocomposites at 5mV/s and (b) CV profile of G-PANI (50:50) nanocomposites at 5, 20, 50 and 100mV/s	64
Figure 25. Specific capacitance versus scan rate (5, 20, 50,100) mV/s of G-PANI (10:50:90) nanocomposites.....	64
Figure 26. Charging-discharging response of PANI, graphene and G-PANI (10:90, 50:50, 90:10) nanocomposites.....	66
Figure 27. Columbic efficiency versus cycles number of G-PANI (10:90, 50:50, 90:10) nanocomposites	67
Figure 28. Specific capacitance versus cycle numbers of G-PANI (10:90, 50:50, 90:10) nanocomposites.	68
Figure 29. Conductivity versus specific capacitance for G-PANI (10, 50, 90) nanocomposites	70
Figure 30. Ragone plot for G-PANI (10,50,90) nanocomposites	71

Figure 31. Impedance spectra for (a) graphene, PANI, and G-PANI (10:90, 50:50, 90:10) (b) G-PANI (50:50), G-PANI (10:90) nanocomposites	73
Figure 32. (a) CV comparison of G-PANI50 of film thickness 10 μm , 30 μm and 50 μm at 5mV/s (b) CV profile of 30 μm film thickness at the scan rate of 10, 50 and 100 mV/s (c) Specific capacitance versus scan rate of G-PANI film of thickness 10, 30 and 50 μm	78
Figure 33. Charging-discharging curves for G-PANI50 of film thickness 10 μm , 30 μm and 50 μm	79
Figure 34. Columbic efficiency G-PANI50 film of thickness 10 μm , 30 μm and 50 μm	79
Figure 35. Impedance plots for G-PANI50 for film thickness of 10 μm , 30 μm and 50 μm	80
Figure 36. CV response of G-PANI50 film in (a) H_2SO_4 (b) LiClO_4 (c) IL (d) KOH (e) SC versus scan rate of G-PANI50 film in (a) H_2SO_4 (b) LiClO_4 (c) IL.....	87
Figure 37. Charging-discharging curves for G-PANI50 in H_2SO_4 , LiClO_4 and IL	89
Figure 38. Comparison of specific capacitance versus cycles numbers of H_2SO_4 , LiClO_4 and IL electrolytes.....	90
Figure 39. Columbic efficiency of acidic, organic and IL electrolytes.	90
Figure 40. Ragone plot of acidic, organic and IL electrolytes.	91
Figure 41. EIS analysis of acidic, organic and IL electrolytes.....	93
Figure 42. CV comparison of G-PANI film in 0.1M, 2M and 4M H_2SO_4 ; Specific capacitance versus scan rate in 0.1M, 2M and 4M H_2SO_4	96
Figure 43. Charging-discharging profile of G-PANI in 0.1M, 2M and 4M H_2SO_4	97
Figure 44. SEM results of G-PANI in (a) NMP (b) Nafion and (c) DMF.....	98
Figure 45. CV response of G-PANI in (a) NMP (b) Nafion and (c) DMF.....	101
Figure 46. Specific capacitance versus scan rate of G-PANI in NMP, nafion and DMF	102

Figure 47. Charging-discharging comparison of G-PANI films in NMP, nafion and DMF.....	102
Figure 48. Cycle's stability versus specific capacitance of NMP, nafion and DMF	103
Figure 49. Ragone plot of NMP, nafion and DMF	104
Figure 50. EIS analysis of G-PANI film in NMP, nafion and DMF	105
Figure 51. Schematic of chemically synthesized G-PTh nanocomposites	109
Figure 52. SEM images of (a) undoped (b) doped G-PTh nanocomposite... ..	112
Figure 53. (a) TEM (b) HRTEM and (c) SEAD images of G-PTh nanocomposite.....	112
Figure 54. Raman spectra of G-PTh nanocomposites	113
Figure 55. FTIR spectra of G-PTh nanocomposites.....	114
Figure 56. XRD plot of G-PTh nanocomposites.....	115
Figure 57. Current-voltage response of G-PTh nanocomposites in (a) 2MHCl (b) 2MH ₂ SO ₄ (c) LiClO ₄ (d) IL	118
Figure 58. Specific capacitance versus scan rates of G-PTh nanocomposites in (a) 2MHCl (b) 2MH ₂ SO ₄ (c) LiClO ₄ (d) IL.....	119
Figure 59. Charging-discharging profile of G-PTh nanocomposites in (a) 2MHCl (b) 2MH ₂ SO ₄ (c) LiClO ₄ (d) IL.....	120
Figure 60. Columbic efficiency versus number of cycles of G-PTh nanocomposites in (a) 2MHCl (b) 2MH ₂ SO ₄ (c) LiClO ₄ (d) IL.....	121
Figure 61. Specific capacitance versus scan rates of G-PTh nanocomposites in (a) 2MHCl (b) 2MH ₂ SO ₄ (c) LiClO ₄ (d) IL	122
Figure 62. Ragone plot of G-PTh nanocomposites in (a) 2MHCl (b) 2MH ₂ SO ₄ (c) LiClO ₄ (d) IL.....	123
Figure 63. Impedance analysis of G-PTh nanocomposites in (a) 2MHCl (b) 2MH ₂ SO ₄ (c) LiClO ₄ (d) IL.	124
Figure 64. Schematic of G-PEDOT nanocomposites.....	128
Figure 65. SEM images of undoped (a) and doped (b) G-PEDOT nanocomposites.	129

Figure 66. (a) TEM and (b) HRTEM images of G-PEDOT nanocomposites.....	130
Figure 67. FTIR spectra of G-PEDOT nanocomposites.....	131
Figure 68. Raman spectra of G-PEDOT nanocomposites.	132
Figure 69. XRD analysis of doped G-PEDOT nanocomposites.....	133
Figure 70. Current-voltage response of G-PEDOT nanocomposites in (a) 2MHCl (b) 2MH ₂ SO ₄ (c) LiClO ₄ (d) IL.	136
Figure 71. Scan rate versus specific capacitance of G-PEDOT nanocomposites for 5, 25, 50 and 100 mV/s	137
Figure 72. Charging-discharging of G-PEDOT nanocomposites in (a) 2MHCl (b) 2MH ₂ SO ₄ (c) LiClO ₄ (d) IL	139
Figure 73. CE% of G-PEDOT nanocomposites versus cycles numbers in (a) 2MHCl (b) 2MH ₂ SO ₄ (c) LiClO ₄ (d) IL	140
Figure 74. Specific capacitance versus scan rate of G-PEDOT nanocomposites in (a) 2MHCl (b) 2MH ₂ SO ₄ (c) LiClO ₄ (d) IL	140
Figure 75. Ragone plot of G-PEDOT nanocomposites in (a) 2MHCl (b) 2MH ₂ SO ₄ (c) LiClO ₄ (d) IL	141
Figure 76. Impedance analysis of G-PEDOT nanocomposites in (a) 2MHCl (b) 2MH ₂ SO ₄ (c) LiClO ₄ (d) IL	142

ABSTRACT

Presently there are deep concerns over the environmental consequences and the consumption of non-renewable energy sources, with the accelerated greenhouse effect, triggered enormous interest in the use of renewable energy sources e.g., solar, hydropower, wind and geothermal. However the intermittent nature of harvesting renewable energy sources has recently gained considerable attention in the alternative reliable, cost effective, and environmentally friendly energy storage devices. The supercapacitor and lithium ion batteries are considered more efficient electrical energy storage devices than conventional energy storage systems.

Both devices have many useful and important applications; they could be an excellent source for high power and high energy density, especially in portable electronic devices and Electrical Vehicles (EVs) or Hybrid Electrical Vehicles (HEVs). In order to make the efficient usage of these stationary energy storage devices, state of the art research on new and advanced electrode materials is highly needed. The aim of this dissertation is to investigate the scope of graphene/metal oxide-conducting polymer nanocomposites electrodes for light weight, high power density and wider voltage window supercapacitor devices.

The facile chemical polymerization approach was used to synthesize the aromatic and heterocyclic conducting polymer nanocomposites. For aromatic nanocomposites, several materials were synthesized includes ZnO-PANI, ZnO/G-PANI,

RuO₂-PANI and G-PANI. Subsequently these materials have been characterized by physical, structural techniques e.g Raman Spectroscopy, Fourier Transform Infrared Spectroscopy (FTIR), X-ray-Diffraction (XRD), Scanning Electron Microscopy (SEM), and Transmission Electron Microscopy (TEM). In addition to material characterization the prepared material was also characterized by electrochemical measurements using cyclic voltammetry (CV), electrochemical impedance spectroscopy (EIS), and chrono potentiometry for supercapacitor electrodes. Since graphene is a two-dimensional single-atom-thick sp² hybridized carbon structure due to its extraordinary characteristic, high electrical conductivity, chemical stability and large theoretical surface area (over 2600 m² g⁻¹) has gained immense interest in the future generation of renewable energy devices. Therefore, among all aromatic based nanocomposites, the Graphene-Polyaniline (G-PANI) rendered promisingly high specific capacitance around 440 F/g with the excellent cyclic stability. The higher specific capacitance of G-PANI might be due to the high conductivity and superior electrochemical properties of graphene in G-PANI nanocomposites.

However, besides the G-PANI, other aromatic nanocomposites e.g., RuO₂-PANI, ZnO-PANI and G/ZnO-PANI also showed the potential of low cost and flexible supercapacitor electrodes with the reasonably good specific capacitance as 360 F/g, 300 F/g, and 275 F/g. We have further investigated the role of conductivity by adding different amount of graphene in G-PANI nanocomposites to optimize device performance with the specific capacitance and columbic efficiency of 440 F/g and 90% respectively.

Further the other important parameters, relate with the electrode thickness, type of electrolytes, concentration of electrolytes and the effect of the solvent has also been studied to achieve the overall performance and reliability of the device. Moreover, in order to have the comprehensive study of conducting polymer besides the aromatic conducting polymer the heterocyclic polymers e.g., polythiophene and poly (3, 4-ethylenedioxythiophenes) (PEDOT) nanocomposites were studied at length to evaluate their role for the cost effective, large surface area and flexible green energy storage devices and has shown great prospects for commercial application. Therefore, G-Cps nanocomposites have proved to be a promising electrode material choice to facilitate the ionic diffusion and contact of the electrolytes to improve the specific capacitance and performance of the device.

CHAPTER 1: INTRODUCTION

1.1 Overview

The growing global energy crisis over the past two decades is, due to the high cost of materials depletion of natural resources, and severe ecological and environmental concerns based on the consumption of fossil fuels, has triggered the keen interest in the development of alternative for energy production. The critical role of energy storage devices in high power energy related applications, made it indispensable to meet the future energy necessities by looking into the alternative options for reliable, low cost, energy storage devices.

The most common electrical energy storage devices are batteries, fuel cells, and supercapacitors. The electrical energy storage and delivery mechanism in batteries and fuel cells depends on the conversion of chemical energy into electrical energy. Unlike batteries, energy storage in supercapacitors, also called electrochemical capacitor (EC), depends on the formation of electric double layers at the interface of the electrode and electrolytes. Comparison among the energy storage devices can be well understood by examining the energy density and power density of the devices, as described in the Ragone plot as shown in Figure 1 [1].

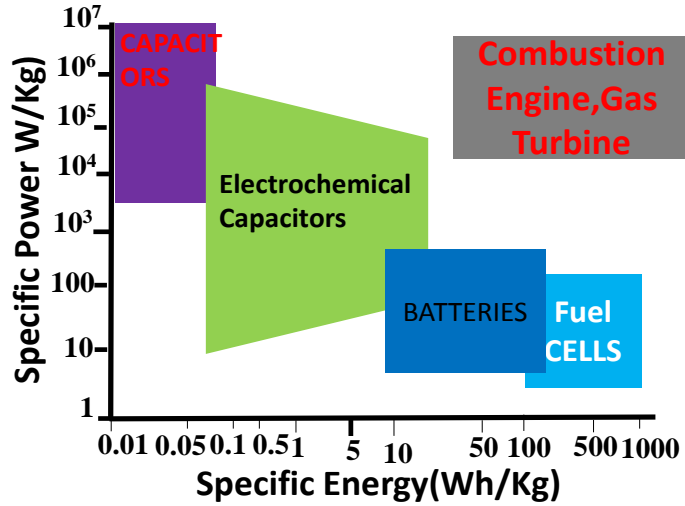


Figure 1. Ragone plot comparison of several electrical energy storage devices with combustion engine. (Adapted from [1])

Up to date there are three main types of capacitors that are widely known: i) Electrostatic capacitor ii) Electrolytic capacitor and iii) Electrochemical capacitor (EC). All types of capacitors perform the basic common, function to store stationary electrical energy [2]. The electrostatic capacitor is comprised of two metallic plates separated physically by an insulating medium e.g., air or ceramic. The charge starts to build up across the two plates when voltage is applied to these plates, one plate is given a positive and, the other is given the negative potential. Electrostatic capacitors have been for nearly a century. Capacitance in the electrostatic capacitor is usually in the order of pico and nano farads expressed in equation 1[2].

$$C = \frac{\Delta Q}{\Delta V} \quad (1)$$

The second generation of capacitor is named electrolytic capacitor which is available at large scale commercially. The assembly of electrolytic capacitor is quite

different from electrostatic capacitor. It consists of two electrodes one is made of a metallic plate, either aluminum or tantalum, and the other electrode is comprised of a conducting liquid electrolyte, which helps in polarization during the charging process [3]. A remarkably thin metal oxide layer is introduced e.g., Al_2O_3 between two electrodes in the electrolytic capacitor to improve the retention of charge for a reasonably longer time. The capacitance in the electrolytic capacitor is comparatively higher than in the electrostatic capacitor which is in the range of milli farad [3, 4].

The third generation of capacitor which has shown promising trend in the overall performance of the device, is known as the electric double layer capacitor (EDLC). In EDLC the carbon is used as the electrode material for both the anode and cathode encapsulated with organic or aqueous electrolytes. Differences in the configuration of all three types of capacitor are given in figure 2 [2, 5, 6].

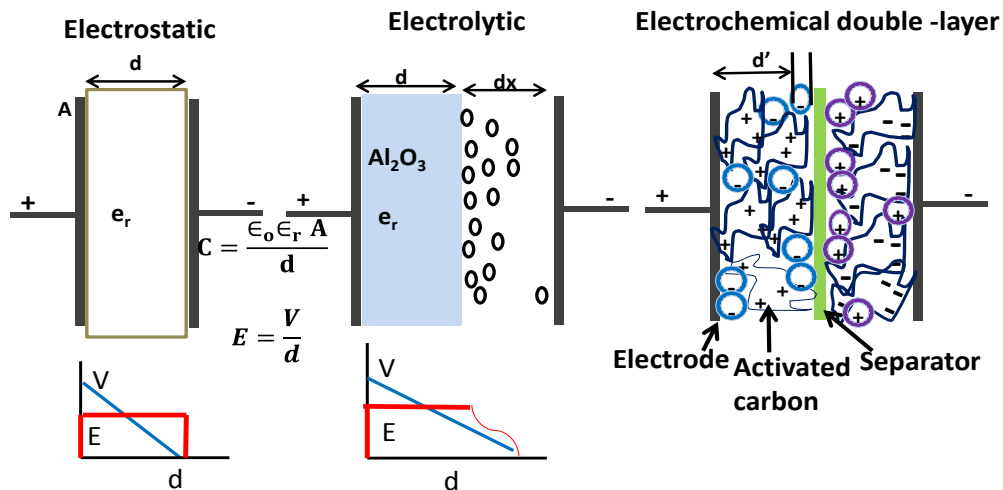


Figure 2. Differences in the configuration of the three types of capacitor. (Adapted from [6])

This chapter encompasses the history, current status, energy storage mechanism types of supercapacitor and motivation for the present research.

1.2 History and Current Status of Supercapacitor

Since the late eighteenth and early nineteenth century the charge storage mechanism at the interface of electrolyte and metal electrodes has been studied by chemist. But the practical access of the electric double layer capacitors (EDLC) has only been realized after the first patent was written by Becker at General Electric Corp in 1940 for an electrolytic capacitor using carbon electrodes [2,6,7]. SOHIO in 1969 made the first attempt to display the electric double layer capacitors (EDLC) with porous carbon materials consisting of tetralkylammonium salt based electrolyte in the market place [2, 8]. However, the EDLC suffered from low energy density, Conway and coworkers made a significant effort in the late 80's in supercapacitor research by introducing the RuO_2 with high specific capacitance and low inherent resistance electrode materials [9]. In late 90's, the supercapacitor research gained tremendous attention, after being realized the use and importance of supercapacitors in the application of hybrid electric vehicle. The physical interface between the electrode and electrolyte could store electrical charge in the order of $\sim 10^5$ farad in supercapacitor [9].

The specific capacitance in EDLC enhances 10-100 times, when the electrode materials are fabricated from transition metal oxides and conducting polymers. The energy storage principles in transition metals and conducting polymer electrodes are known as electro-sorption or redox process, which is quite different from the electric double layer mechanism [10]. This type of capacitor is referred to fourth generation capacitor, which simultaneously has the combined effect of two kinds of energy storage behavior i.e., non-faradic mechanism as in EDL capacitors and faradic process similar to batteries. According to the latest commercial report, the annual revenue generated in the

USA for electrochemical EC devices used only in electronic circuitry is around \$150-200 million [2, 5, 6]. The electrochemical capacitors in the current market are based on the high surface area porous carbon materials as well as based on high capacitance RuO₂ transition metal [11]. The unique high power characteristic of supercapacitor leads to the new concept of hybrid charge storage devices which has the combined effect of supercapacitor interfaces with the fuel cell or battery. Table 1 provides the detailed comparison on the supercapacitor and battery [12].

Table 1. Detailed parametric comparison of capacitor, supercapacitor and battery. (modified from [12])

Parameters	Capacitor	Supercapacitor	Battery	Comparison
Charge Time	10 ⁻⁶ ~10 ⁻³ sec	1~30 sec	0.3~3hrs	Moderate charging time
Discharge Time	10 ⁻⁶ ~10 ⁻³ sec	1~30 sec	1~4hrs	Moderate discharging time
Energy Density (Wh/kg)	<0.12	1~10	20~100	High Energy density
Power Density (W/kg)	>10,000	1000-2000	50~200	Moderate Power density
Cycle Life	>500,000	>100,000	500~2000	Reasonable good cyclic life
Charge/discharge Efficiency	~1.0	0.90~0.96	0.7~0.84	High efficiency

1.3 Energy Storage Principles of Supercapacitor

Energy storage mechanisms in conventional capacitor depends on the pair of parallel metallic plates having equal area A, which are separated by a distance d, in vacuum media is expressed by equation 2 [1, 13].

$$C = \frac{A\epsilon}{4\pi d} \quad (2)$$

where C is known as the device capacitance. If the plates are separated by dielectric medium then capacitance of the device incorporates the medium influence in overall capacitance of the device named as permittivity, given in equation 3 [1, 2].

$$C = \frac{A\epsilon\epsilon_r}{4\pi d} \quad (3)$$

The energy storage mechanism in electrical double layer capacitor (EDLC) is however, similar to the conventional capacitor, but the charge accumulation process does not occur on two metallic electrodes, apart from certain dielectrics. Instead the charge accumulation phenomena directly associated with the thickness of the double layer space, which is a few nanometers, established at the electrode and electrolyte interface.

Moreover, when the potential is applied on two electrodes of supercapacitor, the negative and positive ions diffuse through the electrolytes towards positive and negative electrodes. Ion migration in electrolytes creates two layers of charge storage around electrodes, which is primarily responsible for energy density, W in electrochemical double layer capacitor given by equation 4 [1, 4].

$$W = \frac{1}{2}CV^2 \quad (4)$$

where C is the specific capacitance and V is voltage develops at electrolyte and electrode interface. In general, supercapacitors have long charge-discharge cycle life due to the formation of electrostatic double layer. In addition to double layer charge separation, supercapacitor capacitance is also associated with the oxidized state change reactions occur on the electrode surface, which is called pseudo-capacitance [13-14]. The difference between double-layer capacitor and pseudo-capacitor energy storage mechanisms is discussed in the following section.

1.3.1 Electrical Double Layer Capacitor (EDLC)

The double-layer capacitance in supercapacitor was first noticed by Helmholtz in 1879, according to the Helmholtz theory the evaluation of electrical double layer is due to the strong interactions between the ions/molecules at electrode and electrolyte interface, and reversible ion adsorption onto carbon electrode is responsible for the energy storage in electrochemical capacitors [15, 16, 19]. Since no redox behavior is involved in electrochemical capacitors, the capacitance proposed by Helmholtz model does not change with the surface potential or concentration, which is different from the energy storage mechanism in batteries. The capacitance in double layer capacitor is calculated by using equation 5 [1, 17].

$$C_{di} = \frac{\epsilon_0 \epsilon_r A}{d} \quad (5)$$

where ϵ_r is the dielectric constant of the electrolyte, ϵ_0 is the permittivity of free space, A is the surface area of the electrode, and d is the thickness of electrical double-layer, depending on the size of the ions and the electrolyte concentration [17]. The electric double layer energy storage mechanism schematic is described in Figure 3 [1, 17].

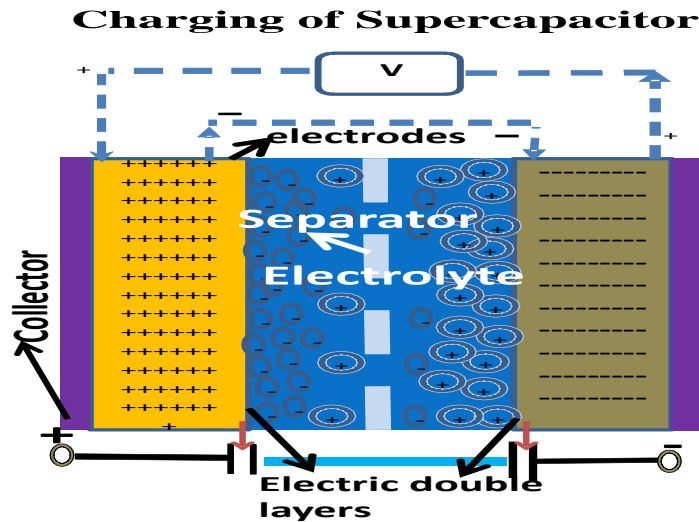


Figure 3. Electrochemical double layer energy storage mechanism. (Adapted from [1])

The separation distance, d , is usually in angstrom range for EDLC, while the separations for the conventional capacitors are in the micro-meter range. However, capacitance in electrochemical capacitor is significantly larger than calculated by conventional capacitor. A displacement current has been observed due to the arrangement of charges, which clearly explains the non faradic nature of the electrical double-layer process due to negligible charge transfer across the interface. Thus oriented polarization of charge species exists at the electrode-solution interface due to the excess or deficiency of electrons, cations or anions in solution is the reason for the forming of the double layer capacitance [18].

The complex formation mechanism of the electrical double layer is not fully understood, yet. It could be caused by several other factors e.g., shape and size of cation, and anion in electrolytes, concentration of electrolyte, packing or type of electrolyte, diffusion rate of charge, as well as the morphology of electrode materials and shape of

electrodes. However, several models have been proposed to understand the controlled potentiostatic behavior of electrode in solution. The electrical double layer can be characterized by several layers explained by the Gouy-Chapman theory, as shown in Figure 4 [19]. According to this model, the electric double layer EDL space is divided into two main layers, the inner layer which is defined as the Helmholtz layer or compact layer, which comprises of counter ions adsorbed on the charged surface, beyond this another layer is observed, which is generally called the “diffuse” layer. In the diffusive layer, the counter ions are not specifically adsorbed, instead of this, they are adsorbed due to the long range electrostatic forces interaction between the solvated ions and charged metals, and do not rely on the chemical properties of the ions [20]. The electric double layer model is based on several layers and is explained in Figure 4.

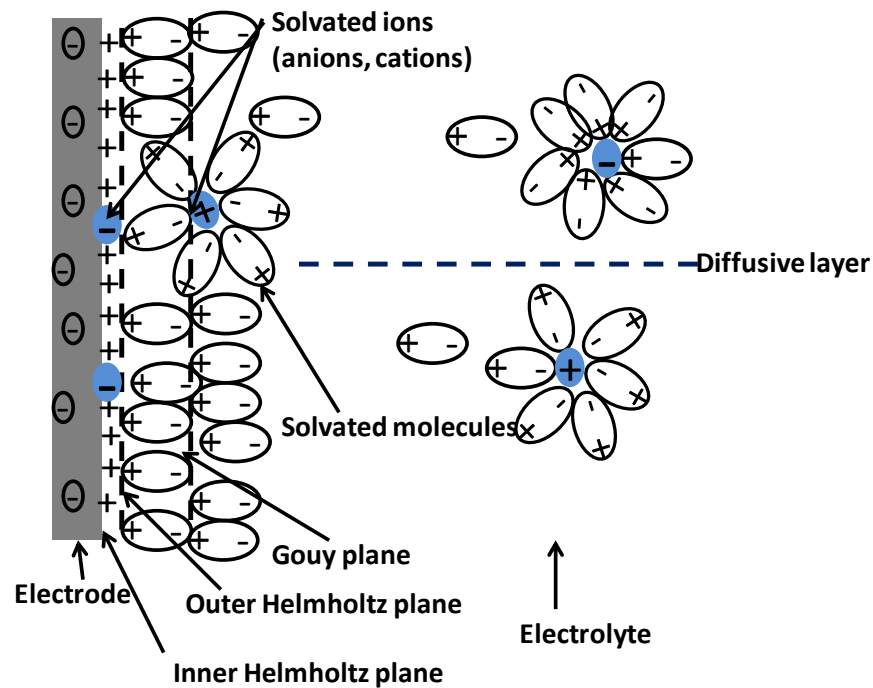


Figure 4. Electrochemical model describing the extension of double layers from the electrode surface into bulk of liquid electrolyte. (Adapted from [19, 33])

Therefore, the overall calculated EDL capacitance is the series capacitance of the compact layer and the diffusive layer is given in equation 6 [20].

$$\frac{1}{C_{total}} = \frac{1}{C_H} + \frac{1}{C_{diff}} \quad (6)$$

Both layers have a potential difference, the outer layer is surrounded by the three dimensional diffusive layer due to thermal agitation of the electrolyte. The total charge density of the electrical double layer is assumed due to the charge density of the inner layer as well as the charge density of excessive ions in diffusive layer [21]. The electric double layer capacitance also strongly depends on the shape of the electric double layer space, which can be in different forms e.g., bell-shape, convex, concave, or camel-like shape [22]. An extensive amount of work has been carried out on the carbon electrodes to understand the electric double layer mechanism in detail.

1.3.2 PseudoCapacitor

The energy storage mechanism, which involves the effect of the ions flow due to the change in electrochemical state of the material, is called faradic process e.g., in batteries the chemical energy is being carried out by flow of ions when the potential is applied across the two electrodes of battery. The difference in EDL and pseudocapacitance is given in Figure 5 [9, 19].

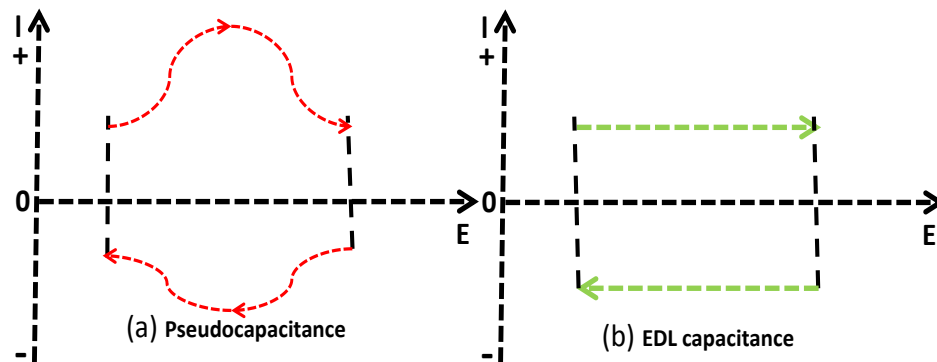


Figure 5. Difference in electric double layer and pseudocapacitance. (Adapted from [9, 19])

The capacitance in pseudocapacitor depends on the fast and reversible faradic reactions occurring on the electroactive materials of electrode surface at the appropriate potentials which assists in fast charge/discharge rate and high reversibility.

In pseudocapacitors, the charge transfer occurs across the double layer of the electrode and electrolyte interphase, the energy storage mechanism in pseudocapacitors is indirect and to some extent analogous to battery charging and discharging principle. The pseudocapacitance is then calculated by following equation 7 [1, 9, 20].

$$C_p = \frac{\Delta q}{\Delta V} \quad (7)$$

where (Δq) is an amount of charge stored which is proportional to (ΔV) the potential difference. Advantages and drawbacks of the double layer and pseudo capacitance are discussed in Table 2 [9].

Table 2. Advantages and disadvantages of electrical double layer capacitor and pseudocapacitor. (modified from [9])

Electric Double Layer Capacitor	Pseudocapacitor	Difference
Phase angle 90°	Phase angle 45°	More transmission like behavior
Low specific energy density	High specific energy density	Good capacity of charge storage
High reversibility	Moderate reversibility	Reasonably good cyclic life
Capacitance remains constant with voltage	Capacitance changes with voltage	Small leakage effect
Narrow potential window (1-3V)	Large potential window (1-5V)	Broad range of applications
High Power due to good diffusion	Low Power due to Kinetic limitations	High diffusion resistance

The cause of developing pseudocapacitance depends on the three types of electrochemical reactions e.g., a) It may be developed due to the redox reactions of ions adsorption on the electrode surface from the electrolyte b) redox reactions develop due to changes in the oxidation state of transition metals e.g., RuO_2 , MnO_2 and IrO_2 used as the active electrode material c) doping and dedoping of the conducting polymer material also gives rise to reversible redox reaction and thus build pseudocapacitance d) the self-discharge degradation of the supercapacitor due to irreversible reactions. The charge movements in the above electrochemical faradic reactions are voltage dependent, which is the same to charging/discharging in batteries [19].

Many factors can influence the pseudocapacitance e.g., the porosity of materials, particle sizes, conductivity of electrode materials, as well as the surface area of the electrode, packing of electrolyte, design of cell, and etc. Generally the pseudocapacitance shows 10 times more capacitance than the electric double layer capacitance, on the other it has some draw backs e.g., lifecycle and reliability of a device [23, 24].

During the oxidation and reduction of these materials, the insertion and removal of counter ions from an electrolyte solution to the electrode surface helps in maintaining the charge neutrality. Another important difference between pseudocapacitors and electrochemical double layer capacitors is that the entire mass of the material is used to store charge. In the following sections are the types of capacitor based on pseudocapacitance mechanism are discussed.

1.3.2.1 Types of Pseudocapacitors

So far three types of Pseudocapacitors are widely known. In the following section these three types are discussed.

(a) Type I

In type I both supercapacitor electrodes are fabricated from identical material. Usually the capacitor either is comprised of the same p type conducting polymer, or both electrodes can be made of the same n type conducting polymers and transition metals. This type of pseudocapacitor is called symmetric capacitor. The capacitance in this type of supercapacitor depends on the individual capacitance of each electrode, which is given in equation 8[1, 25].

$$\frac{1}{C_t} = \frac{1}{C_1} + \frac{1}{C_2} \quad (8)$$

where C_t is the overall capacitance of the cell, which is calculated by adding the individual capacitance of two electrodes in series. Since both electrodes are alike, so $C_1=C_2$, this means that the same amount of charge is utilized by each electrode for doping or undoping of the electrode materials. However this type of capacitor is limited in capacitance and has a narrow potential window [26]. Besides the

capacitance in this type of capacitor it depends on the nature and concentration of the electrolyte as well as the mass of electrodes.

(b) Type II

In type II, since it is consisted of two different p-type conducting polymer electrodes, it exhibits a larger potential window than type I. Configuration of type II supercapacitor is known as an asymmetric device. This device could have the hybrid system based on the composite material consisted of transition metals e.g., RuO₂, IrO₂, MnO₂, Ce₂O₃, and even non-redox carbon materials (activated carbon, graphite, carbon nanotubes, porous carbon etc.) combined with p or n-type conducting polymers [25]. Type II supercapacitors have greater capacity than type I, using different p, n-type polymer electrodes. In this type the capacitance participation and the amount of charge utilized in overall capacitance of each electrode is not the same. Type II is due to higher working cell voltage and shows the increase in energy density and is the most common type in practical use today [26].

(c) Type III

Configuration of the type III is different from type I and type II capacitors, as it is based on two of the same or different conducting polymers with one of the electrodes comprised either of an n type or p type doped polymer. Due to having both electrodes in its doping states, it provides the less resistance, large voltage window and high specific capacitance. The only drawback of type III is it mostly

consists of conducting polymers are available p-type in nature and few of them are of n type doped [25]. Therefore, among the three types of pseudocapacitors commercially favorable types are of type 1 or type II.

1.3.3 Hybrid Capacitor

In order to exploit the full advantages of EDLCs and pseudocapacitors improvements in the overall performance of a device, the third type of capacitor was attempted, which is called hybrid capacitor. The hybrid system renders higher power and energy density without sacrificing the cycle stability and life of the device since the energy storage mechanism in hybrid systems depend on both faradic and nonfaradic processes. In a hybrid system, electrode configurations are based on either composite electrodes (which is integrated with carbon-based materials, conducting polymer) or metal oxide materials lead the benefit of physical and chemical charge storage mechanisms together in a single electrode [27]. The coupling of carbon based material electrodes with pseudocapacitor electrodes has gained an immense importance due to substantial enhancement in total capacitance of the device.

1.4 Electrode Materials for Supercapacitor

Supercapacitor electrodes can be fabricated by utilizing its inherent capacitance properties of a variety of materials in different types of supercapacitors as illustrated in Figure 6 [28].

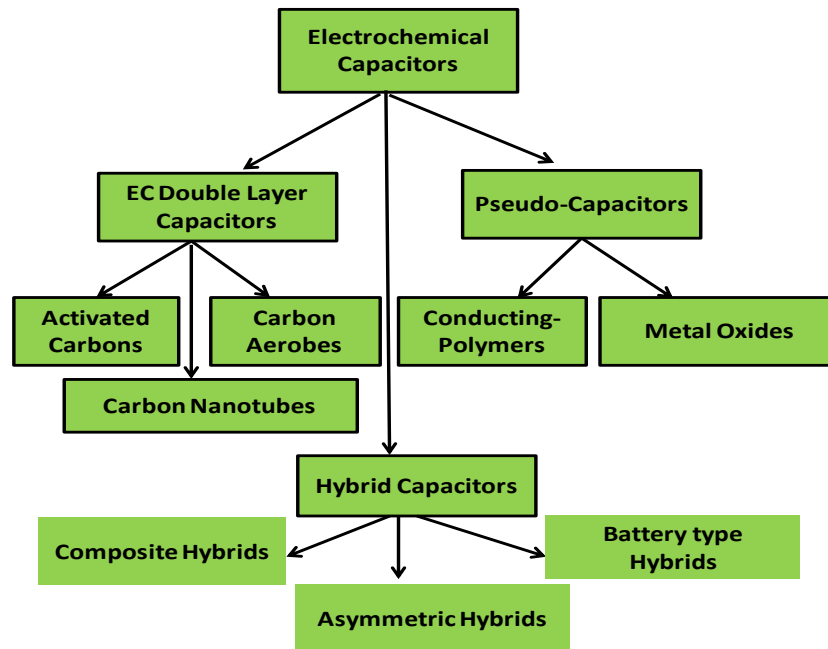


Figure 6. Types of supercapacitor. (Adapted from [28])

The first group of materials, which is most frequently used in commercial supercapacitor electrodes is carbon. Carbon has gained considerable interest due to its various properties including the existence of different allotropies, accessibility, low cost, high surface area, high conductivity, superior corrosion inhibition property, high temperature stability, environmental friendliness and easy processibility. It exists in various micro-textures (powder, fibers, foams, fabrics, nanocomposites), and in different dimensionality from 0 to 3D [29, 30]. The unique adaptable porosity of carbon with various surface functionality is, preferred it to use as conductive additives in active materials of supercapacitor substrates for current leads. So far the forms of carbon, which are well recognized in the use of the supercapacitor electrodes, are activated carbon,

carbon aerogels, carbon nanotubes (CNTs), carbon fibers and graphene [30]. The different forms of carbon are depicted in Figure 7.

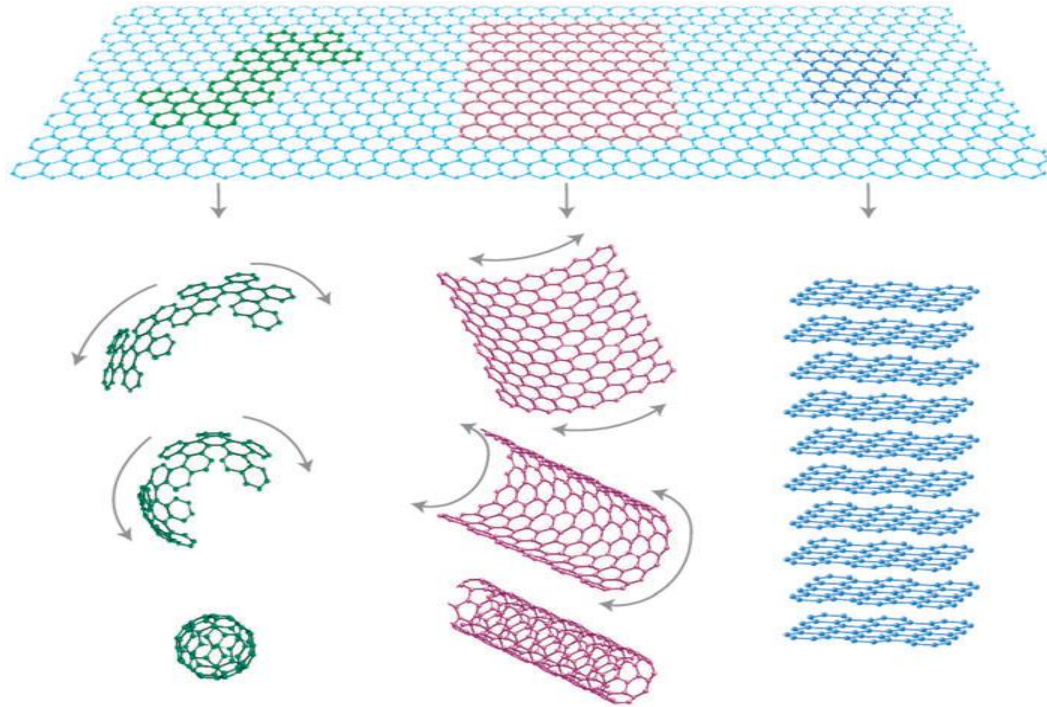


Figure 7. Schematic of carbon family in 0-dimensional fullerene, 1-dimensional carbon nanotube, 2-dimensional graphene, 3-dimensional graphite. (Figure used by permission of the Nature Publishing Group) [30]

1.4.1 Activated Carbon

Activated carbon is a widely known material used for supercapacitor electrodes due to its highly economical processing method and large surface area (BET) which has reported in the range of 500 to 3000m²g⁻¹ [31]. It has shown a good capacitive trend for electrochemical applications. In the electrochemical capacitor (EC), the specific capacitance (SC) obtained by activated carbon is in the range of 25 to 150 F/gm in both aqueous and organic electrolyte [32]. It has shown the higher capacity tendency due to existence of three different pore types in activated carbon e.g., micropores (diameter < 2 nm), mesopores (diameter from 2-50 nm), or macropores (diameter >50 nm) [33].

However, in order to have all pores accessible electrochemically, the size of the pores should be essentially bigger than the size of electrolyte ions. Besides the porosity of material, charge rate is another key factor in the overall enhancement of the specific capacitance of activated carbon based electrode.

Other than activated carbon, another attractive material for supercapacitor electrodes is carbon black, which is more conducting than activated carbon and have high surface area to volume ratio. The conductivity range in carbon black is from 0.1 to 100, which is mainly due to the graphitic conduction mechanism in carbon black [33, 34]. Not only being suitable for supercapacitor electrode material but it can also be used as conducting additive to improve the overall conductivity and performance of the material.

1.4.2 Carbon Aerogels

Carbon aerogels considered one of the promising materials for supercapacitor electrodes and so far the maximum reported specific capacitance (SC) value for carbon aerogel is 180 F/g [35, 36]. Carbon aerogels are highly porous solid materials which are composed of interlinked colloidal like carbon particles or polymeric chains. So far the large surface area for carbon aerogels has been reported approximately ($400-1000 \text{ m}^2\text{g}^{-1}$) with uniform pore size (3-60 μm), high packing density, and possess good electrically conductivity [35]. Carbon aerogels are available in different forms e.g., monoliths, composites, thin films, powders or microspheres. Furthermore, the surface area of aerogels can be substantially increased by surface activation.

1.4.3 Carbon Nanotubes (CNTs)

Carbon nanotubes (CNTs) are one of the important forms of carbon, which were first observed by Iijima in carbon soot in 1991 [36]. CNTs are classified in two types, known as single wall carbon nanotubes (SWCNTs) and multiwall carbon nanotubes (MWCNTs). Due to its amazing electronic and mechanical properties CNTs have captured the attention of researchers worldwide. It has an elastic modulus that is greater than diamond, which is one of the hardest materials. It has also shown a capacity to carry and generates an electric current 1000 times' greater than copper wire [36, 37]. The most notable characteristic of CNTs is the diameter of a tube, which is usually in the range of 1-3nm in length in the order of tens of microns. CNTs naturally show capacitive behavior in their pure form. CNTs have supercapacitor electrodes due to mesopore structures and allow easy diffusion of ions within, and provides lower ESR (equivalent series resistance) than activated carbon and shows the enhancement in power density and energy density of the supercapacitor. However, the high cost in the production of CNTs limits use in different applications. So far, the maximum specific capacitance has been reported for SWCNTs electrodes is 160 F/g and achieved power density was 20KW/kg for the supercapacitor device [37]. Moreover, CNTs show high resiliency due to the nanotubular structure, which could be useful in the formation of composite materials with either conducting polymers or transition metals e.g., MnO_2 , Ni(OH)_2 to improve overall capacitance and stability of supercapacitor electrodes [37, 38].

In addition to CNTs, another attractive material for supercapacitor electrodes is carbon fiber. Carbon fiber has superior charge transportation property due to one-dimensionality. It provides high adsorption capacities to ions due to the existence of large

number of pores at the surface of the fiber and proves to be the best candidate for EDLC electrodes [39]. Recently, graphene is expected one of the most promising new material used in an electrochemical double layer capacitor. The intrinsic properties, such as high flexibility, high conductivity, large surface area, large porosity, and excellent thermal and mechanical properties make graphene the best candidate. Graphene is recognized mostly as a single sheet of graphitic carbon, however, it shows lower columbic efficiency in the beginning due to large surface area to volume ratio, but beyond number of the cycles it renders constant capacity [40].

1.4.4 Transition Metal Oxides

A transition metal oxide due to its superior pseudocapacitive behavior, besides carbon, is a potential candidate material for a supercapacitor. Extensively researched metal oxides for supercapacitor applications so far are ruthenium oxide, nickel oxide, manganese oxide, and cobalt oxide, etc. [41]. Since 1970, RuO_2 was deeply investigated due to its excellent pseudocapacitive and stability characteristics. So far, the SC of RuO_2 in an aqueous system has been observed as high as 1000 F/g in H_2SO_4 electrolyte at room temperature [42]. The limited commercial availability of RuO_2 due to the high cost made it a concern to exploit the potential of several other metal oxides as the supercapacitor electrodes.

Other potential candidates MnO_2 , IrO_2 and NiO are considered potential candidates as the supercapacitor electrodes due to low cost, environmental compatibility, high theoretical specific capacitance 1370 to 1390 F/g, and excellent capacitive behavior. The specific capacitance for MnO_2 and NiO metal oxides are reported as 250 F/g to

280F/g [43]. Different intrinsic properties of various metal oxides are categorized in several advantages and limitations. However, in order to exploit the full advantage of metal oxides, the composite materials, made of one or more materials including: metal oxides, CNTs, activated carbon and conducting polymers as supercapacitor electrodes have also been studied to enhance the performance of a device.

1.4.5 Conducting Polymers

The third group of material, which has already been investigated in detail as a new choice for supercapacitor electrodes, is conducting polymers. The most common types of conducting polymers tested in supercapacitor are [polyaniline (PANI), polypyrrole (PPY), poly (3, 4-ethylenedioxythiophene) (PEDOT) and polythiophene (PTh) poly(3-arylthiophene), p-dopedpoly(pyrole), poly(1,5-diaminoanthraquinone), poly-3-(3,4-difluorophenyl) thiophene, poly-3-(4-cyanophenyl) thiophene, poly-(3-parafluorophenyl)thiophene and poly[bis(phenylamino)disulfide]. Conducting polymers are different than carbon and metal oxides, they have their own unique properties, mainly it is low cost, large scale, easy to process, have fast redox reactions, are substrate independent and have high conductivity. The charging-discharging mechanism in conducting polymers either n type or p type, is different from carbon material: it is solely associated with the faradic reaction process of ions, cations, electrons at the electrodes/electrolyte interface [44].

Unlike the cyclic voltammogram (CV) of carbon, of conducting polymers is not in rectangular shape, instead current peaks at the particular redox potential of polymers are observed [45]. The only main drawback of the conducting polymers is the poor

mechanical stability. Since cycling polymers undergo a series of physical changes e.g., swelling, shrinkage, doping and undoping, which degrades the performance of material over the time. Therefore in order to enhance the mechanical property of the conducting polymer synthesis of the composite materials can be a good choice.

1.5 Target of Research

The driving motivation behind this research effort is to understand the role of nanocomposite electrodes in supercapacitors. The supercapacitor device is recognized as a well characterized device, but when it comes to high power density and high energy density applications, it is still facing issues that need to be resolved. There is a need to improve electrode engineering aspects including the chemical and physical properties (such as different electrolytes, solvent, and binders) of the supercapacitor.

The main purpose of this doctoral work is to study the scope of nanocomposite materials for electrodes in supercapacitor. In this research, several nanocomposite materials are explored and exploited to meet the increasing demand for efficient electrochemical energy storage devices. Some of the research investigations which have been discussed in this doctoral document are briefly outlined below.

Chapter 1 contains a thorough literature review and the current status of supercapacitor research. Further, the importance and application of current research related to electrochemical devices has been explored. The detailed discussion of the energy storage mechanism in electrochemical capacitors has been described. Moreover, in order to meet the current challenges in the performance and commercialization of the

electrochemical capacitor, the need and importance of different electrode materials has also been investigated.

Chapter 2 contains the synthesis, characterization techniques and application of aromatic based conducting polymer nanocomposites. The structural and capacitive behavior of aromatic based conducting polymer nanocomposites for electrochemical energy storage devices was analyzed using X-ray diffraction (XRD), Scanning electron microscopy (SEM), Transmission electron microscopy (TEM), Raman spectroscopy, and Fourier Transform Infrared (FTIR) spectroscopy, Cyclic voltammetry (CV), electrochemical impedance spectroscopy (EIS), and Galvanostatic charge-discharge cycling techniques.

Chapter 3 contains the detailed investigation of the influence of graphene composition on graphene-polyaniline nanocomposites, the effects of conductivity and thickness variation are correlated with the capacitive performance for supercapacitor application via cyclic voltammetry (CV), Galvanostatic charge-discharge cycling, and electrochemical impedance spectroscopy (EIS).

Chapter 4 contains the detailed investigation of the influence, solvents, concentration and type of electrolytes on graphene-polyaniline nanocomposites electrodes for electrochemical capacitor application. The role of different solvents, including: Nafion, NMP (*N*-Methyl-2-pyrrolidone), and DMF (dimethylformamide), were examined in synthesizing the graphene-polyaniline electrodes for electrochemical capacitor applications. Several electrolytes were used to investigate their significance in the performance of supercapacitors, which includes aqueous electrolytes, HCl and

H₂SO₄, organic electrolytes i.e., LiClO₄, and ionic liquid. All of these electrochemical measurements on supercapacitors were carried out at room temperature.

Chapters 5 and 6 contain the discussion of synthesis and characterization techniques for heterocyclic conducting polymer nanocomposites, and its substitutes effect e.g., (graphene-polythiophene and graphene-poly (3, 4- ethylenedioxythiophene) nanocomposites for their use in the overall improvement of electrochemical capacitor.

Chapter 7 is the summary of the doctoral work presented by providing some incentives and suggestions for future work related to nanocomposite materials. One of the most important reasons to enhance the life of the supercapacitor is the use of solid electrolytes and high k dielectric in order to prevent a leakage current and increase the durability of the device. The second factor to improve the overall performance of the device is to reduce the equivalent series resistance by fabricating the micro contacts.

CHAPTER 2: AROMATIC BASED CONDUCTING POLYMER NANOCOMPOSITE FOR ELECTROCHEMICAL CAPACITOR

2.1 Introduction

Since 1977, conjugated conducting polymers have been under a tremendous amount of research due to unique properties of lighter weight, corrosion inhibition, low cost and greater workability [46]. The fast electron transfer during the faradic charge process in the conducting polymers has gained wide interest in the various electronic applications especially, in the field effect transistor, photovoltaic, portable electronic circuits, lithium ion batteries and supercapacitors thus, it is known as the materials of the twenty first century [47]. The most studied conducting polymer among the family of conducting polymers is polyaniline due to its unusual characteristic ease of synthesis, doping, dedoping, low cost, mechanical flexibility, chemical properties and environmental compatibility.

The occurrence of three different distinct oxidation states in polyaniline makes it one of the promising candidates in several important applications [48]. Polyaniline reflects faded yellow or colorless when it is in fully reduced form called the leucoemeraldine state, it gives the blue/violet color when polyaniline is in fully oxidized state named pernigraniline, the third and most useful state of polyaniline is known as emeraldine base and the color taken by polyaniline in this state is green or slightly blue. Among all the above, the third state is the most useful state of polyaniline due to its higher conductivity when doped with an acid and higher stability at room temperature

than leucoemeraldine and pernigraniline, which are known as poor conductors, even after doping with acid. Polyaniline exhibits insulator-to-metal transitions and color changes depending upon both its oxidation state and protonation level. Therefore, the color change property of polyaniline associates with the change in different conductivity levels makes it highly promising choice to be used in fast supercapacitor electrodes [49]. Figure 8 shows the chemical structure of polyaniline.

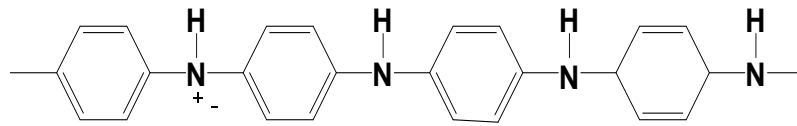


Figure 8. Chemical structure of polyaniline consists of quinoid and benzenoid rings. [49]

Besides the low cost and higher conductivity of polyaniline, it has some drawbacks mainly related to its mechanical stability, which limits its use as a supercapacitor. However, in order to mitigate the polyaniline disadvantages and to utilize its full potential, researchers have been trying to use the polyaniline nanocomposite with different materials e.g., activated carbon, carbon nanotube, transition metal oxides (RuO_2 , MnO_2 , NiO , and Fe_2O_3) to enhance overall stability and performance of supercapacitor devices [50]. The nanocomposite of conducting polymers has become of scientific and industrial interest due to its enhanced properties arising from the reinforcement of two nanomaterials. In this chapter, we discuss the synthesis, characterization and applications of several polyaniline nanocomposites e.g., polyaniline-ZnO, polyaniline- RuO_2 , polyaniline-Graphene, ZnO/Graphene-polyaniline for the use of a supercapacitor using very simple synthesis approach described below.

2.2 Experimental Procedure

The schematic of the overall experimental procedure of polyaniline nanocomposite is shown in Figure 9.

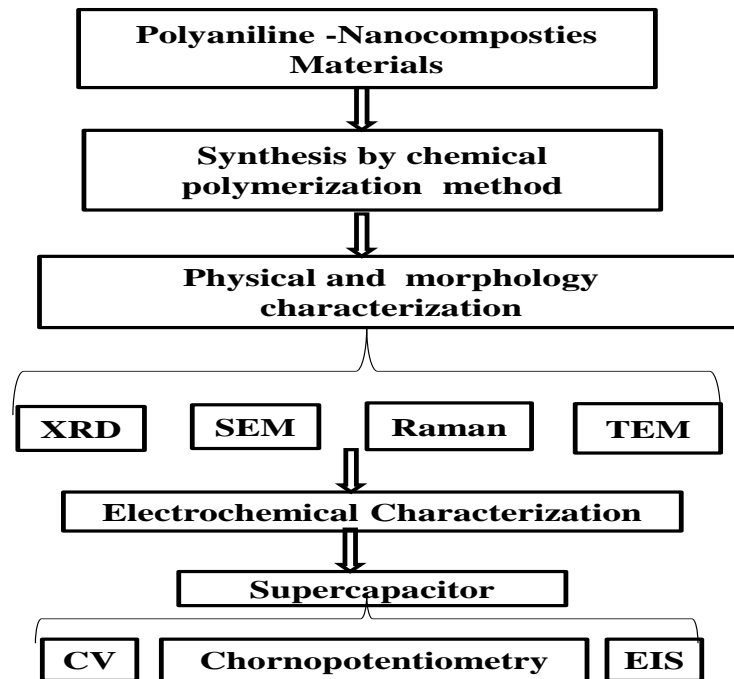


Figure 9. Flow diagram of the experimental procedure.

This schematic is describing the two main parts of polyaniline nanocomposites research work discussed in this chapter. The first part involves the fabrication and structural characterization of the as-prepared nanocomposite materials. the second part is discussing the application of these prepared nanocomposite materials for supercapacitor electrodes.

2.3 Materials

The list of materials used in this dissertation for the synthesis of conducting polymer nanocomposites is shown in Table 3. All these chemicals and materials were employed as purchased without any further purification unless specified.

Table 3. List of chemicals used in this dissertation.

Materials	Company	Purity
1-methyl-2-pyrrolidionone (NMP)	Sigma Aldrich	99.5%
Aniline	Sigma Aldrich	99.5%
sodium hydroxide	Sigma Aldrich	powder, 97
Ammonium persulfate	Sigma Aldrich	98%
N-N-dimethylformamide	Alfa Aesar	99.8%
Graphene platelets	Angstrom Materials	99%
Hydrochloric acid	Sigma Aldrich	37%
Propylene carbonate	Sigma Aldrich	99.7%
Diethyl carbonate (DEC)	Sigma Aldrich	99%
ZnO nanoparticles	Nano spring sky	99%
RuO ₂	Sigma Aldrich	99%
Platinum foil	Sigma Aldrich	99%
Lithium perchlorate	Sigma Aldrich	99%
Sulfuric acid	Sigma Aldrich	99%
Ionic liquid	Sigma Aldrich	99%
Thiophene	Sigma Aldrich	99%
ethylene dioxythiophene	Sigma Aldrich	99%
polystyrene sulfonate Na salt	Sigma Aldrich	99%

2.4 Synthesis Method

The polyaniline nanocomposite has been investigated in this study and was synthesized via chemical polymerization approach, which is explained in detail in the following section.

2.4.1 Chemical Polymerization Method

In polymer science, polymerization is defined as a formation process of three dimensional polymer networks due to the chemical reaction and bonding of monomer molecules. Though there are several ways to synthesis polyaniline e.g., electro deposition, chemical vapor deposition, electro spinning, spray pyrolysis, the most common method used for polyaniline synthesis is the chemical oxidation method due to the low cost, ease of synthesis and potential for large scale [51]. Here we report a facile chemical approach to high surface area polyaniline-nanocomposites, under ambient conditions using aqueous polymerization. The G/ZnO/RuO₂-PANI nanocomposites were chemically synthesized by oxidative polymerization of aniline using ammonium peroxydisulfate [(NH₄)₂S₂O₈] as an oxidant under controlled conditions. While keeping the 1:1 wt% ratio of aniline to G/ZnO/RuO₂, it was added in 200ml of 1M HCl solution, The solution was further cooled down to 4°C in an ice bath. Ammonium peroxydisulfate (0.025M) dissolved separately in 100ml of 1M HCl solution, and later [(NH₄)₂S₂O₈] in 1M HCl solution was added slowly into the aniline solution, and the reaction was continued for 24h [52]. After the stirring for 24h the dark green precipitate of the G/ZnO/RuO₂-PANI nanocomposites were recovered from the reaction vessel and was filtered and washed using deionized water, methanol, acetone, and diethyl ether for the

elimination of the low molecular weight polymer and oligomers. Further, this precipitate was heated at 100°C in a controlled temperature furnace [52].

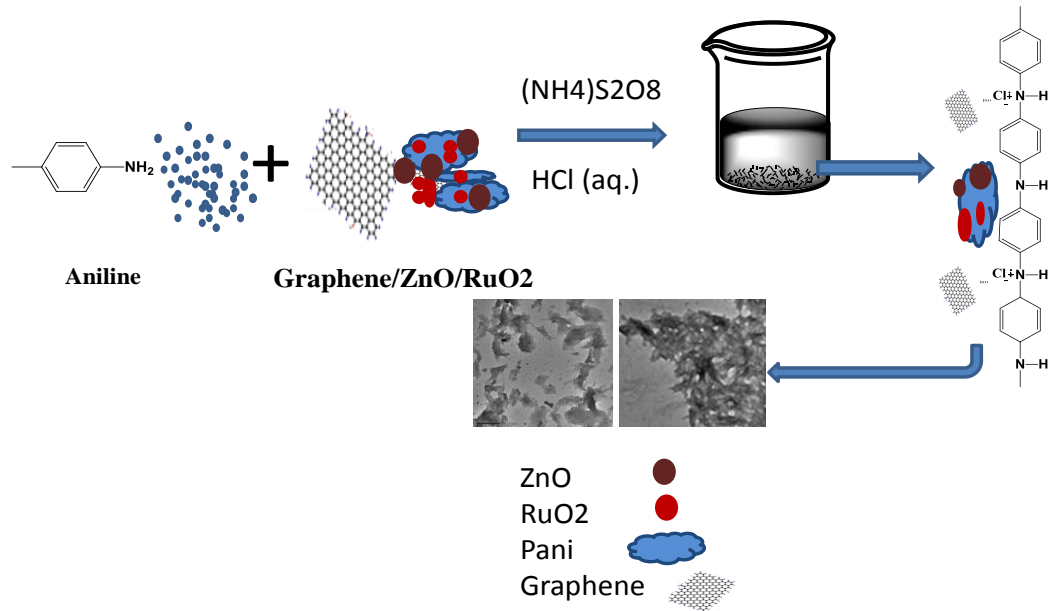


Figure 10. Schematic of polyaniline nanocomposites materials.

The schematic of the successful synthesis of G/ZnO/RuO₂-PANI nanocomposites in conjunction with an aniline monomer to produce mechanical stable, large surface area and conductive nanocomposites material is demonstrated in the Figure 10.

2.4.2 Physical and Structural Characterization

The surface morphology and the feature size of G/ZnO/RuO₂-PANI films were then investigated using an Hitachi S800 Field Emission Scanning Electron Microscope (FESEM). The crystalline structures of the G/ZnO/RuO₂-PANI nanocomposites were investigated using High-Resolution Transmission Electron Microscopy (HRTEM). The crystallographic information of G/ZnO/RuO₂-PANI films were also observed using X-Ray Diffraction technique (XRD). Raman spectra of the as prepared G/ZnO/RuO₂-PANI

films were recorded using a Renishaw Ramascope system at the excitation wavelength of 514 nm. The FTIR spectrum of the conducting polymer nanocomposites was measured using a Perkin Elmer spectrometer with pure KBr as the background. The samples for all four G/ZnO/RuO₂-PANI nanocomposites were prepared by mixing the material in NMP and later it was deposited on the (100) p-type-silicon substrate for all the characterization techniques described above.

2.4.2.1 Transmission Electron Microscopy (TEM)

Transmission Electron Microscopy (TEM) is a well-known microscopy technique, which is mainly used to study the morphology, crystal structure, and the electronic structure of synthesized materials. TEM provides high resolution imaging information of materials due to the small de Broglie wavelength of electrons [53]. All TEM samples, which are given in Figure 11 were prepared by drop casting the synthesized material in ethanol on the thin copper grid, and the solvent was allowed to evaporate at room temperature.

Figures 11(a, b, c, d) reveal interesting information of TEM images of graphene-Polyaniline (G-PANI), ZnO-PANI, graphene/ZnO-PANI and RuO₂-PANI nanocomposites, respectively. Figure 11(a) clearly shows that the graphene sheets are surrounded by homogenous polyaniline networks which is evident of the successful synthesis of G-PANI nanocomposites. The High Resolution TEM image in the inset of Figure 11(a) depicts that the synthesized G-PANI composite not only contains porosity and uniformity, but it also has some order of crystallinity due to the presence of graphene platelets. Furthermore, no agglomeration of either graphene or PANI could be seen in TEM results, but the graphene sheets are successfully covered by the polyaniline layers,

this is quite promising for obtaining the high surface area of the synthesized material for electrochemical performance.

The TEM studies have confirmed that few layers of graphene sheets are also stacked with conducting polymer chain in all graphene-conducting polymer (G-CPs) nanocomposites. Figure 11(b & c) illustrates the TEM micrographs of the ZnO-PANI (doped) and ZnO/G-PANI nanocomposites reveal that average diameter of ZnO-PANI particle size is in the range of 30 to 80 nm, which is slightly larger than the ZnO nanoparticle precursors it was equal to 20 nm, indicating that polymerization occurs by aggregation of few nanoparticles. ZnO spherical nanoparticles are completely embedded in the polyaniline network chain, and can be seen in Figure 11(b). The TEM image in Figure 11(c) also depicts the successful encapsulation of tertiary nanocomposite and includes graphene and ZnO nanoparticles within polyaniline network.

It can also be observed that the influence of ZnO and graphene platelets in the polyaniline network provides a larger surface area than ZnO-PANI nanocomposites but it also has a larger particle size which is around 50 to 90nm. However, TEM images of the RuO₂-PANI nanocomposite in Figure 11(d) shows the complete coverage of PANI within RuO₂ nanoparticles. The initial diameter of RuO₂ was 40nm, which was increased to 60nm due to the successful incorporation of RuO₂ and PANI during chemical polymerization synthesis. However, in spite of the larger particle size it also provides the larger surface area due to its flake like morphology, which is quite significant in the enhancement of capacitive behavior of synthesized nanocomposites. At low magnification, the tetrahedral shape of RuO₂ particles was also observed in the TEM image 11(d).

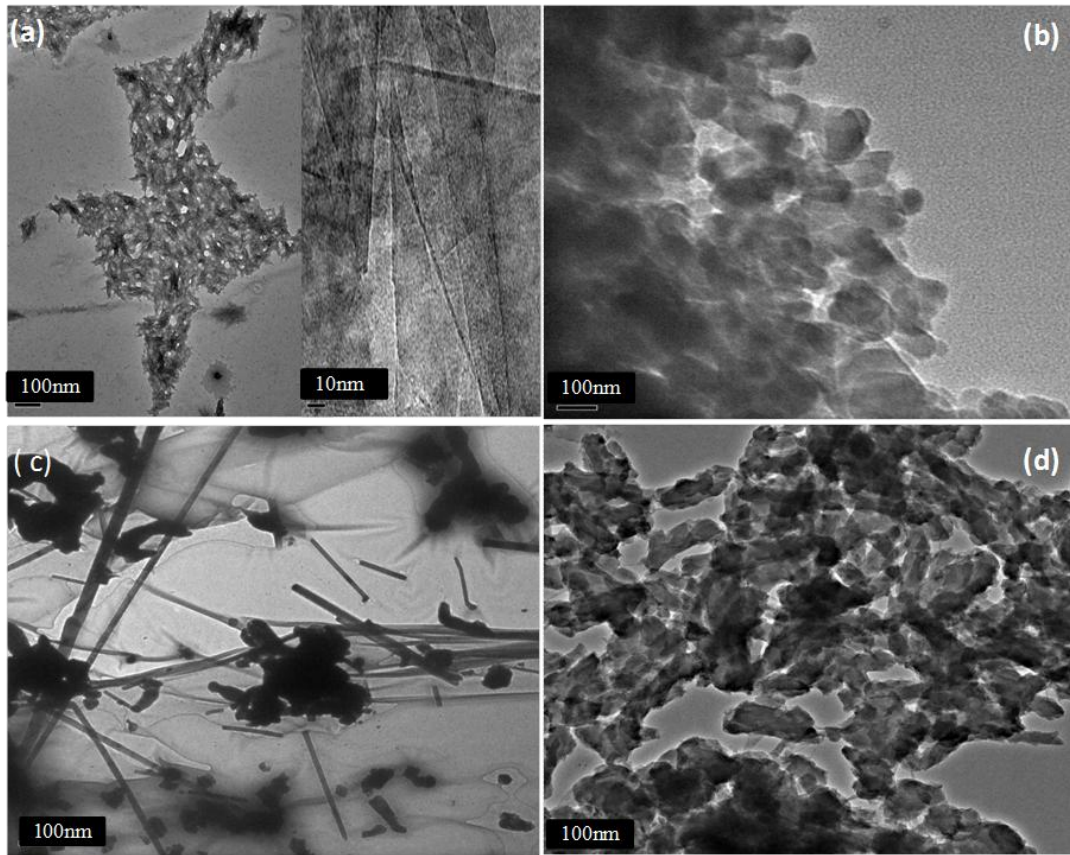


Figure 11. TEM images of (a) G-PANI (b) ZnO-PANI (c) G/ZnO- PANI (d) RuO₂-PANI nanocomposites.

2.4.2.2 Scanning Electron Microscopy (SEM)

Scanning Electron Microscopy is known as one of the most widely used and established microscopy techniques. In this microscopy approach, a high intensity electron beam scans through the sample surface and information related to topology, composition, electrical conductivity and feature size of the sample surface is collected in the form of electrical signals, which later transform into the image. Figure 12(a, b, c, d) shows the SEM-images of G-PANI, ZnO-PANI, G/ZnO-PANI and RuO₂-PANI nanocomposites. All samples of PANI nanocomposites for SEM images were prepared in N-methyl-

2pyrrolidone (NMP) and the resultant film was drop casted on the p type silicon (100) substrate. Later the film was doped in 0.1M HCl for a couple of minutes, special attention must be taken as to not leave the film in the HCl for a longer time to avoid the removal of the film from the Si substrate [52, 54]. Figure 12(a) illustrates the interesting structure of an interpenetrating network throughout the G- PANI surface.

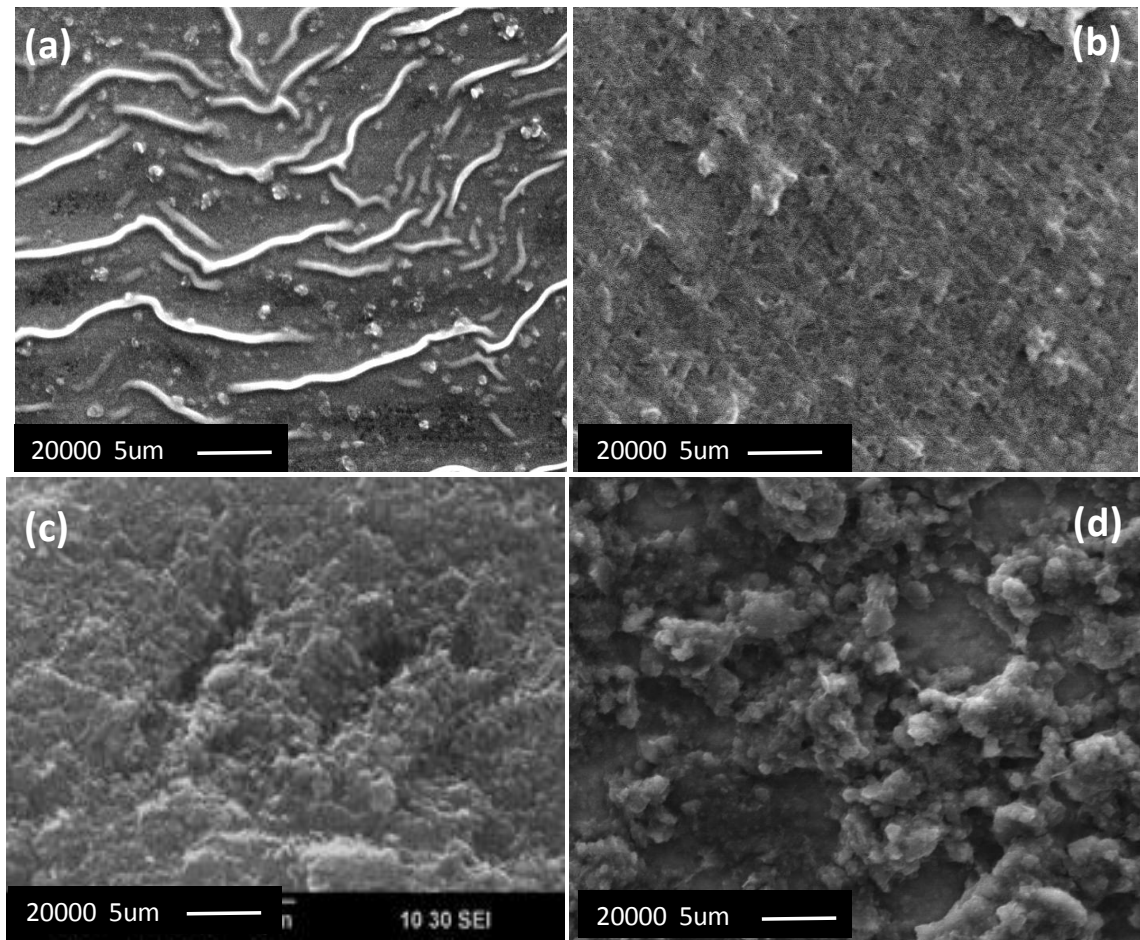


Figure 12. SEM images of the (a) G-PANI (b) ZnO-PANI (c) G/ZnO-PANI (d) RuO₂-PANI nanocomposites.

The typical flake structure of the G-PANI film cannot be observed in the SEM image because NMP was used as a solvent in the film formation, which possesses the very characteristic of the plasticizer to produce a smooth film. Doping in the G-PANI

film creates polaron and bipolaron states, which change, the morphology of polyaniline and the less lined penetrating structure was observed in Figure 12(a). Figure 12 (b&c) represents the SEM image of ZnO-PANI and G/ZnO-PANI (doped) nanocomposite film. The ZnO-PANI film indicates a rock structure embedded within the polymeric structure and is entirely different from the PANI film as observed by Ram et al [55, 59]. The average diameter and the height of ZnO-PANI particles have been found to be 50 nm and 100 nm, respectively.

On the other hand, the SEM image of an aligned G/ZnO-PANI nanocomposite exhibits more porous and uniform morphology than ZnO-PANI, but there is no significant difference in the structure and orientation of both materials. Figure 12(d) exclusively shows the flake like morphology of the RuO₂-PANI synthesized material. It could be due to the overall mixing effect of PANI and RuO₂ in a polymeric matrix structure, which lends more flexibility to the system. The average particle size of synthesized RuO₂-PANI has been found to be around 50nm to 80nm, respectively. In fact the, conducting polymer nanocomposites provide porous structures. Having higher surface area these deliver good access to electrolytes, and hence offer the possibility for high specific capacitance and fast redox processes.

2.4.2.3 X-Ray Diffraction (XRD)

X-Ray Diffraction (XRD) is an useful nondestructive technique to investigate the crystal structure of materials. The scattering of X-rays from the lattice planes of material at a typical characteristic angle results in a specific crystal structure pattern of a given compound. The crystal size of materials is calculated using the Scherrer Formula given in equation 9.

$$B(2\theta) = \frac{K\lambda}{L\cos\theta} \quad (9)$$

where L is the crystal size in nm, λ is the x-ray wavelength (Å), K is the constant value normally around 0.9 related with the shape factor of the average crystalline, B is the full width at half maximum (FWHM) in radians and 2θ is the peak position in ($^{\circ}$). Figure 13 exhibits the XRD patterns of the G/ZnO-PANI, G-PANI, ZnO-PANI and RuO₂-PANI nanocomposites. All diffraction peaks observed for RuO₂-PANI in Figure 13 could be indexed to the rutile RuO₂. The sharp peaks for RuO₂-PANI are found at 25, 35, 40, 52 and 55 degrees. This clearly indicates the high crystalline and the existence of rutile phase RuO₂. XRD profile for RuO₂-PANI shows the dominant contribution of [110] peak at 25 $^{\circ}$ compared to the other peaks in the XRD pattern, which are [101], [200], [211], and [220] at 33 $^{\circ}$, 40 $^{\circ}$, 52 $^{\circ}$ and 55 $^{\circ}$. Whereas, the X-ray pattern for ZnO-PANI film exhibits peaks at: 33.03, 38.25, and 69.23 degrees [59]. The average particle size of ZnO-PANI film, from the peak width using Scherrer's equation, was found to be around 50 to 70nm, this is in agreement with the TEM results. The doped ZnO-PANI nanocomposite film reveals better crystallinity than the undoped film. The large angle peak can be observed near 25 degrees, which represents the doped nature of polyaniline. In general, the doping changes the structure of the polyaniline and makes it more crystalline in nature [56].

Addition of graphene to ZnO-PANI nanocomposites also gives rise to a sharp peak at 38 $^{\circ}$ which clearly indicates the presence and crystallinity of the graphene platelets in resultant nanocomposite materials. The most common peaks found for ZnO-PANI and G/ZnO-PANI are [100], [002], [101], [102], [110], [103] at 32,35,39,50 and 56 degrees. The existence of [002] peak at 38 $^{\circ}$ reveals the crystalline structure of ZnO in the polymer network. The X-ray peaks for G-PANI films are observed at 6, 25, 40, and 55 degrees.

The sharp and well-defined peaks at 25° and 38° correspond to [0 0 2] and [100] plane, indicates highly ordered crystal structure with interlayer spacing of 0.336 nm of graphene in G-PANI nanocomposites [52]. The average size of the G-PANI particles was calculated to be around 80 nm to 100 nm [57].

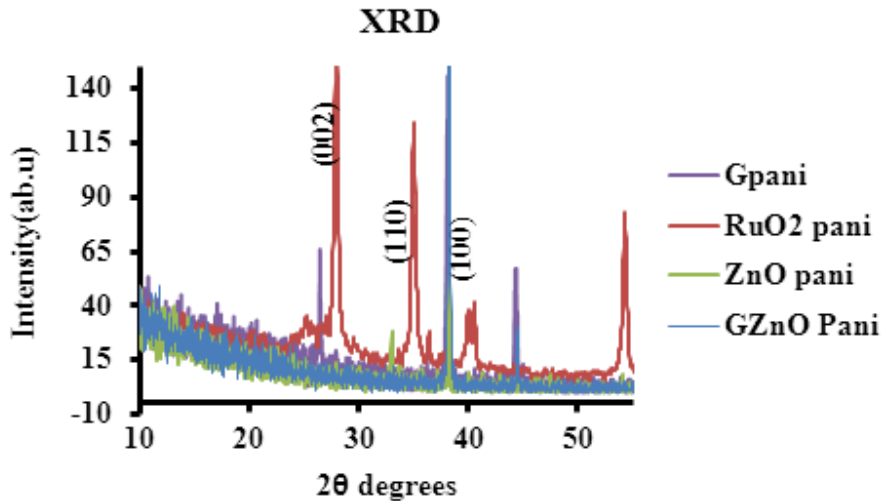


Figure 13. XRD pattern of the G-PANI, ZnO-PANI, G/ZnO-PANI, RuO₂ PANI nanocomposites.

2.4.2.4 FTIR Spectroscopy

Fourier Transform Infrared Spectroscopy technique deals with the infrared region of the electromagnetic spectrum, which is used to identify the presence of chemical compounds present in the material. In this spectroscopy, the infrared rays pass through the sample and finally the information related to perturbation of chemical compounds is collected in the form of spectra. All four samples, exhibit the same benzenoid and quinoid ring vibrations around 1500 cm^{-1} and 1600 cm^{-1} , respectively. A peak around 1306 cm^{-1} is seen in all four samples which is due to the delocalization of the π -electrons in the doped polyaniline polymer. Figure 14 depicts the FTIR spectra of native doped

ZnO-PANI, G-PANI, ZnO/G-PANI and RuO₂-PANI nanocomposites films coated on p-type (100) silicon substrate, respectively. As evident from Figure 14, the FTIR spectra of ZnO-PANI exhibited characteristic bands at: 3445, 3345, 3238, 3074, 2606, 1685, 1516, 1473, 1408, 1329, 1274, 1175, 1188, 1078, 1004, 842, 724, and 508 cm⁻¹. Amongst these, the band at 3445 cm⁻¹ is due to the N-H stretching of PANI in ZnO-PANI. The appearance of peaks at 1516 cm⁻¹ is attributed to the “C=C” stretching of the quinoid and benzenoid rings respectively. The band at 1329 cm⁻¹ is assigned to the emeraldine base structure [58, 59]. Further, the band at 1175 cm⁻¹ is due to the “N=Q=N”, where Q represents the quinoid ring present in the ZnO-PANI nanocomposites.

As shown in Figure 14, ZnO/G-PANI exhibits characteristic bands at 3269, 3094, 2983, 2934, 2871, 2528, 1121, 1590, 1597, 1506, 1314, 1284, 1160, 1031, 894, 839, 721, 687, 619 and at 536 cm⁻¹. Of these, the prominent bands at 1314 cm⁻¹ and 1284 cm⁻¹ attribute to “C-N⁺” stretching of doped PANI. It is very interesting to note, that the band observed at 1380 cm⁻¹ in the ZnO-PANI is shifted to 1314 cm⁻¹ in the ZnO/G-PANI as a result of protonation due to the addition of graphene [57, 59]. Also, the peak observed at 2800 cm⁻¹ in ZnO/G-PANI is due to the presence of N-H groups in PANI molecular chain itself, was not observed in ZnO-PANI. FTIR spectra of G-PANI exhibit its characteristic bands at 2890 cm⁻¹ due to the N-H stretching of PANI in G-PANI film [52].

The appearance of peaks at 1504 and 1594 cm⁻¹ is attributed to the C=C stretching of the quinoid and benzenoid rings, respectively in G-PANI nanocomposites. Further, the band at 1167 cm⁻¹ is due to the N=Q=N, where Q represents the quinoid ring present in the G-PANI nanocomposites [52]. The band at 2800 cm⁻¹ is attributed to the O-H stretching present in polyaniline. Finally, the RuO₂-PANI nanocomposites spectra in

Figure 14 gives also interesting information related to the existence of bands at: 500,850,1180,1300,1500 and 2009 cm^{-1} . The small peak at 500 cm^{-1} is due to influence of hydrous RuO_2 within polyaniline matrix [60].

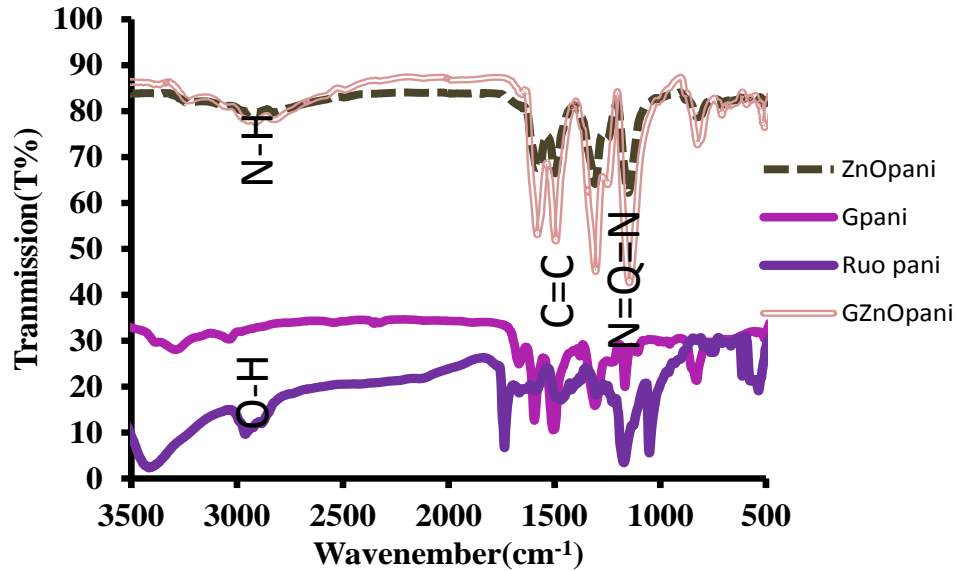


Figure 14. FTIR spectra of the G-PANI, ZnO-PANI, G/ZnO-PANI, RuO_2 PANI nanocomposites.

2.4.2.5 Raman Spectroscopy

Raman spectroscopy is a well renowned spectroscopy approach, which is used to identify the materials by collecting the finger print of the molecules of materials based on their chemical bond vibrations and molecular symmetry. Figure 15 depicts the Raman spectra for all four samples of polyaniline nanocomposites. The Raman spectra for G-PANI shows bands at 1136, 1164, 1192, 1197, 1221, 1244, 1286, 1346, 1375, 1417, 1438, 1494, 1520, 1583, 1614, and 1632 cm^{-1} . The bands at 1583, 1346 and 2690 cm^{-1} are due to D and G graphene peaks, which mainly attribute the distortion in graphene lattice due to the presence in the polyaniline network [52, 57].

The peak at 1375 cm^{-1} present in G-PANI structure reveals that graphene does not only make the nano-composite material, but also can be acting as a dopant in the nanostructure, which is further verified with impedance results. The G-PANI Raman spectrum of ZnO-PANI exhibits bands at 160.2, 441.7, 521.7, 644.4, 842.57, 1194.3, 1258.74, 1358.7, 1421.4, 1513.8, 1590.4, 1617.3, 1942.5, and broad peak at 2019.3-2758. The characteristic of polyaniline can be observed by broad, asymmetric bands at 1600-1700 cm^{-1} . However, Raman spectrum for the ZnO/G-PANI nanocomposite shows peak positions at: 148.2, 434.9, 523.3, 820, 978.5, 1175.5, 1238.1, 1289.3, 1366.39, 1426.01, 1506, 1581.4, 1618.72, 1988.1, 2400.1, 2672.6, 3095.65, and a broad peak from 2548-3200. The Raman spectrum is progressive, which implies that the G/ZnO-PANI in doped states is either bipolaronic form or polaron lattice, isolated polarons, as well as, partially charged “C-N” sites or “C=N” sites with a bond order between ZnO- PANI and G/ZnO-PANI films [59]. One can therefore expect a change in the “polaron band” wave number according to whether the maximum or only a partial charge is localized on N, as well as change in the amine band wave number as a function of charge on the nitrogen [52, 59]. We are therefore interested in the two bands at 1330 and 1490 cm^{-1} which are the characteristic of “-C-N⁺” and “C=N” stretchings as a function of charge localization in the doped form of polyaniline. In last the Raman spectra of RuO₂-PANI nanocomposites reveal the bands at peaks: 535, 690, 730, 1000, 1250 and 1500 cm^{-1} . Of these the bands at 535, 660 and 720 represent the single crystal RuO₂ modes named E_g, A_{1g}, and B_{2g}, respectively. However, peaks at 600 and 700 cm^{-1} are due to Ru⁴⁺-O and Ru³⁺-O bonds present in RuO₂-PANI nanocomposites [60]. The detailed study of structural characterization is discussed above, for Raman, FTIR, XRD, SEM and TEM techniques

reveal the successful synthesis of PANI nanocomposite materials using the facile polymerization approach.

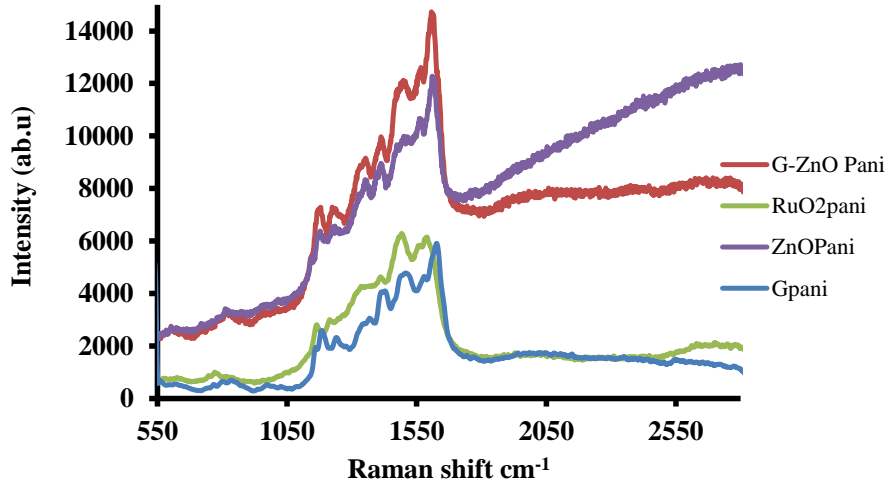


Figure 15. Raman spectra of the G-PANI, ZnO-PANI, G/ZnO-PANI, RuO₂ PANI nanocomposites.

2.5 Electrode Preparation and Cell Assembly of Supercapacitor

A three-electrode electrochemical cell system was used to evaluate the electrochemical performance of polyaniline nanocomposites by Cyclic Voltammetry (CV), Electrochemical Impedance Spectroscopy (EIS), and galvanostatic charge-discharge techniques on an Auto lab PGSTAT302N work station at room temperature. The working electrodes were prepared by mixing the G/ZnO/RuO₂-PANI nanocomposite films in N-methyl-2-pyrrolidone (NMP), which was followed by sonication for 20 minutes and later it was stirred for 12 hours. After mixing well, the solution was casted over the graphite electrode and dried at 80°C for 1hr in a controlled temperature oven. For comparison study, the size of the electrode and thickness of the film was kept the same for all four samples, which is around 1cm² and 30microns. Other than working electrode, an Ag/AgCl was used as a reference electrode and platinum sheet was used as

an auxiliary electrode. The schematic of an electrochemical cell used for the electrochemical measurements for supercapacitor electrodes of G-PANI, ZnO-PANI, G/ZnO-PANI and RuO₂-PANI nanocomposites is given in Figure 16. Besides the cell assembly for supercapacitor, Figure 16 also explains the charging and discharging mechanism in the supercapacitor. As explained in Figure 16, during the charging of the supercapacitor the electrons flow toward the counter electrode through external load, while ion moves in the opposite direction to working electrode through electrolyte. Whereas during discharging the electrons flows in reverse direction from counter to working electrode and ions in electrolyte follows the path towards the counter electrode.

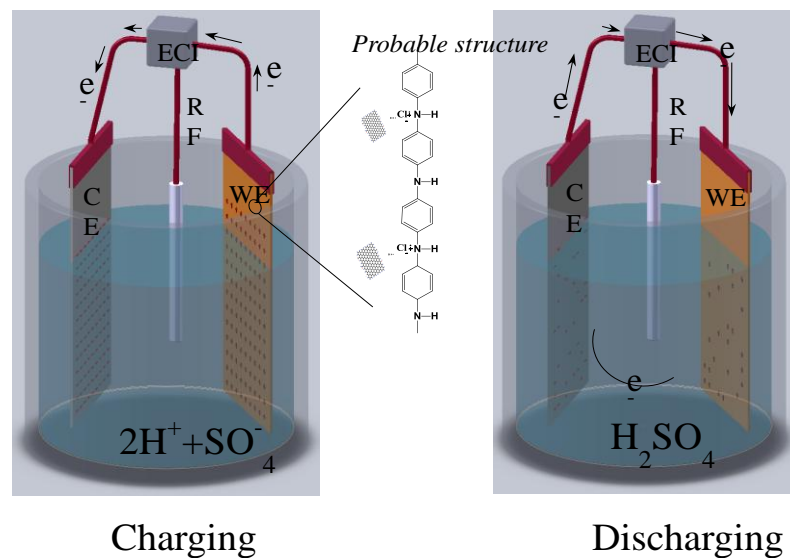


Figure 16. Schematic of supercapacitor electrodes for electrochemical measurements.

2.6 Electrochemical Characterization

2.6.1 Cyclic Voltammetry (CV)

Cyclic voltammetry is a widely used electrochemical technique to investigate the role of thermodynamics and electron transfer kinetics at the interface of the electrode and electrolyte for supercapacitor and Li-ion battery application. In cyclic voltammetry, the electrochemical cell is cycled in a particular potential window, where the potential is applied to the working electrode and measured for different scan rates. Scan rate is defined as the change in potential versus time. The electrochemical performance of material can be evaluated by observing the current change in a cathodic and anodic scan. Figure 17 exhibits the CV profile of the four samples, ZnO-PANI, G/ZnO-PANI RuO₂-PANI and G-PANI film, on graphite electrodes at scan rates (5, 20, 50, and 100 mV/s) performed in 2MH₂SO₄ to understand the conducting polymer (CPs) redox processes. Figure 17(a&b) shows the oxidation and reduction characteristic peaks for ZnO-PANI and G/ZnO-PANI nanocomposites at around 0.2, 0.3, 0.5, 0.45 0.6V and 0.7, 0.45, 0.40V. The 0.2V peak attributes to the oxidation of the emeraldine form of PANI whereas the peak at 0.7V is due to the pernigraniline form of PANI otherwise known as protonation. The peak at 0.5V corresponds to anodic dissolution, the one at 0.45V corresponds to the reduction of zincate. However, the peak at 0.5V can be attributed to the oxidation of ZnO in the acidic medium [59, 61]. From these results, it is obvious that the ZnO-PANI nanocomposite retains its individual redox property by exhibiting the individual voltammetry characteristic at the appropriate potential. In comparison to ZnO-PANI, G/ZnO-PANI, RuO₂-PANI, the CV profile of G-PANI shows a larger rectangular area, which simply describes the higher electrochemical response or the presence of

higher electroactive elements in the G-PANI nanocomposites, this leads in achieving the higher specific capacitance in supercapacitor.

The oxidation and reduction peaks for RuO₂-PANI and G-PANI are noticed at 0.2, 0.4, 0.6, 0.7V and 0.45, 0.3, 0.2, -0.1V in Figure 17(c & d). The current-voltage relation of RuO₂-PANI films also reflects the successful doping or protonation of PANI within RuO₂ particles due to the presence of 0.6V and 0.7V peaks potential. Nevertheless the existence of a distinct peak centered at 0.6V and 0.3V associates to the reversible oxidation and reduction of graphene sheets within polyaniline in G-PANI films [52, 57, 62]. For instance, graphene plays an interesting role in a diffusion controlled behavior of ions due to its unique electrochemical property and higher conductivity induced by doping mechanism.

The plot between current density versus the square root of the scan rate gives the straight line for all four polyaniline nanocomposites, which indicates a diffusion-controlled process at ZnO-PANI, G/ZnO-PANI, RuO₂-PANI and G-PANI electrode and electrolyte interfaces. Moreover, the diffusion coefficient for all the polyaniline nanocomposites explained above has been calculated using Randles-Sevick equation, which is given as following [51, 58, 59].

$$I_p = (2.687 \times 10^5) n^{3/2} A D_0^{1/2} C v^{1/2} \quad (10)$$

where n is the number of electrons transferred in the reaction, A is the electrode area, C is the concentration of the diffusing species in the bulk of the electrolyte, and v is the sweep potential rate. By using the values of $n = 2$ and $C = 0.2 \text{ M H}_2\text{SO}_4$, the diffusion coefficient D_0 calculated for ZnO-PANI, G/ZnO-PANI, RuO₂-PANI and G-PANI is given in Table 4.

Table 4. Diffusion coefficients of polyaniline nanocomposites.

Materials	(D ₀) Diffusion coefficients cm ² /sec
ZnO-PANI	0.7×10^{-10}
G/ZnO-PANI	0.8×10^{-9}
RuO ₂ -PANI	3×10^{-8}
G-PANI	8×10^{-8}

It is shown that the diffusion coefficient of the G-PANI material is two orders of magnitude higher than the other polyaniline nanocomposites used as for supercapacitor electrode. This simply attributes the superior electrochemical characteristic due to the large surface area, greater flexibility, higher conductivity, and porosity of G-PANI nanocomposites compared to ZnO-PANI, G/ZnO- PANI and RuO₂-PANI nanocomposite material, which simply contributes in the enhancement of specific capacitance and the stability of supercapacitor device.

The specific capacitance comparison study of ZnO-PANI, G/ZnO-PANI RuO₂-PANI and G- PANI nanocomposites at scan rates (5, 25, 50 and 100 mV/s) is shown in Figure 17(e). At the higher scan rate specific capacitance of nanocomposites decreases which may be the reason for diffusion limitations in the electrode and therefore the maximum area of electrode remains inaccessible. This simply tells that the observed specific capacitance calculated for G-PANI material is higher than the rest of nanocomposites materials, the relation between specific capacitance and scan rate tends

to decrease linearly, however, the rate of decrease in the specific capacitance in G-PANI film is slower due to the higher electrochemical stability of graphene than other nanocomposites. The following equation was used to calculate the specific capacitance using CV profile.

$$C = \frac{I}{s} \quad (11)$$

where C is specific capacitance, I is the specific current and s is the scan rate. The maximum capacitance obtained for ZnO-PANI, G/ZnO-PANI RuO₂-PANI and G-PANI nanocomposites at a scan rate of 5mv/sec is (280F/g, 300F/g, 360F/g and 430F/g) respectively.

2.6.2 Electrochemical Impedance Spectroscopy (EIS)

Impedance spectroscopy is a technique which studies the behavior of small potential perturbations at different frequencies at a constant dc potential. An impedance spectrum normally divides into three regions, which are described as low frequency, medium frequency and high frequency region. The small semicircle is observed in the high frequency region, which arises due to the kinetic phenomena and charge transfer resistance and double layer capacitance. Whereas, in low frequency the formation of the tail at a certain angle is due to the diffusion mechanism of ions in material, for the ideal supercapacitor the tail should be parallel to the y-axis. The Nyquist spectra for G/ZnO-PANI, G-PANI, ZnO-PANI and RuO₂-PANI nanocomposites was recorded in the frequency range of 100mHz to 100KHz at room temperature is shown in Figure 18.

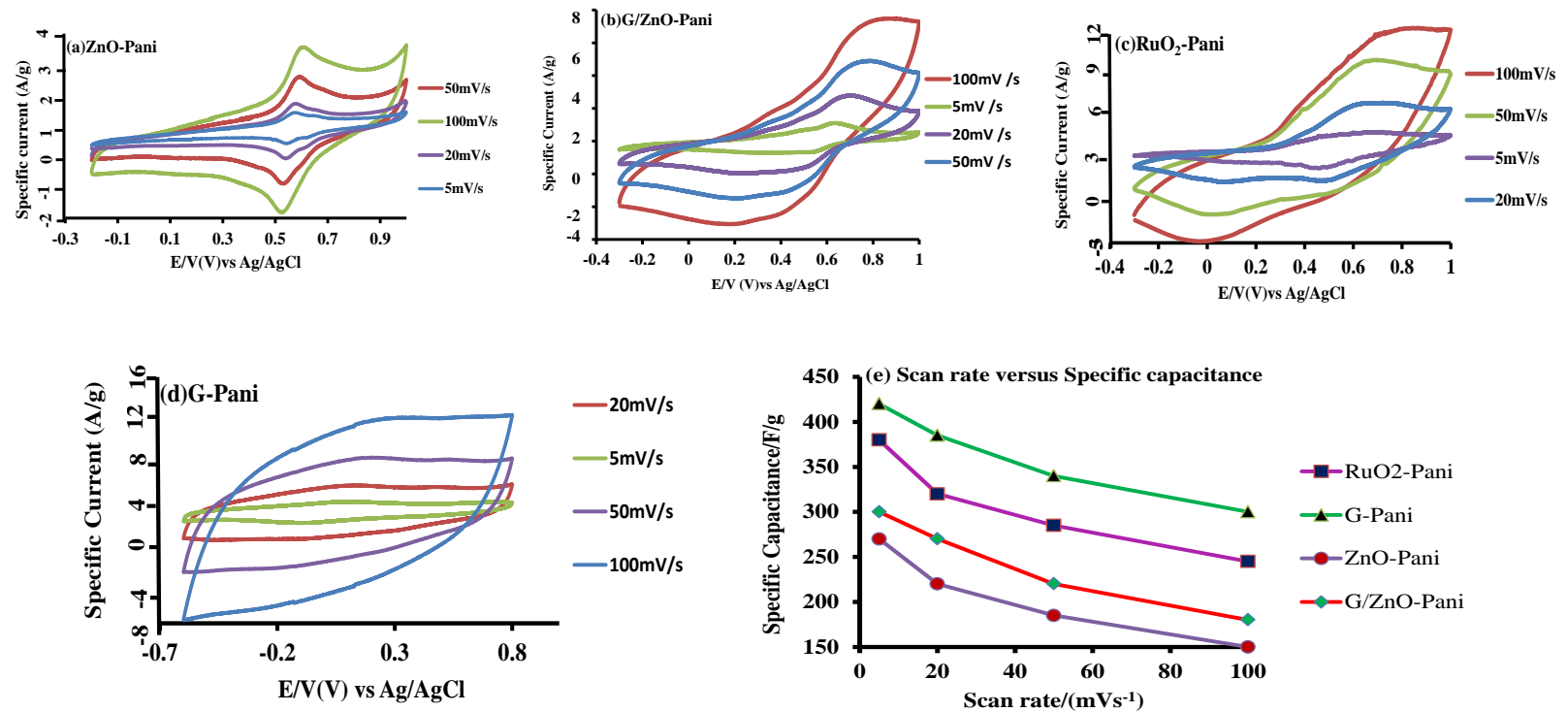


Figure 17. CV responses of (a) ZnO-PANI (b) G/ZnO-PANI (c) RuO₂-PANI (d) G-PANI at scan rates (5, 20, 50, 100 mV/s) (e) Scan rate versus specific capacitance

The Nyquist plot of ZnO-PANI demonstrates two well-defined portions, a smaller semicircle in higher frequency and a straight line over the low frequency region. The semicircle in the plot ascribes to the electron transfer rate at the interface of the electrode and electrolyte. Interfacial polarization resistance of the electrode and electrolyte cause the formation of the linear part of the plot [63]. Moreover, it is evident from Figure 18 that the ZnO presence has shown typical behavior of any redox species occurring due to the presence of PANI. The Nyquist plot of G/ZnO-PANI also shows the desired straight line curve for the low frequency region, but the presence of the small semicircle at high frequency is missing as it was observed in ZnO-PANI. However, the lower resistance in G/ZnO-PANI plot is indicative that the addition of graphene in ZnO-PANI has increased the conductivity of the film, which enhances the diffusion controlled process, as well as it offers less charge resistance. Similarly, the small semicircle in the lower frequency region also was not seen in RuO₂-PANI and G-PANI plots, which might be due to the low faradic resistances of the material. The charge transfer resistance, R_{ct} , of ZnO-PANI, G/ZnO-PANI, RuO₂-PANI and G-PANI, are found to be equal to 65, 20, 15 and 1 Ω . The lower charge transfer resistance in the G-PANI film associates with the higher conductivity, as well as, the large surface area of the films, which is very characteristic of graphene. In the impedance plot of ZnO-PANI, G/ZnO-PANI, and RuO₂-PANI straight line angle close to 45° is observed, indicating typical Warburg impedance influence. However in the G-PANI plot, the straight line angle is inclined towards 90°, which is the typical ideal EIS curve for supercapacitors. The low charge transfer resistance and following the trend for the ideal supercapacitor curve exhibited by G-PANI film compared to ZnO-PANI, G/ZnO-PANI, and RuO₂-PANI in 2M H₂SO₄ confirms the

superior electrochemical characteristics of synthesized material [64].

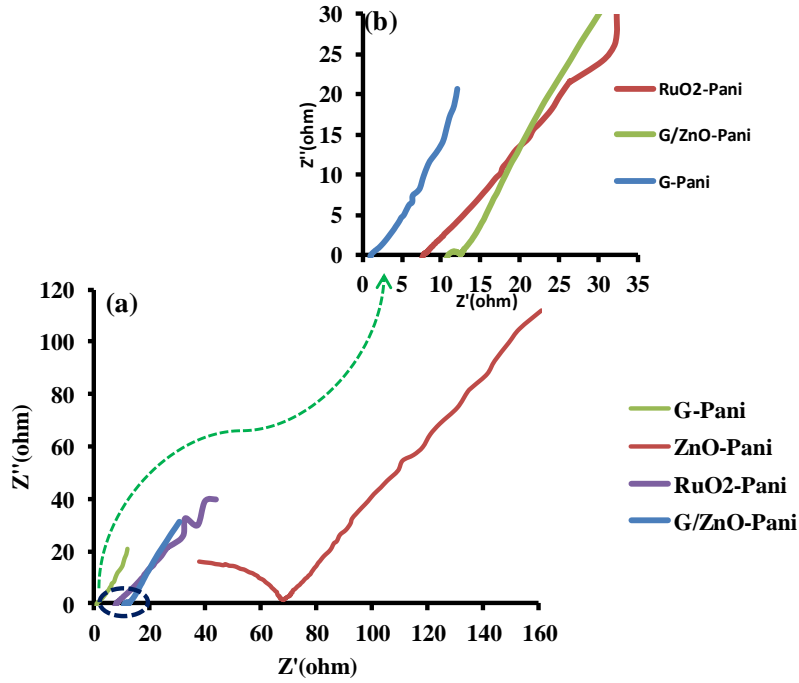


Figure 18. EIS analysis of(a) ZnO-PANI, G/ZnO-PANI, RuO₂-PANI , G-PANI and (b) G/ZnO-PANI, RuO₂-PANI , G-PANI.

2.6.3 Galvanostatic Charge & Discharge

The galvanostatic charge & discharge test was conducted at a given current density. The amount of charge capacity (Q) is calculated by using the formula.

$$Q = I \times t \quad (12)$$

where I is the current density and t is time. Figure 19(a) demonstrates the galvanostatic charge-discharge curves for ZnO-PANI, G/ZnO-PANI, RuO₂-PANI and G-PANI films at a charging/discharging current density of 0.2 A/g. All charge/discharge curves for ZnO-PANI, G/ZnO-PANI, RuO₂-PANI and G-PANI are based on supercapacitor are triangular in-shape, which attributes the pure electric double layer (EDL) capacitance of polyaniline nanocomposites [52, 64, 65]. The prominent voltage stages are observed in

the G-PANI film, which is in the ranges of 1.6-1.2V and 1.2-0V, respectively. The discharging duration for 1.6-1.2V is relatively short, which ascribes to EDL capacitance; whereas a much longer discharging duration from 1.2-0 V associates with the combination of EDL and faradic capacitances of G-PANI synergistic effect.

The discharge curve of the supercapacitor with G-PANI films is similar to that of ZnO-PANI, G/ZnO-PANI, and RuO₂-PANI. However, the “IR drop” in G-PANI compared to other nanocomposites is much smaller. This result reveals that the internal resistance in G-PANI film is much lower than other polyaniline nanocomposite electrodes, which is of great importance in fabricating safe and power saving supercapacitors. From the above comparison, it is understood that the incorporation of conducting graphene platelets in the polyaniline network not only helps in providing the stability, but also renders high conductivity to the synthesized structure. The following formula was used to calculate the specific capacitance using the charging-discharging curve for ZnO-PANI, G/ZnO-PANI, RuO₂-PANI and G-PANI films [65].

$$C = \frac{I \cdot \Delta V}{\Delta t \cdot m} \quad (13)$$

where C is specific discharge capacitance, ΔV is a potential difference (V) Δt is discharging time(s), and m is the weight of film (g) and I is the discharge current (A). By keeping the film weight of all four samples are the same which is around 3mg, specific capacitance values, were obtained using equation 12 for ZnO-PANI, G/ZnO-PANI, and RuO₂-PANI and G-PANI is 260 F/g, 300 F/g, 330 F/g and 380 F/g, which is in agreement with the specific capacitance values calculated by the cyclic voltammogram (CV).

Moreover, the G-PANI film possesses a much higher volumetric capacitance than that of ZnO-PANI, G/ZnO-PANI, and RuO₂-PANI films owing to its more compact

structure, showing high merits in potential applications for low-volume high capacitance devices [52, 64]. The rate of performance for ZnO-PANI, G/ZnO-PANI, RuO₂-PANI and G-PANI films was evaluated by charging/discharging for different cycle's numbers at a constant current density 0.2A/g is shown in Figure 19(b). The cycle stability of all four polyaniline nanocomposites shows some decrease in specific capacitance over the 400 number of cycles. This might be due to the increase in volume of the electrode materials during charging-discharging for number of cycles and then enhances the series resistance at the electrode and electrolyte interface [57]. It is important to note that G-PANI films compared to ZnO-PANI, G/ZnO- PANI, and RuO₂- PANI show good consistency in the specific capacitance beyond the 400 number of cycles, which is an evidence of superior mechanical properties of graphene within polyaniline matrix.

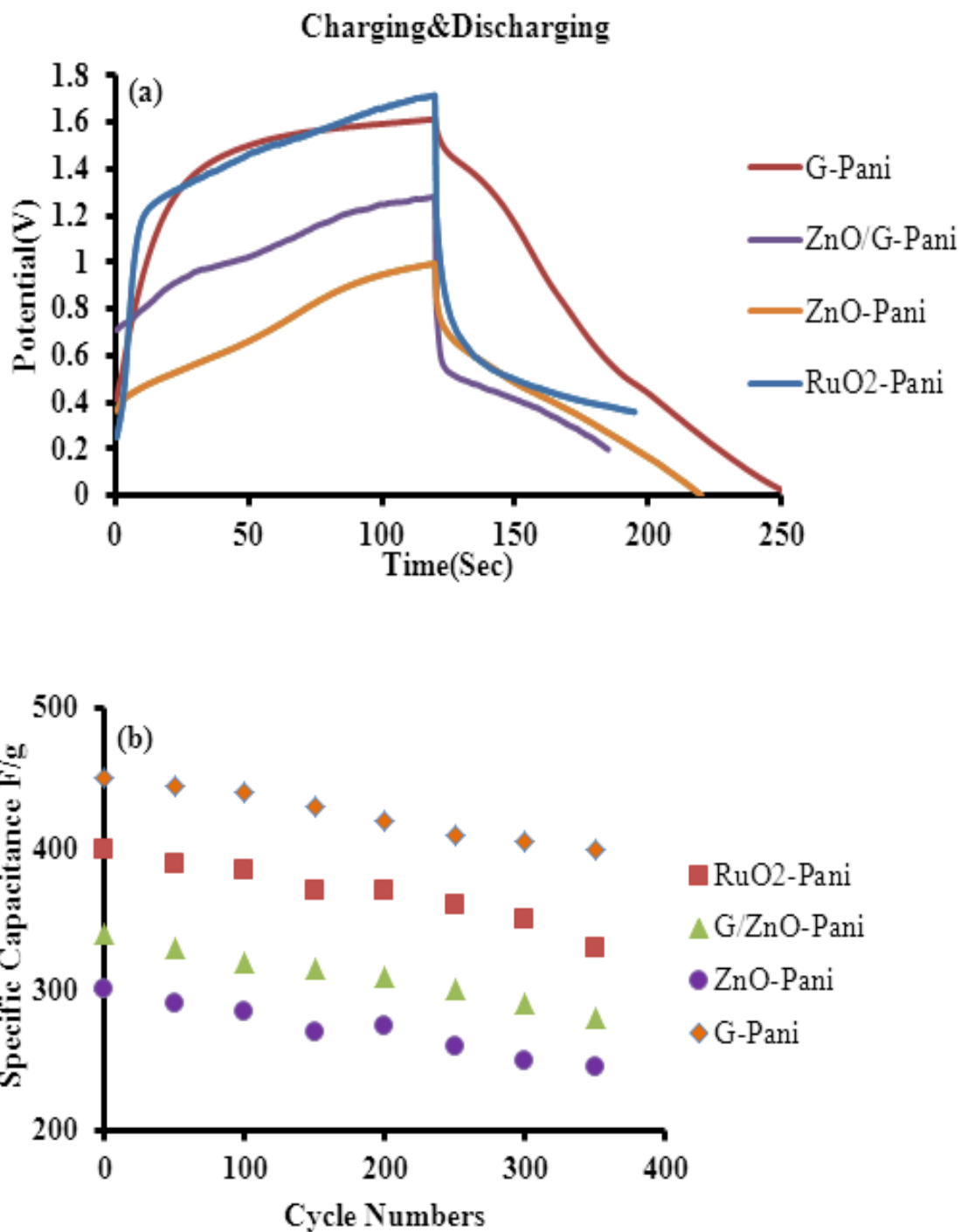


Figure 19. (a) Charging & discharging profile and (b) cycle numbers versus specific capacitance of polyaniline nanocomposites.

2.7 Summary

Aromatic based conducting polymer nanocomposites were synthesized by means of chemical polymerization. The important features of this method are the simple approach, low energy consumption, inexpensive, substrate independent and environmental friendliness. The successful synthesis of aromatic based conducting polymer nanocomposites were investigated in detail using physical and structural techniques. Prepared materials were used in supercapacitor electrode assembly to evaluate the electrochemical behavior in 2MH₂SO₄. Electrochemical measurements for all polyaniline nanocomposites reveal the promising potential of the synthesized materials for the application of supercapacitor. However, G-PANI in comparison of ZnO-PANI, G/ZnO-PANI and RuO₂-PANI, showed maximum specific capacitance and greater cyclic stability. This can be attributed to the superior electrochemical performance and higher structural hierarchy of G-PANI due to the significant doping of graphene (G) in the polyaniline network.

CHAPTER 3: INFLUENCE OF GRAPHENE COMPOSITION ON G-PANI BASED ELECTROCHEMICAL CAPACITOR

3.1 Introduction

Graphene conducting polymer nanocomposites, G-CP,s have gained immense attention due to the excellent electrochemical properties of the G-CPs. Electron movement has been observed ballistically in the graphene layer at ambient temperatures due to the high quality of the sp_2 carbon lattice. Among all of the materials so far used in the supercapacitor, the graphene has attracted prominent attention in recent years, due to its extraordinary high thermal and electrical conductivities, large surface area and flexibility, great mechanical strength, relatively low manufacturing cost and environmental benignness [66]. Though PANI has a low redox potential and has been reported to undergo fast redox reactions, where the charging reaction is found to be faster than discharging reaction, but the G-PANI nanocomposite enhances the electrochemical and mechanical stability of polyaniline as well. Interesting properties of G-CP have made it the material of choice not only for the supercapacitor but also for the other advanced electronic applications (e.g., sensors, transparent electrodes, supramolecular assemblies and lithium ion battery.)

However, to obtain the maximum advantage of synthesized G-PANI material, the right proportion of graphene to polyaniline is very important. People have already reported the different weight percent amounts of graphene to polyaniline nanofibers for the use of the supercapacitor [57, 67]. Contrary to polyaniline nanoparticles, though

polyaniline nanofibers have superior electron transport and electrochemical behavior it still has limitations (e.g. mechanical stability upon cycling, high aspect ratio, large surface area and solubility of nanofibers) As an alternative to polyaniline nanofibers we have synthesized the polyaniline nanoparticles with different ratios of graphene to optimize the electrochemical response of prepared material. In addition to the graphene-polyaniline ratio the thickness of the prepared G-PANI film is also a critical factor to obtaining maximum specific capacitance of a device. Therefore, in this chapter we will be discussing the influence of graphene within the polyaniline matrix and the desired thickness of material to optimize the performance of the supercapacitor.

3.2 Experiment

The graphene-polyaniline nanocomposites (G-PANI) were synthesized as described above in section 2.4. The same polymerization method was used to synthesize the different weight ratios of G-CPs nanocomposite. We synthesized three materials keeping the weight. ratio of graphene to the aniline monomer as (50:50, 10:90, and 90:10). The ammonium peroxydisulfate $[(\text{NH}_4)_2\text{S}_2\text{O}_8]$ amount was kept the same during the three sample preparation 0.025M to the aniline monomer. While keeping the (50:50, 10:90, and 90:10) weight percent ratio of graphene to the aniline monomer, it was added in 2M HCl solution of 200ml, The solution was further cooled down to 4°C in an ice bath. Later $[(\text{NH}_4)_2\text{S}_2\text{O}_8]$ (0.025M) dissolved separately in 100 ml of 1MHCl solution was added drop wise in the above graphene-aniline solution over the period of 1hour while keeping the controlled temperature less than 10°C. The polymerization process was observed within 5 minutes after the addition of ammonium peroxydisulfate, when the solution starts changing its color from bluish-black to a dark green shade. Once the

polymerization was complete the ice bath was removed around the vessel. Finally, after stirring for 24 hours, the dark green precipitate of G-PANI nanocomposites, recovered from the reaction vessel, was filtered, and washed using deionized water, methanol, acetone, and diethyl ether for the elimination of the low molecular weight oligomer. Later, the doped G-PANI nanocomposites were undoped by mixing it in a 2MNaOH solution for 6hours. In the end, blue precipitate material of G-PANI nanocomposites were collected after washing with methanol and deionized water several times [52, 68].

3.3 Structural Characterization

3.3.1 Scanning Electron Microscopy (SEM)

Figure 20 shows the SEM picture of PANI, graphene and G-PANI films on graphite substrates of an area of 1 cm². All the prepared materials were first dissolved in 1-methyl-2-pyrrolidionone (NMP) and were later drop cast on the graphite substrate to ensure the same thickness of material. Figure 20(a) shows the homogeneous fine morphological structure for PANI whereas Figure 20(b) reveals the overlapping platelet structure due to the presence of graphene sheets. In addition to graphene and PANI Figure 20(c, d and e) presents the G-PANI10, G-PANI50 and G-PANI90 images which depict a combined morphology of graphene as well as of PANI. Nevertheless G-CPs shows a smoother, flexible and fine structure since 1-methyl-2-pyrrolidionone (NMP) solvent is used as a plasticizer. Interestingly different weight ratios of G-PANI do not depict any significant difference in morphology rather than a variation in an amount of graphene has been observed. Random agglomeration of graphene platelets on polymer surface is also observed for G-CPs samples [52, 69].

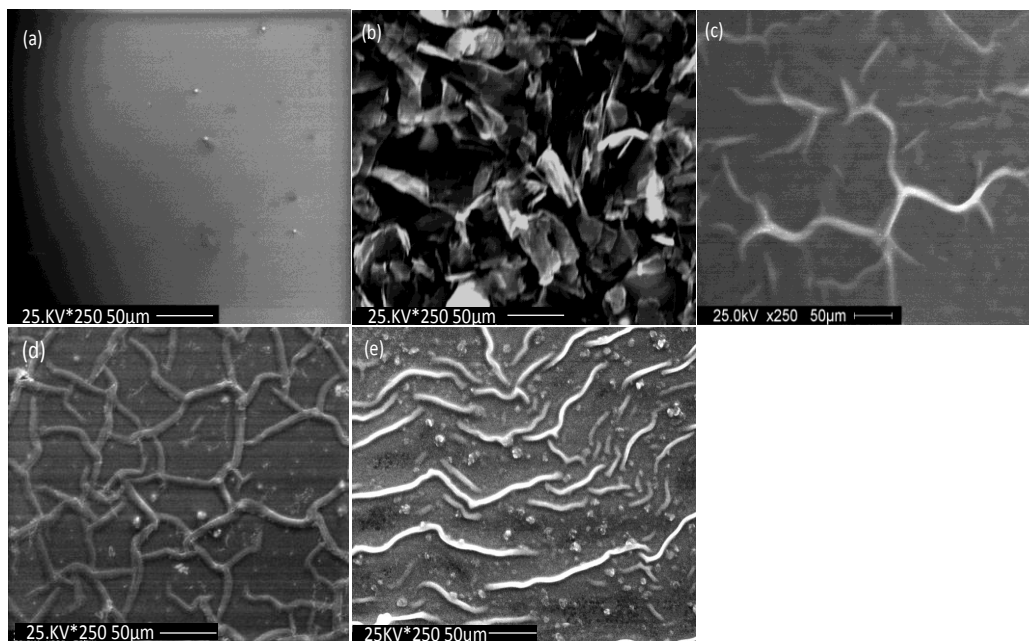


Figure 20. SEM images of (a) PANI (b) graphene and (c) G-PANI10 (d) G-PANI50 (e) G-PANI90.

3.3.2 Transmission Electron Microscopy (TEM)

TEM results of graphene, PANI, and G-PANI nanocomposites of ratio (10, 50, and 90) are given in Figure 21 (a, b, c, d, e). The graphene shows the typical curves and layers like structure with the size of a few nanometers. The agglomeration of particles within graphene sheets can also be observed in the TEM image. SAED pattern of graphene in Figure 21(a) inset shows good crystallinity character of graphene sheets. However the TEM image of PANI in Figure 21(b) shows an amorphous nature of PANI and not any specific crystalline order was observed for the PANI sample. Furthermore the TEM of G-PANI nanocomposites of weight ratios (10, 50, and 90) are shown in Figure 21(c, d, e) reveals almost the same kind of morphology structure except the variation in the amount of graphene. TEM of all G-CPs shows some order of crystallinity due to the presence of graphene sheets in the synthesized material. Homogenous encapsulation of

graphene sheets within PANI particles are noticed in G-PANI TEM images [52, 57, 70]. This simply explains the porosity and flexibility of G-PANI material due to the synergetic effects of polyaniline and graphene, which is quite promising in achieving high specific capacitance in ECs.

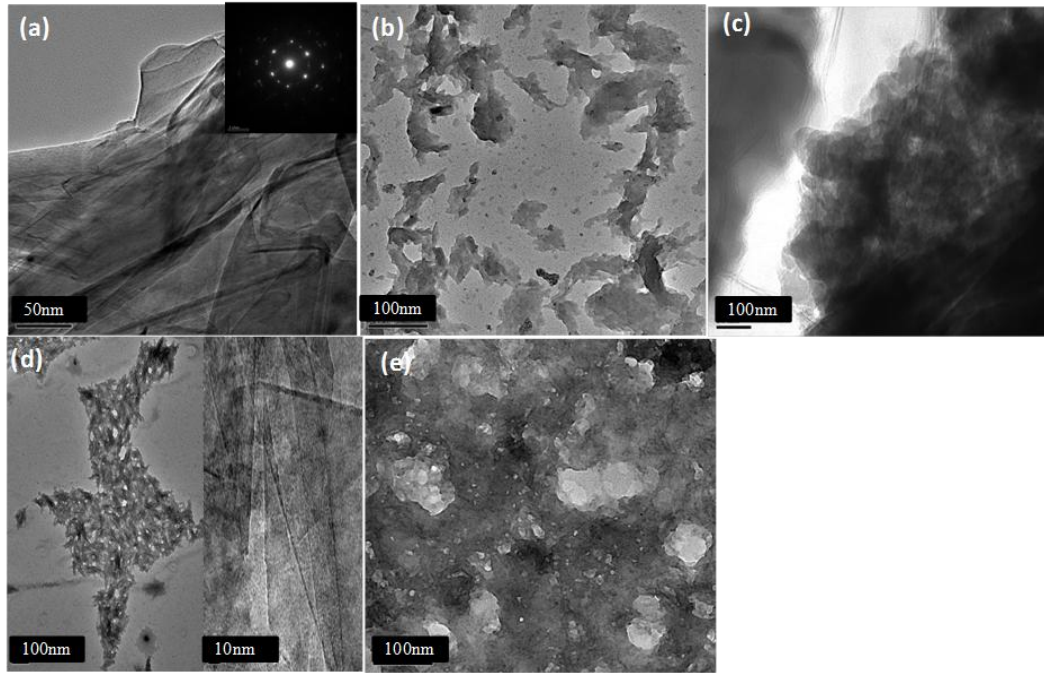


Figure 21. TEM images of (a) graphene (b) PANI (c) G-PANI10 (d) G-PANI50 (e) G-PANI90.

3.3.3 XRD

The XRD patterns of PANI and G-PANI films are shown in Figure 22. It is observed that PANI exhibits a broad peak around 15 to 20 degrees, indicating an amorphous structure. However, the G-PANI nanocomposites reveal a sharp and intensive peak at 26.5 degree, corresponding to the (0 0 2) plane, which indicates a highly ordered crystal structure of graphene with an interlayer spacing of 0.336 nm. However, the position of this peak and its intensity vary slightly from sample to sample, depending on the number of layers and the composition of graphene to aniline monomer. The diffraction intensity in Figure 22 at

26.5 and 37 degrees corresponds to planes (0 0 2) and (1 0 0) indicative of the presence of the graphene in the nanocomposites structure [71, 72]. The calculated size of G-PANI nanoparticles using Scherrer's equation was found to be around 50 to 90nm which kept increasing with the addition of graphene within the polyaniline. This value of G-PANI nanoparticle size is consistent with the TEM results.

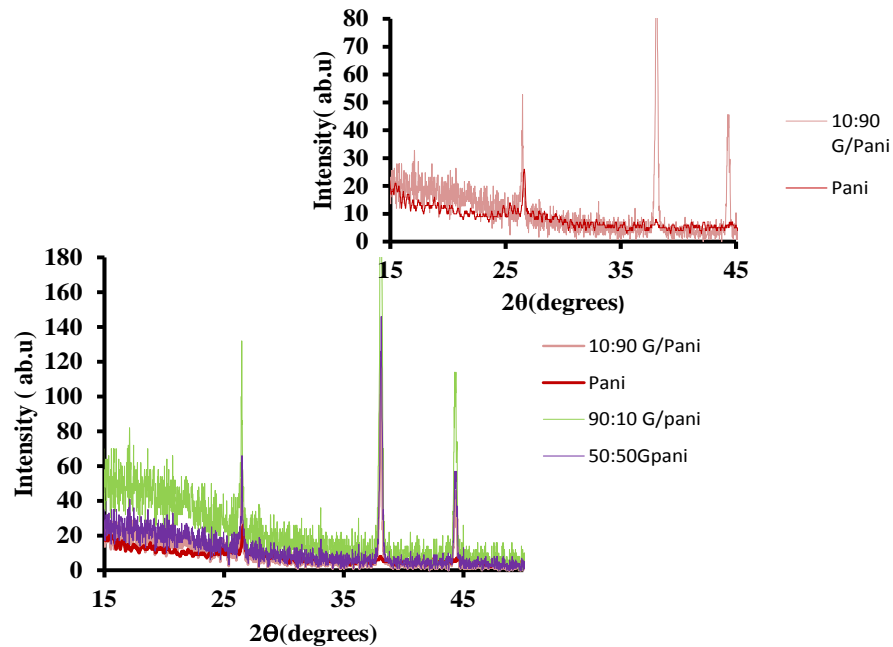


Figure 22. XRD spectra of PANI, and G-PANI (10:90, 50:50, 90:10) nanocomposites.

3.3.4 Raman Spectroscopy

It is significant to have a Raman spectra study for PANI and G-PANI (10:90, 50:50, 90:10) nanocomposites materials on the silicon substrate due to their distinctive identification in the structures as shown in Figure 23. Figure 23 shows the appearance of bands at 1600, 1545, 1450, 1350, 1295, 1250, 1237 and 1151 cm^{-1} corresponding to characteristic bands of PANI structure [72]. The agglomeration of graphene sheets is also

confirmed with Raman spectroscopy as shown in Figure 23. Two characteristic peaks at 1300 and 1582 cm^{-1} are corresponding to the D and G bands of graphene respectively [73-76]. The G band of our sample is relatively intense compared to the D band for G-PANI50 and G-PANI90 ratio. The observed intensity change is due to a multilayer of graphene in the nanocomposites structure.

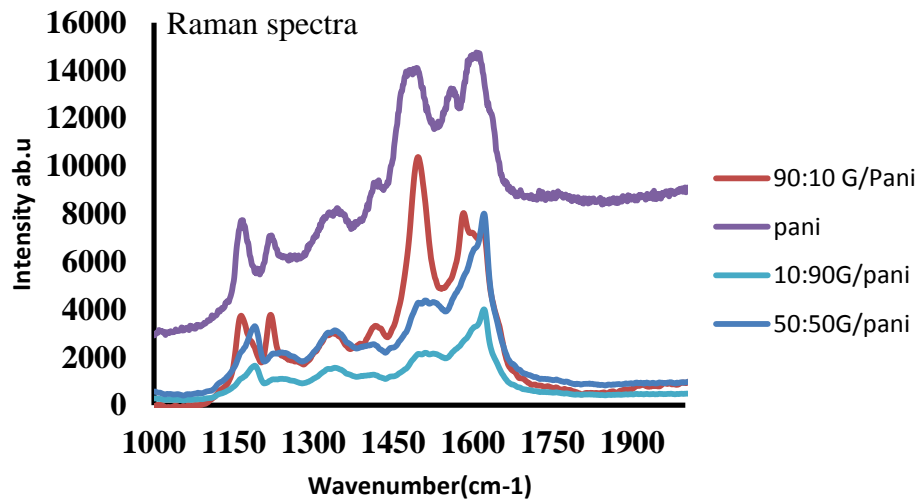


Figure 23. Raman spectra of PANI, and G-PANI (10:90, 50:50, 90:10) nanocomposites.

3.4 Electrochemical Evaluation

3.4.1 Electrode Preparation

In order to study the electrochemical response of prepared G-PANI nanocomposites for supercapacitor application, two electrodes of each material of the same thickness and area are prepared by mixing the materials in NMP while kept on stirring for 12 hours. One electrode is used as a cathode and another is used as an anode by providing negative and positive potential in supercapacitor cell assembly. All electrochemical measurements for the prepared electrodes were carried out at room temperature.

3.4.2 Capacitance Evaluation of G-PANI Films with Different Composition of Graphene

3.4.2.1 CV

The CV response of prepared G-PANI films of different weight ratios, coated on graphite has been studied in $2\text{MH}_2\text{SO}_4$ is shown in Figure 24(a). Figure 24(a) compares the cyclic voltammetry response of PANI, graphene, and G-PANI films of different ratios but of identical film thickness, at a scan rate of 5mV/s . One can see that in Figure 24(a), all CV curves are in deformed rectangular shape due to the combined effect of two materials graphene and polyaniline in the voltage window of -0.7 to 1.0V . The deformed CV shape of PANI shows the oxidation and reduction peaks potential at 0.3 , 0.5 and 0.3V due to the characteristic of redox potential of PANI, whereas the CV response of graphene does not show any significant peak and has a slightly narrow surface area. By comparison the CV curves of G-PANI50 show significant higher specific capacitance than G-PANI10 and G-PANI90 samples as depicted in Figure 24(a). It is attributed to the larger CV area and higher porosity besides the higher electronic conductivity of G-PANI 50 sample.

In the CV profile of G-PANI50 and G-PANI10 oxidation potential peaks are observed at 0.3 , 0.4 , -0.2 , -0.1V and reduction peaks at around 0.6 , 0.45 , -0.05V . Nevertheless no significant oxidation peak was observed for the G-PANI90 sample since it reflects more EDL behavior. The detailed reason obtaining a lower specific capacitance (SC) for G-PANI10 may be due to the low electronic conductivity of material which provides limitations in electronic and ionic diffusion and reduces the overall performance of a device. Similarly the lower SC in G-PANI90 sample attributes due to the dominant influence of graphene which leads to high resistance due to the excessive grain

boundaries of graphene in prepared material. The above discussion indicates that the right amount of graphene content within the polymer network is quite important to obtain the optimum capacitive behavior of G-PANI films.

$$C = \frac{I}{s(m_1+m_2)} \quad (14)$$

For all samples the specific capacitance was calculated by using equation 14 where I is the current density and $(m_1 + m_2)$ is the sum of mass of two electrodes and s is scan rate. The specific capacitance calculated from Figure 24(b) shows the variation in specific capacitance of G-PANI50 film as 250, 290, 340 and 390 F/g at scan rates 100, 50, 20 and 5mV/s. At a smaller scan rate, the electrolyte ions access to the maximum inner surface area of the electrode and gives rise to higher specific capacitance, whereas at a higher scan rate inner pores of films might not be accessed effectively by ions which helps in increasing the electrode resistance, additionally decreasing the specific capacitance. The increase in CV response at different scan rates explains that electrochemical kinetics is controlled by a diffusion controlled mechanism for G-PANI nanocomposites material.

One can understand the discussion that specific capacitance of G-PANI film does not increases with the increase in total surface area rather that it is relevant to the proper pore size, porosity and ionic and electronic conductivity of the films respectively. It is observed that specific capacitance of all G-PANI samples monotonically decreased with increasing scan rate and is shown in Figure 25. However the specific capacitance decreasing rate in G-PANI50 and G-PANI10 electrodes compare to G-PANI90 films is significant lower. It clearly indicates the good electrochemical stability of graphene in the

polymer which helps in improving the performance of EC. Whereas the decreasing rate of SC versus scan rate in G-PANI90 films is significantly high due to the influence of redox characteristic of PANI and ESR arises from the excess amount of graphene. The calculated specific capacitance for all three ratios of G-PANI films at a scan rate of 5mV/s is given in table 5.

Table 5. Specific capacitance for PANI, graphene, G-PANI (10:90, 50:50, 90:10) nanocomposites.

Material	Specific Capacitance F/g
PANI	230
Graphene	130
G-PANI10	300
G-PANI50	370
G-PANI90	270

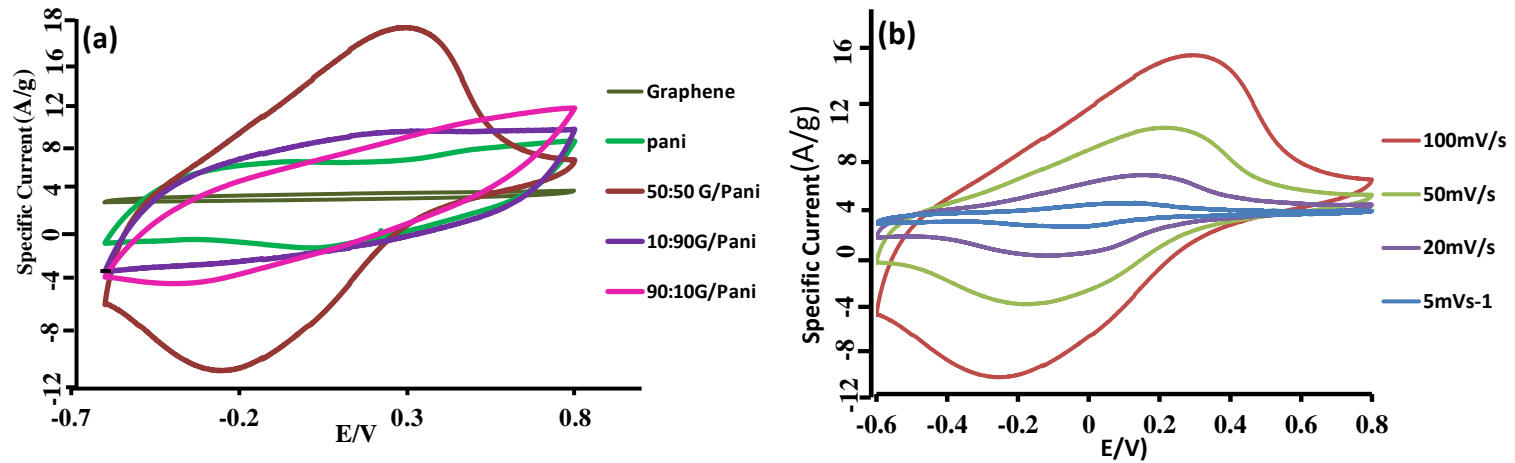


Figure 24. (a) CV profile of PANI, graphene, and G-PANI (10:50:90) nanocomposites at 5mV/s and (b) CV profile of G-PANI (50:50) nanocomposites at 5, 20, 50 and 100 mV/s.

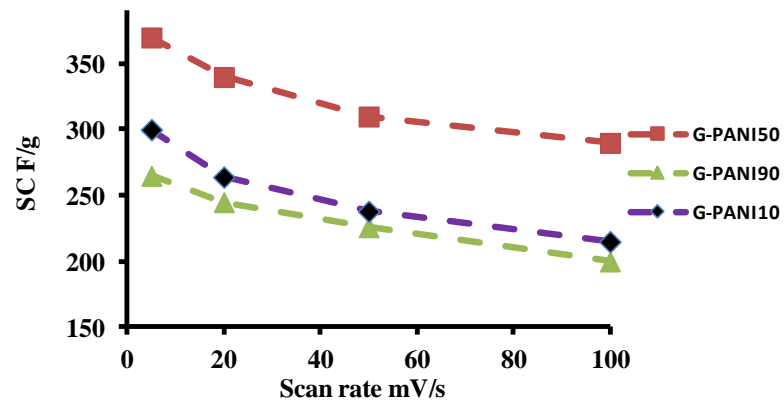


Figure 25. Specific capacitance versus scan rate (5, 20, 50,100) mV/s of G-PANI (10:50:90) nanocomposites.

Further Figure 26 shows the chronopotentiometry behavior of G-PANI films of different weight ratios. The charge-discharge curves of all prepared material have the potential range window from -0.5 to 2.0 V in 2MH₂SO₄ at a discharge current density of 0.2A/g. All charge-discharge curves for G-PANI films of different weight. ratios are triangular in shape [74]. In polyaniline discharging curve two prominent voltage stages are observed which is in the range of 1.6-0.5V and 0.5-0V respectively and simply describes the presence of EDL and faradic capacitance influence. Compared to PANI, the graphene discharge curve has quite a longer voltage range from 1.3V to -0.1V and then from -0.1V to -0.5V which demonstrates the dominant role of EDL capacitance in graphene film. In comparison to PANI and graphene, a charge-discharge curve of all G-PANI films has two voltage ranges from 1.9V to 0.75V and 0.75V to 0V.

However due to an existence of equivalent series resistance (ESR) in electrodes, all G-PANI films show the voltage drop. A comparative study of G-PANI films reveals that the voltage drop is much smaller in G-PANI50 film than in G-PANI10 and G-PANI90 films and has a longer discharge curve due to the existence of faradic capacitance and superior electrochemical characteristics. Slower potential change rate, $\Delta V/\Delta t$, of G-PANI50 films indicate higher specific capacitance. This result reveals that the internal resistance in G-PANI50 film is much lower than other G-PANI films electrode which is of great interest in fabricating higher specific capacitance supercapacitor. The specific capacitance values are calculated from charge-discharge curves using equation 15, where m_1 and m_2 are the sum of mass of two electrodes, Δt is discharging time, ΔV is maximum potential and I is a current density.

$$C = (I \cdot \Delta V) / (\Delta t \cdot (m_1 + m_2)) \quad (15)$$

Specific capacitance values from discharge curves of G-PANI (10, 50, and 90) films are found as 245F/g, 360F/g and 290F/g and are consistent with the CV results. Thus, from the capacitance evaluation discussion of G-PANI (10, 50, 90) films with the cyclic voltammetry and the charging-discharging method, it can be inferred that the addition of the optimum amount of graphene within the polyaniline chain is vital to improving the performance and efficiency of the device. Otherwise performance of a device can degrade due to the enhancement of internal resistance of the electrode material. In addition to charging discharging curves, the columbic efficiency was calculated for all three G-PANI compositions (10, 50, and 90) electrodes given in Figure 27. Columbic efficiency is calculated by using the ratio of discharge time to charge time.

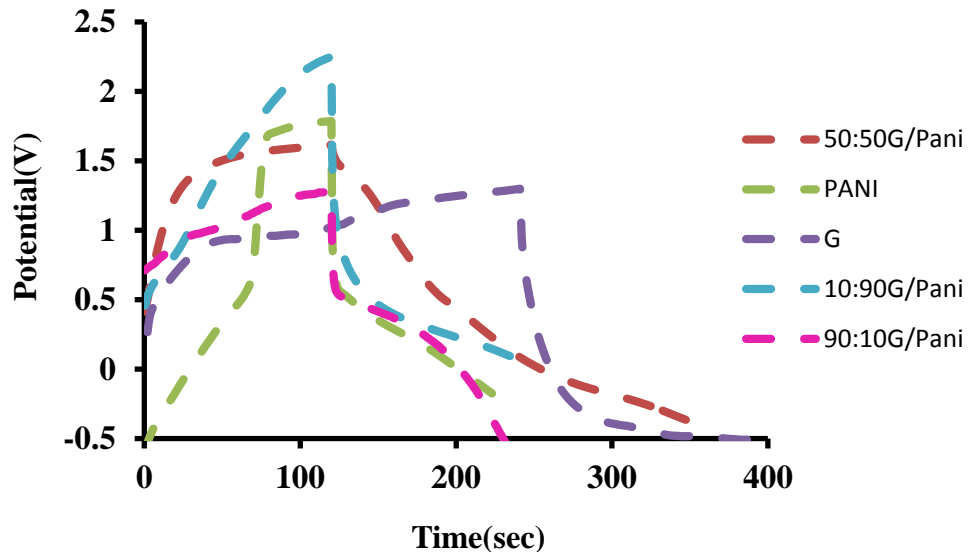


Figure 26. Charging discharging response of PANI, graphene and G-PANI (10:90,50:50, 90:10) nanocomposites.

It has been observed that initially the G-PANI films show lower efficiency due to the voltage drop but later tend to be constant over the number of cycles. Among all G-

PANI films the G-PANI50 shows higher columbic efficiency which is around 90% throughout 500 numbers of cycles. However, the initial decrease in capacitance was related to the irreversible charge compensation in faradic reaction associated with the oxidation/reduction of PANI.

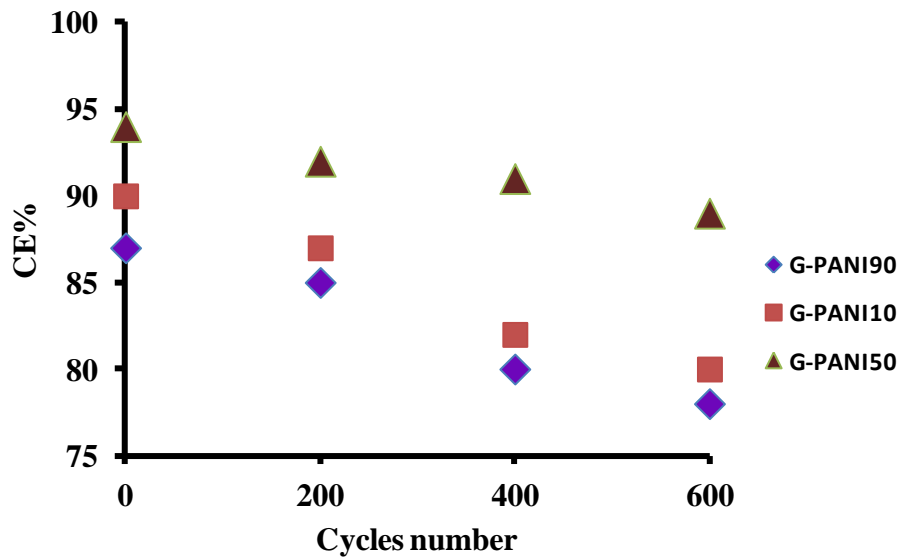


Figure 27. Columbic efficiency versus cycles number of G-PANI (10:90, 50:50, 90:10) nanocomposites.

The long term capacitance performance of G-PANI films can be evaluated while running the cell for 500 cycles is shown in Figure 28. While increasing the cyclic numbers, the specific capacitance of G-PANI (50:50) film decreases slightly but then levels off after the 300th cycle this is a good trend and evidence of higher electrochemical stability of the film. Such a low decrease in specific capacitance and high efficiency after the long charge/discharge cycles indicates the high stability of the G-PANI composite and its prospective potential as an active electrode material for long-term supercapacitor applications.

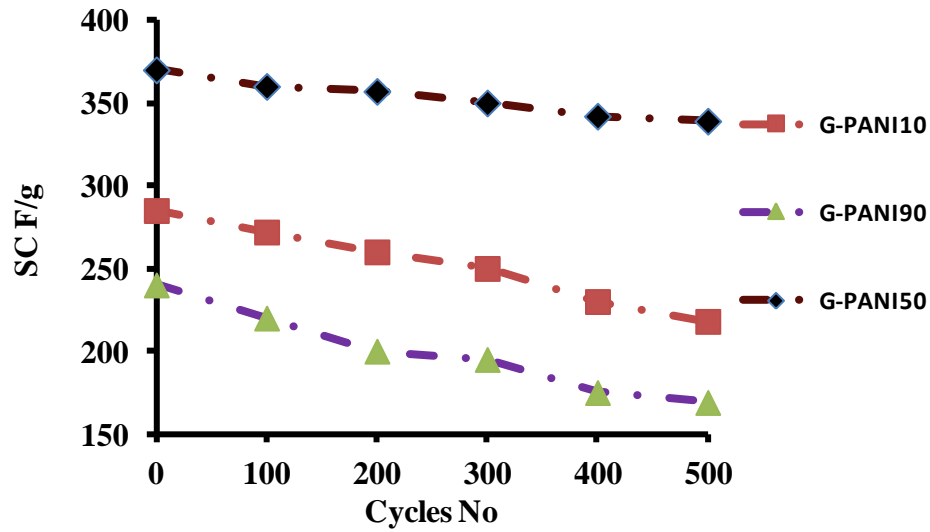


Figure 28. Specific capacitance versus cycle numbers of G-PANI (10:90,50:50,90:10) nanocomposites.

By comparison G-PANI50 and G-PANI90 show more improved stability upon cycling than G-PANI10, which attributes the superior mechanical property of graphene addition to polyaniline. This result illustrates that improved electrochemical property of the G-PANI electrode material to be used in the high performance supercapacitor.

3.4.2.2 Four Probe Measurement

The four probe point approach is quite significant in knowing the conductivity of material corresponding to its elemental composition especially in thin film material. Here we have used the four probe method to calculate the conductivity of different weight ratios of G-PANI films. Calculated conductivity values of G-PANI films are given in table 6. It is seen that as graphene adds to polyaniline, the resultant nanocomposites material is increasing the conductivity. We made the measurement for three samples with graphene content of 10, 50 and 90% to aniline monomer weight. percent during the synthesis of resultant material. It has been found that conductivity of films kept

increasing with the addition of graphene into polyaniline rather than with PANI alone. The maximum conductivity of the film was found at 7.65 s/cm for the G-PANI90 sample. However specific capacitance calculated for these samples show the linear relation up to some extent and corresponds to the conductivity of a material. The specific capacitance versus conductivity of G-PANI films is given in Figure 29.

In contrast to conductivity, the maximum specific capacitance was obtained for G-PANI50 film. This simply attributes that electronic conductivity of electrode material is essential to a certain limit. Beyond that limit the conductivity is not playing any prominent role in increasing the specific capacitance of the device. It may be because aside from the conductivity of electrode material there are other factors too, which has dominant influence in order to keep the overall resistance of material lower (e.g. minimum grain boundaries effect, appropriate surface area, pore size, and morphology of material to increase the specific capacitance of a device [76-77].) Thus the results in Figure 29 confirm that G-PANI film 50 has higher specific capacitance than G-PANI (10, 90) which is in agreement with the above discussion as explained in chapter 3.

Table 6. Conductivity of PANI, G-PANI (10:90, 50:50, 90:10) nanocomposites.

Material	Conductivity (s/cm)
PANI	3.63x 10 ⁻³
G-PANI 10:90	0.55
G-PANI 50:50	4.04
G-PANI90:10	7.65

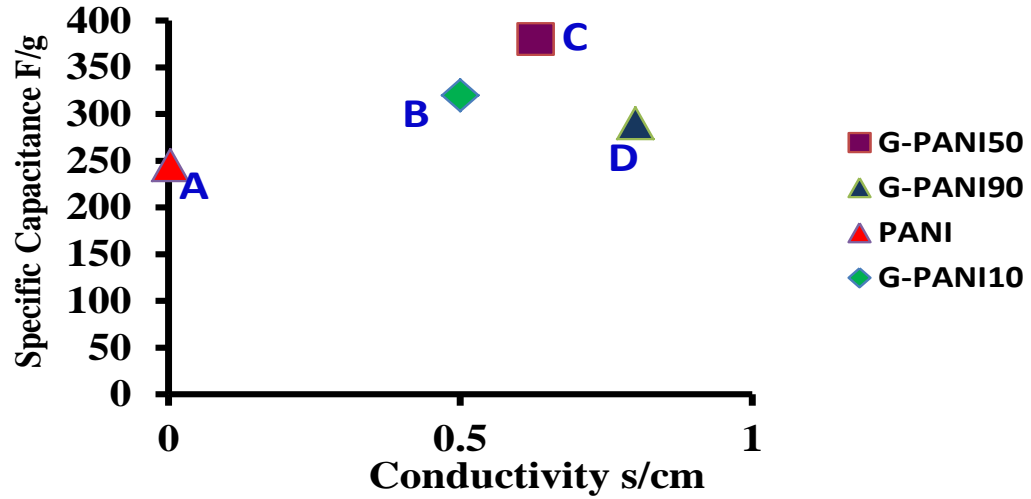


Figure 29. Conductivity versus specific capacitance for G-PANI (10, 50, 90) nanocomposites.

3.4.2.3 Ragone Plot

The Ragone Plot is an empirical relation between the specific power density and energy density to estimate the performance of energy storage devices. Figure 30 shows the Ragone Plot for three compositions of G-PANI films of identical area and thickness. Energy density is defined as the capacity of the amount of energy stored in a given space per unit volume. The Power density is defined as an amount of power or rate of energy transfer per unit volume [78]. Energy density for G-PANI films is calculated in W h kg^{-1} using equation 16, where m_{total} (m_1+m_2) is the total mass of two electrode materials and ΔV is the linear voltage change from 0 to V_{max} over time, and t_d is the discharging time.

$$Ed = \frac{\Delta V I t_d}{m_1 + m_2} \quad (16)$$

Similarly, power density (P_d in W kg^{-1}) for the G-PANI samples has been calculated using equation 17, where E_d is the energy density and t_d is the discharging time.

$$P_d = \frac{E_d}{t_d} \quad (17)$$

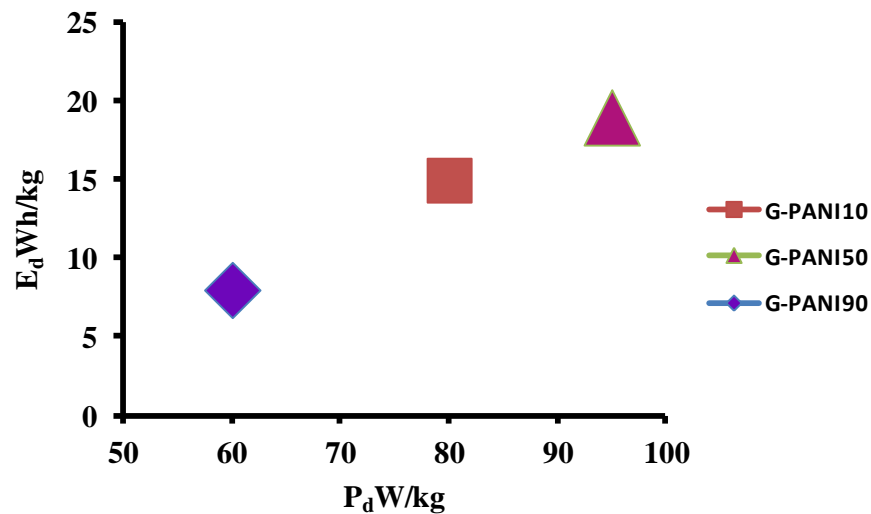


Figure 30. Ragone plot for G-PANI (10, 50, 90) nanocomposites.

By comparison, the maximum energy density and power density has been achieved for the G-PANI 50 electrode as illustrated in the Ragone Plot. It is noticed that G-PANI 50 films retain at least 80% of its energy density even when the power density increases from 40 to 100 Whkg^{-1} . Therefore, porous, flexible and the right proportion of graphene in PANI makes it an excellent choice of material to provide high power density with less loss of energy density in supercapacitors [79].

3.4.2.4 Electrochemical Impedance Spectroscopy (EIS)

Figure 31 shows the Impedance Plots of G-PANI nanostructures recorded at room temperature in a frequency range from 100 mHz to 100 kHz at the applied potential of 0V. The important electrochemical information can be extracted from the Impedance Plots by analyzing the limiting behavior at high and low frequencies. At the high-frequency region, a well-defined semicircle has been observed for Graphene, PANI, G-

PANI90 and G-PANI10 films, whereas no semicircle has been observed for G-PANI 50 films in high frequency region. Existence of a parallel combination of capacitance and resistance at the interface of the electrode and electrolyte is responsible for the formation of a semicircle in the high frequency region. However, the intercepts of graphene, PANI, G-PANI 10, G-PANI 50, G-PANI 90 films on the real impedance axis are at 75, 40, 25, 15 Ω . Among all G-PANI50 film shows resistance of less than 1ohm, which is mostly contributed by the uncompensated solution resistance. Smaller series resistance in G-PANI50 indicates that the charge transfer resistance is less, and our film has a faster kinetic property that reveals better ion and charge transport during doping/dedoping process of G-PANI50 film.

Further, the linear region formation in lower frequency is obvious in graphene, PANI, and G-PANI nanocomposites films which is defined as Warburg Impedance. The source of originating the Warburg Impedance is the slower diffusion rate across the electrode. PANI, Graphene and G-PANI 90 shows higher Warburg Impedance than G-PANI10 and G-PANI50 films as the slopes of the former films that are inclined closer to the angle of 45° . The difference in impedance at high and low frequency ascribes to the higher transport rate of reactants in high frequency region, whereas the transport rate of reactants is smaller in the low frequency region [79, 80]. For G-PANI50 films the vertical line leans more towards the imaginary axis, which reveals the good capacitive behavior of G-PANI50 than other G-PANI composition.

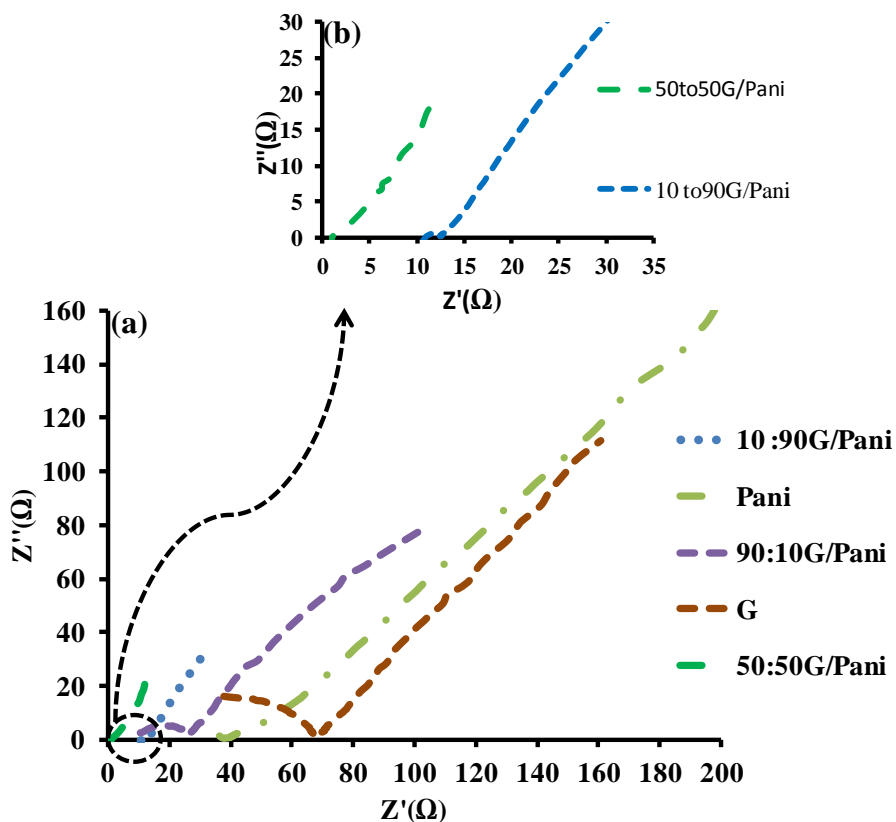


Figure 31. Impedance spectra for (a) graphene, PANI, and G-PANI (10:90, 50:50, 90:10) (b) G-PANI (50:50), G-PANI (10:90) nanocomposites.

In the end, by comparing the results of cyclic voltammogram, charge/discharge and impedance measurements, it can be seen that the specific capacitance of the G-PANI50 composite is markedly higher than G-PANI10 and G-PANI90 based electrodes for supercapacitor measurement. Therefore, surface modification by adding the equal weight ratio of graphene into aniline monomer is an effective way to improve the electrochemical performance and specific capacitance of the supercapacitor device. The higher flexibility of G-PANI50 provides the possibility of using the nanocomposites material without the addition of low capacitance conducting additives and insulating binder [57, 79].

3.5 Capacitance Evaluation with Different Thicknesses of G-PANI Film

As discussed above, the G-PANI50 film endowed higher specific capacitance, so here we synthesized the electrodes of the G-PANI50 material of different thicknesses. In order to determine the optimum film thickness to get the maximum specific capacitance, three thicknesses were selected 15 μm , 30 μm and 50 μm , respectively. Figure 32(a&b) compares the current voltage response of G-PANI50 film of different thicknesses on the same size of the electrode in 2MH₂SO₄. It is noticed that CV profile in Figure 32(a) for all three thicknesses shows the deformed rectangular shape of different areas. However, the area for the 30 μm film is closer to the ideal CV rectangular box. The maximum specific current and specific capacitance is obtained for 30 μm film and compared to 10 μm and 50 μm film thicknesses. It attributes that if a film is too thin, like 15 μm , it might provide less surface area, which not only decreases the electric double layer capacity, but also the specific capacitance of a device. In addition to thin film, if a film is too thick it may also offer high resistance to ion diffusion, despite large surface area. This simply attributes that if the surface area or pore size is smaller than the size of the electrolyte then it limits the ion diffusion, otherwise the inner surface area of electrode remains inaccessible by electrolytes ions due to an excessive thickness of film and develops higher interfacial resistance at electrode and electrolyte interface [81]. This degrades the specific capacitance of the supercapacitor.

In our experiments 30 μm film thickness reflects the maximum specific capacitance with the existence of useful surface area. Higher electronic and ionic conductivity also represents the higher electrochemical surface behavior of 30 μm film. Oxidation and reduction potential peaks for all thicknesses are observed at 0.2, 0.4, 0.57

and 0.6V. However the lower reduction peak at 0.57V has been observed in 30 μ m film than in 50 μ m and 10 μ m films, which clearly indicates the higher electronic conductivity of the film. The maximum specific capacitance obtained at 5mV/s for all thicknesses is given in Table 7.

Table 7. Specific capacitance versus G-PANI (50:50) thickness at a scan rate of 5mV/s.

Material	Specific Capacitance F/g
10 μ m	280
30 μ m	370
50 μ m	220

Figure 32(b) shows the change in specific capacitance of 30 μ m film thickness at different scan rates (100, 50, 10 mV/s). However specific capacitance comparison of all film thicknesses at scan rates of (5, 20, 50 and 100 mV/s) is given in Figure 32(c). It is seen that the capacitance decreases as scan rate increases due to the diffusion limitation of electrolyte ions in the inner surface area of the electrode material, however the rate of decrease in capacitance versus scan rate is lower in 30 μ m film than in 10 μ m and 50 μ m films, which clearly indicates the higher electroactive characteristic of film. The investigation of the charge/discharge study of G-PANI50 film of different thicknesses is shown in Figure 33. All discharge curves show the linear and symmetric behavior and voltage is in the range of 0-1.5V in 2MH₂SO₄ at a current density of 0.2A/g. The initial voltage drops are observed in all films, which is related with the ohmic loss arises from

the internal resistance of the cell. Nevertheless, the low series resistance has been observed in 30 μm film compared to 10 μm and 50 μm electrodes, which tells the higher ability of ion diffusion in active material.

Further the voltage change rate ($\Delta V/\Delta t$) in a 30 μm film is smaller than in 50 μm and 10 μm film thicknesses, this leads to higher specific capacitance in 30 μm film. Therefore, it can be inferred from the above discussion that optimum thickness plays an important role in lowering resistance to counter ion diffusion. Shorter diffusion distance of counter ions during complete charge/discharge yields higher specific capacitance. Moreover, specific capacitance was calculated using chronopotentiometry curves and is consistent with the SC values obtained by CV plots. The specific capacitance using charge-discharge curves at constant current density for 10 μm , 30 μm and 50 μm thicknesses are obtained as 280F/g, 360F/g and 220F/g. Figure 34 shows the comparison of columbic efficiency of 10 μm , 30 μm and 50 μm thicknesses. Initially efficiency drops a little due to the redox reaction of PANI, and later the rate of efficiency drops and gets slower, which ascribes the improve mechanical stability of G-PANI films. By comparison, the rate of decrease of the columbic efficiency over the number of cycles of the 30 μm films is significantly lower due to the higher electroactive characteristic than 10 μm and 50 μm films.

3.5.1 Electrochemical Impedance Spectroscopy (EIS)

The Electrochemical Impedance Spectroscopy (EIS) study for supercapacitor fabrication from the G-PANI50 of thicknesses 10 μm , 30 μm and 50 μm in 2M H_2SO_4 is qualitatively analyzed using Nyquist Plots shown in Figure 35. Figure 35 compares the

Impedance Plots for $2\text{MH}_2\text{SO}_4$ in three frequency regions. The small semicircle is observed at high frequency only for $50\mu\text{m}$ thickness which attributes to bulk electrolyte resistance. However, no semicircle is observed in the high frequency region for $30\mu\text{m}$ and $10\mu\text{m}$, films which demonstrates the faster kinetic rate in the $30\mu\text{m}$ film thickness. In the low frequency region, the cause of forming the non-vertical slope of the electrochemical capacitor is 1) morphology, porosity and redox properties of G-PANI. 2) The low mobility of ions which increases the charge transfer resistance [81, 82]. Moreover, the straight line portion in $30\mu\text{m}$ film leans more towards the imaginary axis and it indicates a good capacitive behavior. This illustrates the low charge transfer resistance with increasing double layer capacitance of $30\mu\text{m}$ film thickness. The bulk resistance for films of $10\mu\text{m}$, $30\mu\text{m}$ and $50\mu\text{m}$ thicknesses is found in 35, 16 and 5 Ω . The qualitative comparison of film conductivity and capacitance of the cells can be well examined due to the slope differences of the Nyquist Plots and maximum resistance values of the plots.

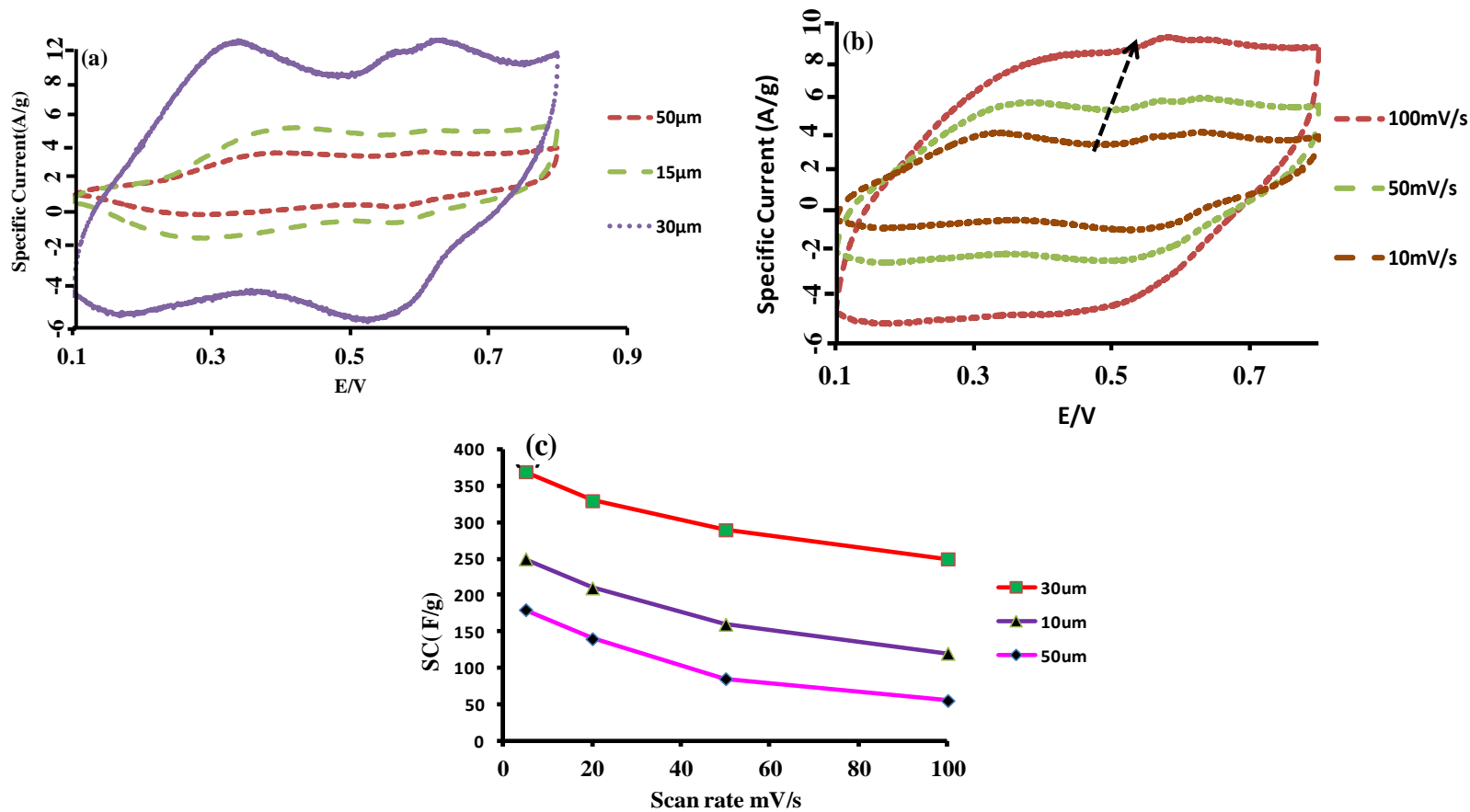


Figure 32. (a) CV comparison of G-PANI50 of film thickness 10µm, 30µm and 50µm at 5mV/s (b) CV profile of 30µm film thickness at the scan rate of 10, 50 and 100 mV/s (c) Specific capacitance versus scan rate of G-PANI film of thickness 10, 30 and 50µm.

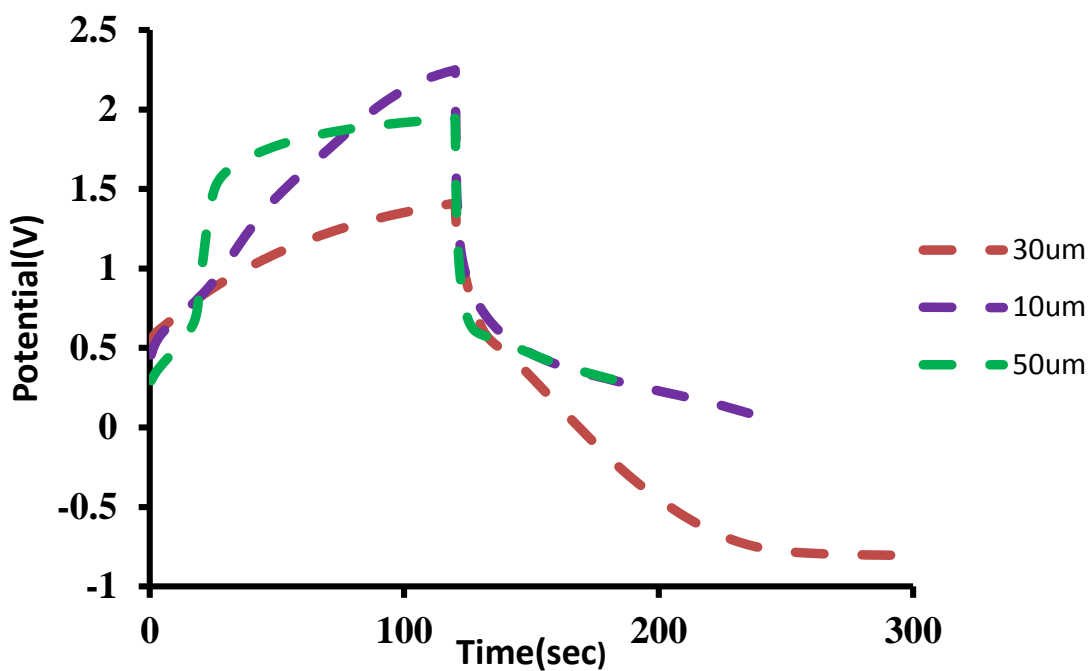


Figure 33. Charging-discharging curves for G-PANI50 of film thickness 10µm, 30µm and 50µm.

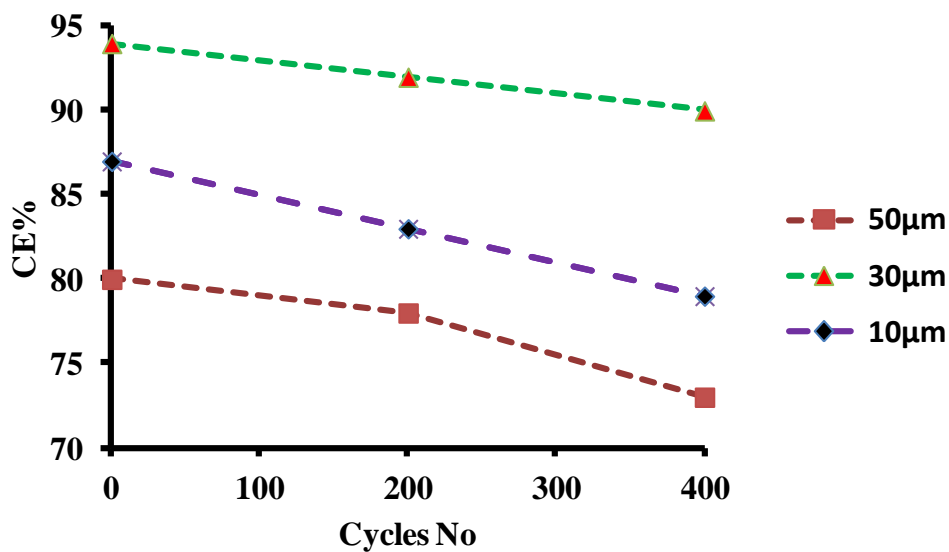


Figure 34. Columbic efficiency G-PANI50 film of thickness 10µm, 30µm and 50µm.

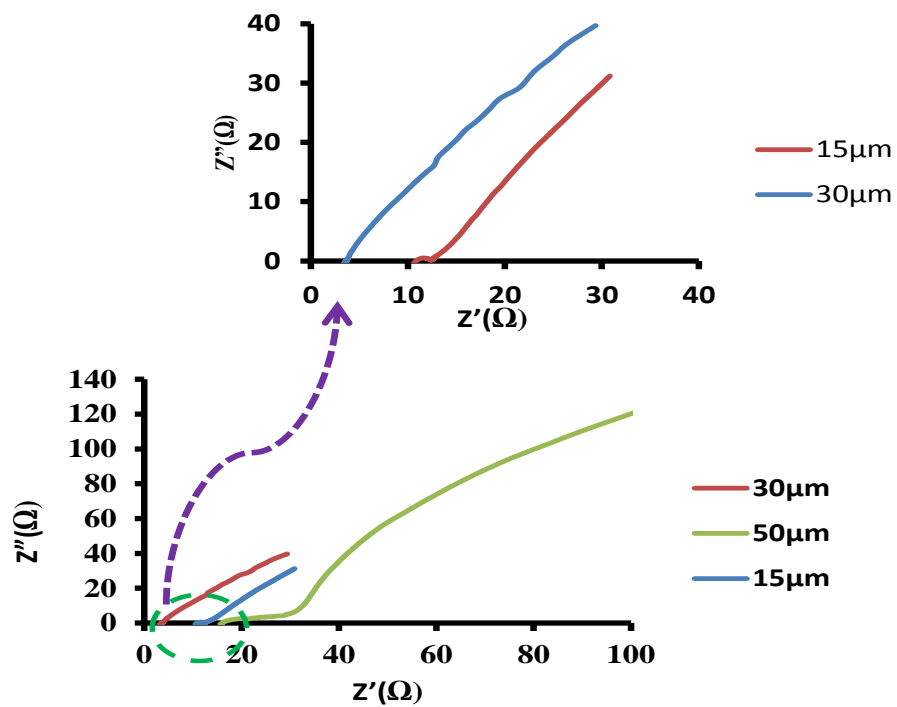


Figure 35. Impedance plots for G-PANI50 for film thickness of 10 μm, 30 μm and 50 μm.

3.6 Summary

G-PANI nanocomposites of different compositions are prepared by the facile chemical polymerization approach and further characterized for application to electrochemical capacitors. Tunability of a specific area and conductivity of the film has been investigated in depth. However, the incorporation of graphene can dramatically increase the charge storage capacity, and the specific capacitance of the G-PANI electrode. The maximum specific capacitance of 370F/g has been obtained for the equal weight ratio of graphene to aniline monomer. This is almost two to three times higher than the specific capacitance of graphene and PANI. In addition to higher specific capacitance, G-PANI nanocomposites also demonstrate the stable electrochemical properties and long cycle life. The energy density of the G-PANI based supercapacitor is apparently higher than PANI and graphene based supercapacitor. The optimum film thickness of the G-PANI film has also been studied to achieve the maximum specific capacitance of supercapacitor. For instance the film thickness of 30 μ m has provided the higher specific capacitance of 360F/g and columbic efficiency of 90% compared to 15 μ m and 50 μ m film thicknesses.

CHAPTER 4: INFLUENCES OF ELECTROLYTES AND SOLVENTS ON G-PANI BASED ELECTROCHEMICAL CAPACITOR

In addition to the influence of graphene content and film thickness variation in G-CPs nanocomposites as discussed in chapter 3rd for supercapacitor application, there are other important factors, too, that need to be investigated to enhance the performance of a device. Besides the electrode material and configuration, electrolyte is also one of the key parameters which affects the shape, formation and thickness of electric double layer EDL in electrochemical capacitor. The EDL thickness is generally equal to few nanometers which helps to store energy electrostatically in supercapacitor. Therefore the interfacial effect of electrode surface and size of electrolyte ions plays a dominant role in the capacity of EDL [83]. EDL formation mechanism depends on the applied voltages on the electrodes, which separates the ions into cations and anions in electrolytes and are then attracted to negative and positive electrodes to form the electrical double layer.

Accepting with the exception of G-PANI the porous electrodes, the capacitance of supercapacitor is thus determined by the packing of electrolytes. Therefore, making an appropriate choice in electrolytes is certainly a good way to enhance the specific capacitance as well as the energy density of the device. In general, most known electrolytes for the supercapacitor are molten salts, aqueous electrolytes, organic electrolytes and room temperature ionic liquids (ILs) [84]. Recently, molten salts, due to the limitation of high temperature, are rarely used in electrochemical capacitor. Typically,

aqueous electrolytes, due to its higher conductivity, low cost such as H_2SO_4 , HCl , KOH , Na_2SO_4 solutions are widely used in ECs. However, the main limitation for aqueous electrolytes is the low operating voltage which is at around (1.3 to 1.5) kinetically. This low operating voltage lowers the specific capacitance of a device as well as the aqueous electrolytes which have high evaporation rate and the high prospective of corrosion to the hardware part of device, this not only degrades the performance but also reduces the life of the device. To reduce the risk of corrosion and improve the stability of device, another promising class of electrolytes is an organic electrolyte. Organic electrolytes, in contrast to aqueous electrolytes, have a larger decomposition voltage (approx. 2.7V) which may be the reason to increase the energy density of ECs and are less likely to be corroded. The most recent electrolyte, which has attracted, significant attention in electrochemical devices is room temperature ionic liquid (ILs). Since ILs have wide electrochemical windows, excellent thermal stability, non-volatility, and good ionic conductivity, makes it a promising candidate for ECs. By comparison, the IL has higher decomposition voltage, which is at around 2.6 to 3.5V, than aqueous and organic electrolytes [85].

Besides the nature of electrolyte, EDL mechanism also depends on the concentration of electrolytes. This means the optimal number of ions in an electrolyte is also essential to obtain the maximum EDL capacity. Thus, in this chapter we are investigating the role of aqueous, organic and Ionic liquid (IL) electrolytes, the concentration of electrolyte and effect of solvents in G-CPs films for electrochemical capacitor application.

4.1 Capacitance Evaluation with Different Electrolytes for G-PANI Film

As discussed above in chapter 2nd and 3 the graphene-polyaniline nanocomposites (G-CPs) were synthesized using the facile chemical approach. The G-PANI50 nanocomposites rendered maximum capacitance, so all the electrodes are fabricated by drop casting the G-PANI50 film in NMP (N-methyl-2-pyrrolidone) on the graphite electrodes of 1cm² area. Typical thickness of the electrodes was kept at 30µm as it has shown optimum specific capacitance discussed in chapter 3. Figure 36(a,b,c) gives the detailed comparison of CV study of G-PANI50 films in aqueous, organic and ionic liquid electrolytes in the potential window of -0.6V to 1.0V. It is noted that CV curves of G-PANI50 exhibit deformed rectangular shape in aqueous, organic and ionic liquid electrolytes at the scan rates of 100, 50, 20 and 5mV/s. However, by comparison, the CV profile in 2M H₂SO₄ exhibits the reversible redox behavior with oxidation peaks at 0.3, 0.68, 0.92 V and reduction peaks at 0.7, 0.42, -0.05 V respectively. The peak around 0.65 V is the characteristics of the oxidation of emeraldine form of PANI, whereas the peak at 0.89 V is attributed to the pernigraniline state of PANI (otherwise known as protonation of PANI) [57, 98]. Larger CV area of G-PANI50 films in 2M H₂SO₄ gives the higher specific capacitance which simply shows the higher electroactive surface property in acidic solution.

Higher capacitance in acidic solution also attributes the good chemical affinity between electrode surface and electrolyte ions. In aqueous electrolytes, the ion size is smaller so it offers less interfacial and diffusion resistance across the EDL which shows the potential of higher capacity. Compared to an acidic solution we also performed the CV measurement in 2M KOH basic solution to understand the capacitance effect in

acidic as well as basic solution as shown in Figure 36(d). As it is reported in literature, that G-PANI nanofibers showed higher specific capacitance in basic solution, but in contrast to G-PANI fibers, the higher specific capacitance for G-PANI nanocomposite was not observed in basic medium [87]. The Shape of the CV in 2MKOH exhibits a small surface area which is due to the undoped state of KOH system. Significant redox characteristics have not been observed in the measured CV profile of the KOH electrolyte. Therefore, it indicates that the salt or acidic system for the G-PANI supercapacitor or rechargeable energy applications provide better performance with higher specific capacitance and good cyclic stability. The CV curves for organic electrolyte (0.5 M LiClO₄) and ionic liquid (2:1 BMIM-PF₆/ACN) electrolyte are shown in Figure 36(b, c). CV measurement for LiClO₄ does not show any redox characteristic inspite chemical affinity of electrode material and organic electrolyte shows more like EDL behavior.

Compared to aqueous, the organic electrolyte shows less specific capacitance. This might be due to the fact that organic ions are bigger in size than aqueous electrolytes and offers higher resistance to diffuse through the inner surface area of electrode material. In addition to organic and aqueous electrolytes, the CV response of room temperature IL is seen in Figure 36(c). The smaller CV area of IL may also be due to the lower ionic conductivity of IL compared to organic and aqueous electrolytes, which increases the pore resistance of the electrolyte. It is understood that besides the surface area functional groups and morphology of the electrode materials, chemical affinity between the electrode and electrolyte is also a critical parameter to obtain the better performance in supercapacitor. The conductivity of 1BMIM-PF₆ is usually around 1.9-2.3 ms/cm which

is smaller than H_2SO_4 and LiClO_4 [88]. The anion size of PF_6^- is much bigger which may cause the slower diffusion than ClO_4^- and Cl^- ions, and some of the surface area cannot be accessed by PF_6^- ions, although the electrochemical stability of PF_6^- is higher than ClO_4^- and Cl^- ions. However the EDL structure and capacitance is evaluated by size of cations, anions and the size of electrolyte solvent. IL is ionic in nature which relates with the viscosity of ionic liquid respectively. The specific capacitance comparison of G-PANI50 films for aqueous, organic and IL electrolytes are given in Table 8 at the scan rate of 5mV/s. It can be observed that maximum specific capacitance has been obtained for acidic solution rather organic and IL.

Table 8. Specific capacitance comparison of G-PANI (50:50) nanocomposites in aqueous, organic and IL at scan rate of 5mV/s.

Electrolytes	Specific capacitance F/g
Acidic aqueous ($\text{HCl};\text{H}_2\text{SO}_4$)	370
Basic aqueous (KOH)	110
Organic electrolyte (LiClO_4)	160
Ionic Liquid(IL,s)BMIM- PF_6	125

On the basis of the insights obtained from the discussion of CV measurements of aqueous, organic and IL electrolytes, it is believed that electrolytes are different in nature and possess typical chemical affinity with the electrode surface. Despite the advantages and disadvantages of electrolytes, acidic electrolyte for G-PANI50 is more promising for the higher conductivity and higher specific capacitance of supercapacitor, but still more investigation regarding the types of electrolyte is required.

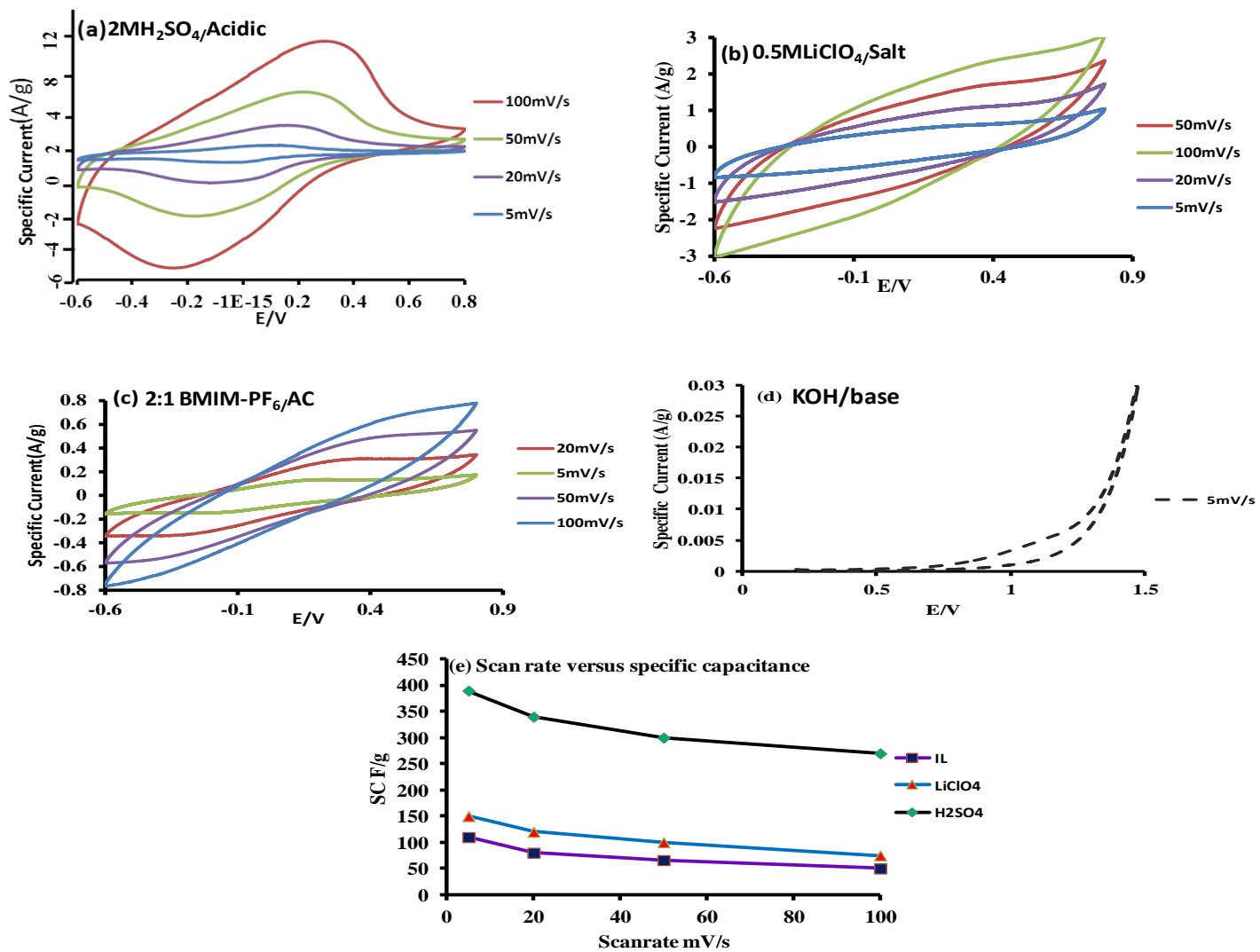


Figure 36. CV response of G-PANI50 film in (a) H₂SO₄ (b) LiClO₄ (c) IL (d) KOH (e) SC versus scan rate of G-PANI50 film in (a) H₂SO₄ (b) LiClO₄ (c) IL.

However, the specific capacitance versus scan rate of the G-PANI film in different electrolytes is demonstrated in Figure 36e. It is noted that in all electrolytes, specific capacitance decreases with the increase in scan rate from 5 to 100mV/s due to the diffusion limitations. However, the lesser rate of decrease in SC versus scan rate has been observed in H₂SO₄ due to the higher ionic and electronic conductivity besides the smaller ion size than in LiClO₄ and IL.

In addition to the CV response of G-CPs composites, the charging-discharging behavior of G-PANI50 film was also studied in different electrolytes at the constant current density of 0.2A/g. Figure 37 gives the comparison of the charging-discharging response in aqueous, organic and IL electrolytes. All charging curves are triangular in shape and vary in potential range from 0 to 3.5V. The detailed study of aqueous, organic and IL electrolytes manifests the low Ohmic drop in aqueous electrolyte compare to organic and IL. This simply attributes the higher conductivity or low internal resistance of aqueous electrolytes due to smaller ion size. The bigger ion size in organic and IL offers higher ESR resistance which causes the large Ohmic drop while charging and discharging of EC. The dominant effect of EDL capacitance in charging discharging behavior of organic and IL is more prominent than faradic capacitance respectively. However the combined influence of EDL and faradic capacitance is prominent in an aqueous electrolyte.

The longer discharge curve and slower potential change rate in aqueous electrolyte shows the superior electrochemical behavior of acidic solution over that of organic and IL. Thus, the lower internal resistance of aqueous electrolyte helps in the formation of larger EDL due to good chemical affinity between porous G-PANI50 and

cations and anions of acidic solution. Using the chronopotentiometry results, the calculated specific capacitance values for aqueous, organic and IL electrolytes are found at approximately 365 F/g, 135 F/g and 110 F/g. These values are in good agreement with the specific capacitance values obtained by cyclic voltammetry. So from the above discussion it is realized that the choice of appropriate electrolyte is very essential in the enhancement of the specific capacitance as well as the reliability of supercapacitor.

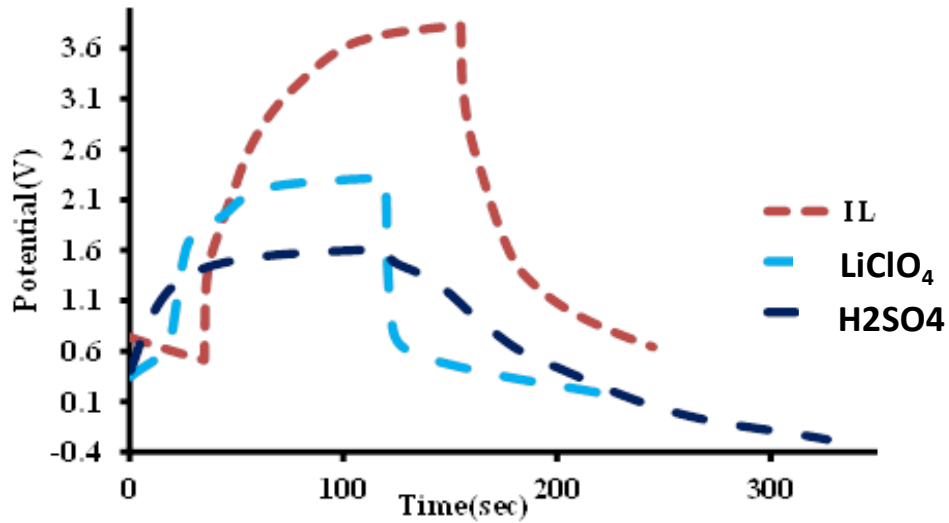


Figure 37. Charging-discharging curves for G-PANI50 in H_2SO_4 , $LiClO_4$ and IL.

The cyclic stability evaluation over the number of cycles for three electrolytes can be examined in Figure 38. It is noted that for the initial few cycles the aqueous and organic electrolytes shows less decrease in the specific capacitance than in IL. But as the number of cycles continued from 200 to 500, the capacity retention in the IL was higher than in aqueous and organic electrolytes which show the superior electrochemical

behavior of IL over that of acidic and organic solution. or it may also be due to the higher vapor pressure or viscosity of IL [89].

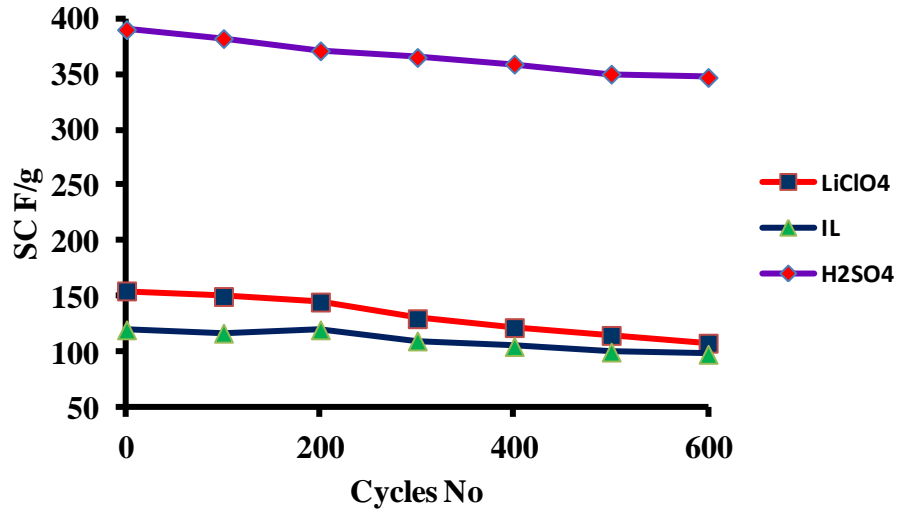


Figure 38. Comparison of specific capacitance versus cycles numbers of H₂SO₄, LiClO₄ and IL electrolytes.

On the basis of the charging-discharging data, columbic efficiency for all three electrolytes is calculated and given in Figure 39.

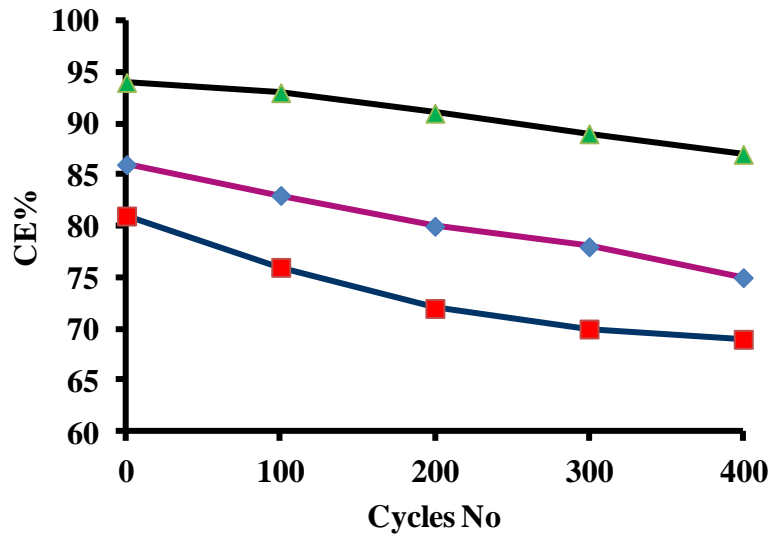


Figure 39. Columbic efficiency of acidic, organic and IL electrolytes.

In order to estimate the device stability and performance of G-PANI50 for all three electrolytes, the cell was run for 500 cycles. Figure 39 illustrates the stability behavior of aqueous, organic and IL electrolytes. It is obvious that over the number of cycles the acidic solution shows the lesser loss in columbic efficiency rather than organic and IL electrolytes. It may be due to the higher electrochemical and electroactive response of H_2SO_4 .

Nevertheless the supercapacitor performance of all three types of electrolytes can also be estimated by looking into the ragone plot as given in Figure 40. The maximum energy density with reasonably good power density has been obtained for acidic solution compare to organic and IL. However the maximum power density was calculated for IL then in organic and aqueous electrolyte.

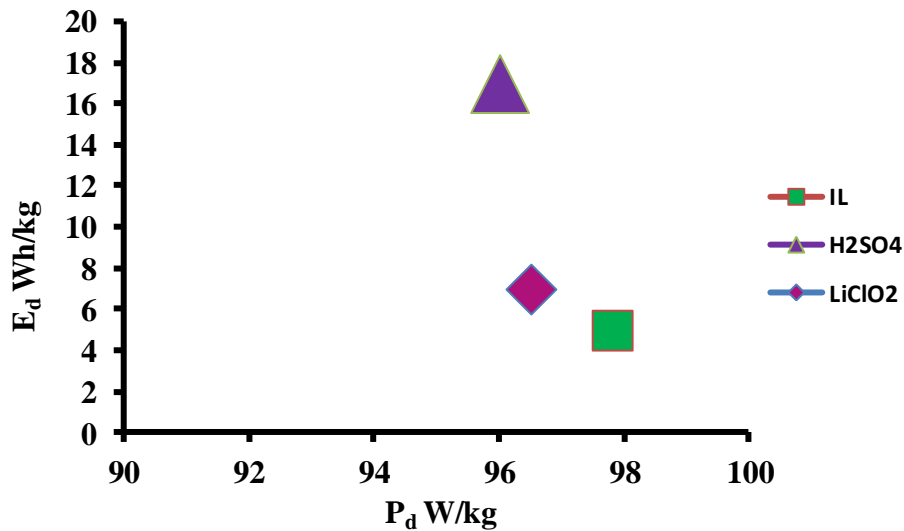


Figure 40. Ragone plot of acidic, organic and IL electrolytes.

It clearly explains the higher electrochemical stability of IL during charging and discharging with the higher potential at different current densities then in acidic and

organic electrolytes. Whereas the lowest energy density has been observed for IL then in organic and acidic solutions due to the higher charger transfer resistance that offers longer diffusion paths to IL ions [90, 91].

4.1.1 Electrochemical Impedance Spectroscopy (EIS)

Figure 41 reflects the impedance spectra analysis for aqueous, organic and IL electrolytes. All impedance plots were recorded at room temperature in the frequency range of 100mHz to 100KHz. Nyquist plots for aqueous, organic and IL show the charge transfer resistance of 0.1, 50 and 150ohms. The higher charge resistance ascribes to the diffusion/transport in IL due to bigger ionic size of IL and organic electrolyte than in acidic solution. It may be also due to higher conductivity of acidic solution, as well. All Nyquist plots have shown the identical slope in low frequency regions which indicates the Warburg resistance. The reason of the existence of Warburg resistance is due to the frequency dependent diffusion response of electrolyte ions. The larger Warburg resistance observed for organic and IL electrolyte indicates the obstruction in the ion movements due to the large variation in ionic diffusion paths [92, 93].

By comparison the H_2SO_4 has negligible Warburg resistance which manifests the presence of not only low electrical resistance but also exhibits small and equal diffusion paths of ions within electrolyte. However, in higher frequency a small semi-circle is not detected for H_2SO_4 which simply tells the influence of low charge transfer resistance. For instance, in H_2SO_4 G-PANI plot in low frequency shows the straight line angle incline more towards the 90° , which is closer to typical ideal EIS curve for supercapacitor. The low charge transfer resistance and following the trend for ideal

supercapacitor curve exhibited by G-PANI film in 2M H_2SO_4 confirms the superior electrochemical characteristics of acidic solution.

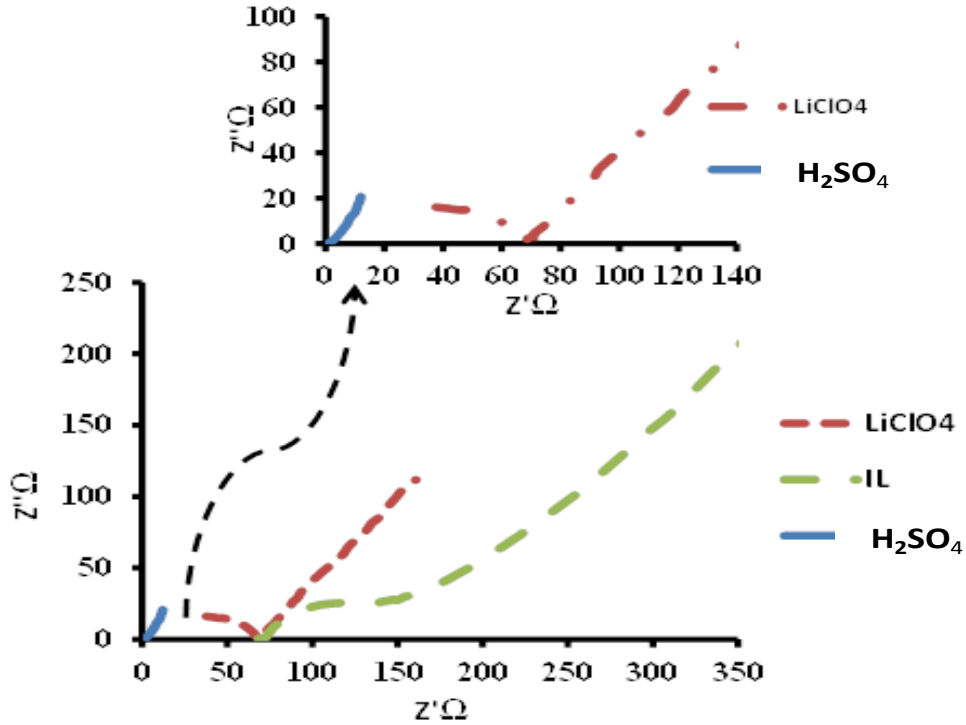


Figure 41. EIS analysis of acidic, organic and IL electrolytes

4.2 Influence of Electrolyte Concentration on G-CPs Film

Figure 42 illustrates the influence of electrolyte concentration for the capacitive behavior of G-CPs film. As discussed in section 4.1 among all the acidic electrolytes showed higher specific capacitance than in organic and IL. Therefore, we shall further investigate the role of acidic concentration on the capacitive performance of G-PANI films. Three H_2SO_4 concentrations are used to get the comprehensive idea to correlate the concentration with capacitive behavior of electrodes. Figure 41(a) shows the CV comparison of 0.1M, 2M and 4M H_2SO_4 concentrations at the scan rate of 5mV/s in a potential window of -0.6V to 1.0V. It is noted that CV measurements of 2M H_2SO_4 has

shown the ideal box shape larger surface area compared to 0.1M and 4MH₂SO₄. This might attribute to the higher conductivity of electrolyte and less electrode pore resistance.

Whereas the redox peaks potential is observed at -0.1, 0.3, 0.5 and 0.67V for 0.1M and 2M H₂SO₄ at scan rates of 100, 50, 20 and 5mV/s as shown in Figure 42(b, c). It is believed that the presence of these peaks mainly relate with the transition of PANI between its semiconducting state (leucoemeraldine form) to conducting state (polaronic form) in G-PANI film [52]. The peak centered at 0.5V is probably because of some semi redox mechanism due to the synergy effect of graphene and polyaniline components. However Figure 42(d) shows the CV profile of 4MH₂SO₄ having more EDL behavior and no significant redox peak was observed. Thus the reason for smaller CV surface area for 0.1M and 4M concentration can be due to lower conductivity, and ionic diffusion limitation in pores of electrode material. Aside from the decrease in specific capacitance for 4MH₂SO₄, the higher acidic solution concentration might risk the corrosion of device components and also affect the reliability and safety of the supercapacitor. Thus from the above discussion, it can be inferred that optimum amount of ions in electrolytes plays a significant role in the improvement of the performance of the supercapacitor. Table 9 provides the specific capacitance comparison at 5mV/s for 0.1M, 2M and 4MH₂SO₄. The maximum capacitance was obtained for 2MH₂SO₄ due to higher conductivity and lesser diffusion limitations. The change in specific capacitance versus scan rates for all three concentrations is shown in Figure 42(e). It is believed that lower capacitance at a higher scan rate may be due to the inaccessibility of electrolyte ions to the inner surface area of the electrode.

Table 9. Specific capacitance comparison of G-PANI (50:50) nanocomposites in (H₂SO₄) concentrations (0.1M, 2M and 4M) at 5mV/s.

Electrolyte Concentration	Specific Capacitance F/g
0.1MH ₂ SO ₄	180
2M MH ₂ SO ₄	360
4M MH ₂ SO ₄	250

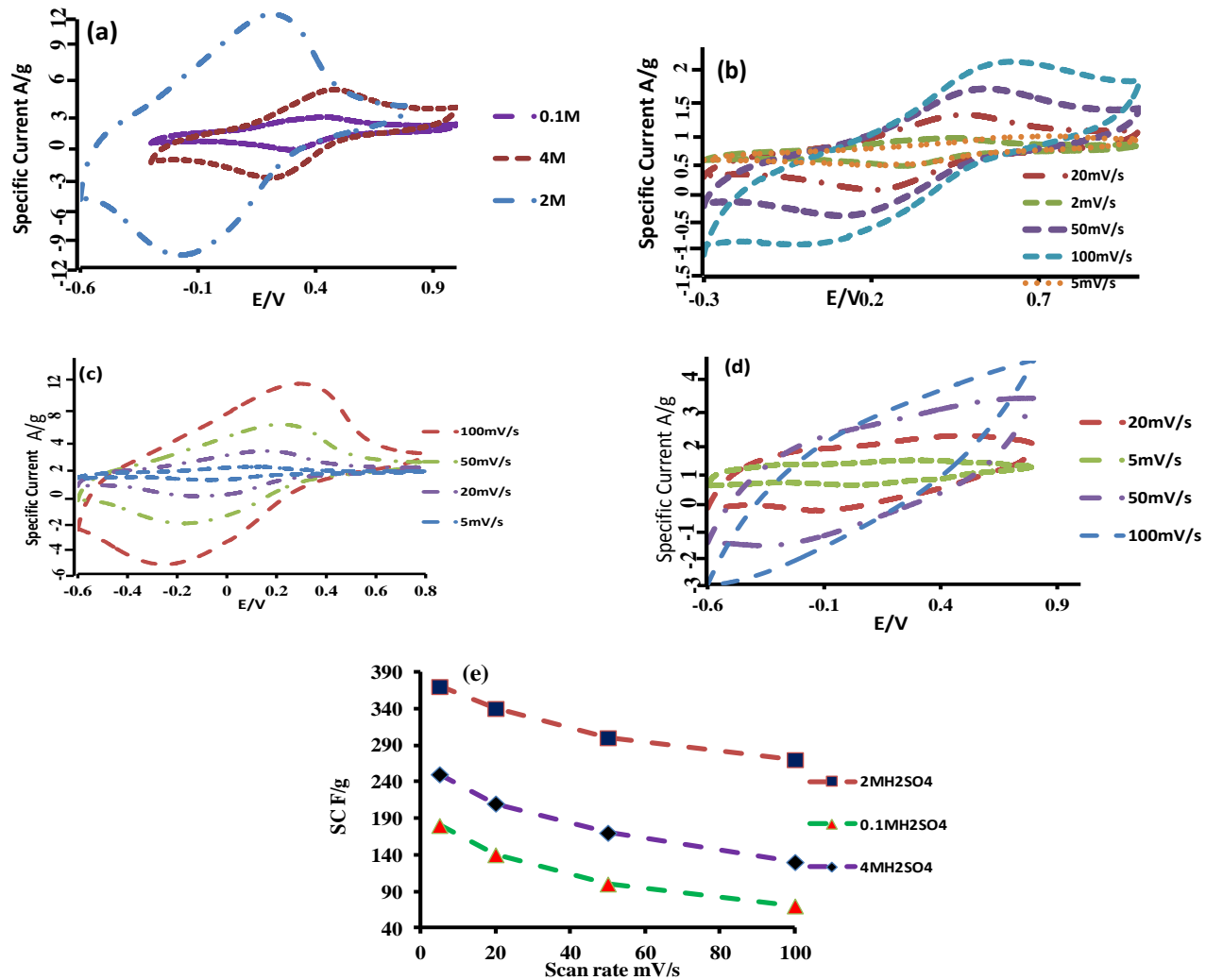


Figure 42. CV comparison of G-PANI film in 0.1M, 2M and 4MH₂SO₄; Specific capacitance versus scan rate in 0.1M, 2M and 4MH₂SO₄.

In order to evaluate the capacitive behavior, Figure 43 shows the charging and discharging trend for 0.1M, 2M and 4MH₂SO₄ at the constant current density of 0.1A/g. The potential range for all charging curves is between 0V to 1.6V. No significant difference has been seen in the discharging curves for different H₂SO₄ concentrations. However for 2MH₂SO₄ the discharging rate was found to be slower and contained small IR drops compared to 0.1M and 4MH₂SO₄. In discharging trends of 0.1M, 2M and 4M H₂SO₄ two voltage ranges are observed as ranging from 1.5 to 0.9V and 0.9 to 0.3V, 1.5 to 1.3V and 1.3 to 0V and 1.3 to 0.4 V and 0.4 to -0.6 V. The presence of two voltages ranges in discharging curves of 0.1M, 2M and 4MH₂SO₄ manifests the influence of EDLC and pseudocapacitance in relevant electrodes. Nevertheless, the 2M concentration has a larger pseudocapacitance influence than 0.1M and 4M, which may improve the specific capacitance in the supercapacitor. Specific capacitance values were calculated using charging-discharging curves for 0.1M, 2M and 4M are as 150, 360 and 270 F/g, which is in good agreement with the capacitance values obtained from CV curves.

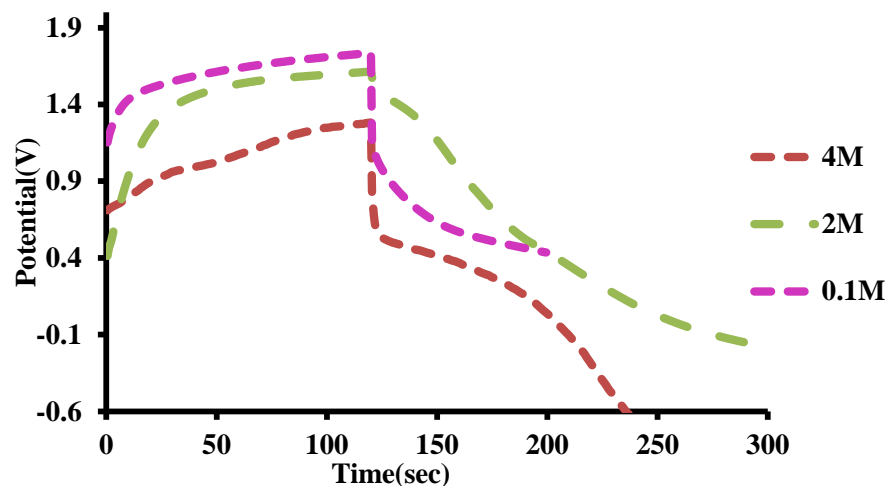


Figure 43. Charging-discharging profile of G-PANI in 0.1M, 2M and 4M H₂SO₄.

In addition to charging-discharging behavior, the cycle stability of 0.1M, 2M and 4MH₂SO₄ was also tested and capacity retention upon 500 cycles was found at around 87% in 2MH₂SO₄ then in 0.1M and 4MH₂SO₄. The capacity retention comparison of 0.1M, 2M and 4M H₂SO₄ is quite attractive in fabricating the durable and fast ECs.

4.3 Capacitance Evaluation of G-PANI Film with Different Solvents

As discussed in section 2.5 the electrode fabrication of G-PANI nanocomposites uses NMP solvent. Here we are discussing three solvents as NMP, Nafion and DMF in the formation of G-PANI film. In order to maintain the consistency in films, the mixing of G-PANI powder to the amount of each solvent was kept the same, which is 50mg

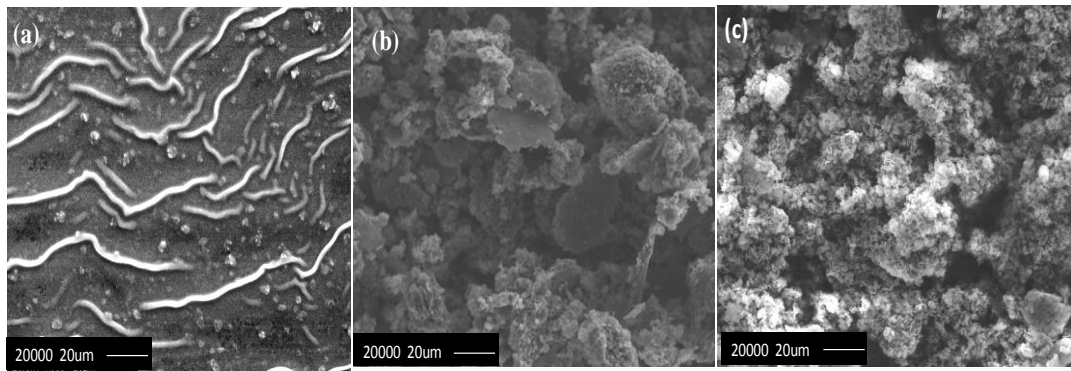


Figure 44. SEM results of G-PANI in (a) NMP (b) Nafion and (c) DMF.

composite material mixed in 30ml of solvent. For Nafion, however, the mixing solution contains the weight. ratio of Nafion, ethanol and water as (80:10:10). The film thickness for each solvent was kept relatively the same at 35 μ m on the size of 1cm² electrode. Figure 44(a, b, c) shows the SEM image of G-PANI films in NMP, Nafion and DMF solvents. A typical flake like structure of the G-PANI film cannot be observed in SEM image of NMP, because the NMP as a solvent possesses the very characteristic of the plasticizer to fabricate smooth film [52, 93, 94].

However, in contrast to NMP, SEM images for Nafion and DMF show the porous and flake like morphology of G-PANI film which is also promising in achieving reasonably good specific capacitance. For instance, besides flake like morphology, it has also several grain boundaries due to less solubility of G-PANI in Nafion and DMF. As it is noted that SEM image of G-PANI film fabricated with NMP shows smoother morphology and lined structure than in Nafion and DMF. The reason of obtaining the lesser lined penetrating, interesting structure in NMP reflects the doping in the G-PANI film which creates polaron and bipolaron states and change the morphology of polyaniline. It can also be due to high solubility of G-PANI in NMP. In addition to the SEM discussion, Figure 45(a, b, c) illustrates the CV measurements of NMP, Nafion and DMF casted films in $2\text{MH}_2\text{SO}_4$. Figure 45 depicts the deformed rectangular CV profile of NMP. Nafion and DMF synthesized films have reasonable specific capacitance, but the maximum specific capacitance was obtained for NMP films. It attributes the higher solubility of PANI in NMP than in Nafion and DMF. Influence of solvents on the capacitive behavior of G-PANI film is observed in Figure 45(a, b, c) at the scan rates of 5, 20, 50 and 100mV/s. High solubility of PANI in NMP gives less grain boundary and pore resistance which, in turn, provides high specific capacitance. As far as Nafion is concerned, it has less solubility for G-PANI material, but it acts as a conducting binder for the film and, thus, gives reasonably good capacitance.

In comparison to NMP and Nafion, the CV response of DMF shows the good capacitance, but it is still lower than the former solvents. This might be due to the partial solubility of G-PANI in DMF and causes higher resistance due to the diffusion limitations of ions into electrode surface. Redox peaks are observed at -0.1, 0.3, 0.5 and

0.67V for NMP, Nafion and DMF as shown in Figure 45(a, b, c). The maximum capacitance was obtained for NMP due to the higher conductivity and lesser diffusion limitations. The change in specific capacitance versus scan rates for all three solvents is shown in Figure 46. It is observed that specific capacitance of all films decreases with increase in scan rate due to the access of limited surface area or electrode pores resistance. However, the rate of decrease in specific capacitance for NMP film is lower than that of Nafion and DMF. This indicates the higher electroactive behavior of NMP film with good stability, higher conductivity and larger surface area. Maximum specific capacitance was calculated using CV response of NMP, Nafion and DMF at the scan rate of 5mV/s is 370F/g, 320F/g, and 260F/g.

In addition to the CV discussion, the capacitance performance of three solvents was also analyzed using charge-discharge behavior of films. Figure 47 shows the charge-discharge curves of films made of NMP films, Nafion and DMF at the current density of 0.2A/g. Potential range for all films varies within range of -0.5 to 1.6V and the shape of all discharge curves is almost identical in triangular shape. By comparison the low ohmic voltage drop is seen in NMP films then was observed in Nafion and DMF electrodes. However, the influence of EDL capacitance and pseudocapacitance is evident in discharging curves for NMP, Nafion and DMF electrodes. The slower change in voltage rate and large pseudocapacitance influence for NMP film shows the performance of NMP electrodes is higher than in Nafion and DMF electrodes.

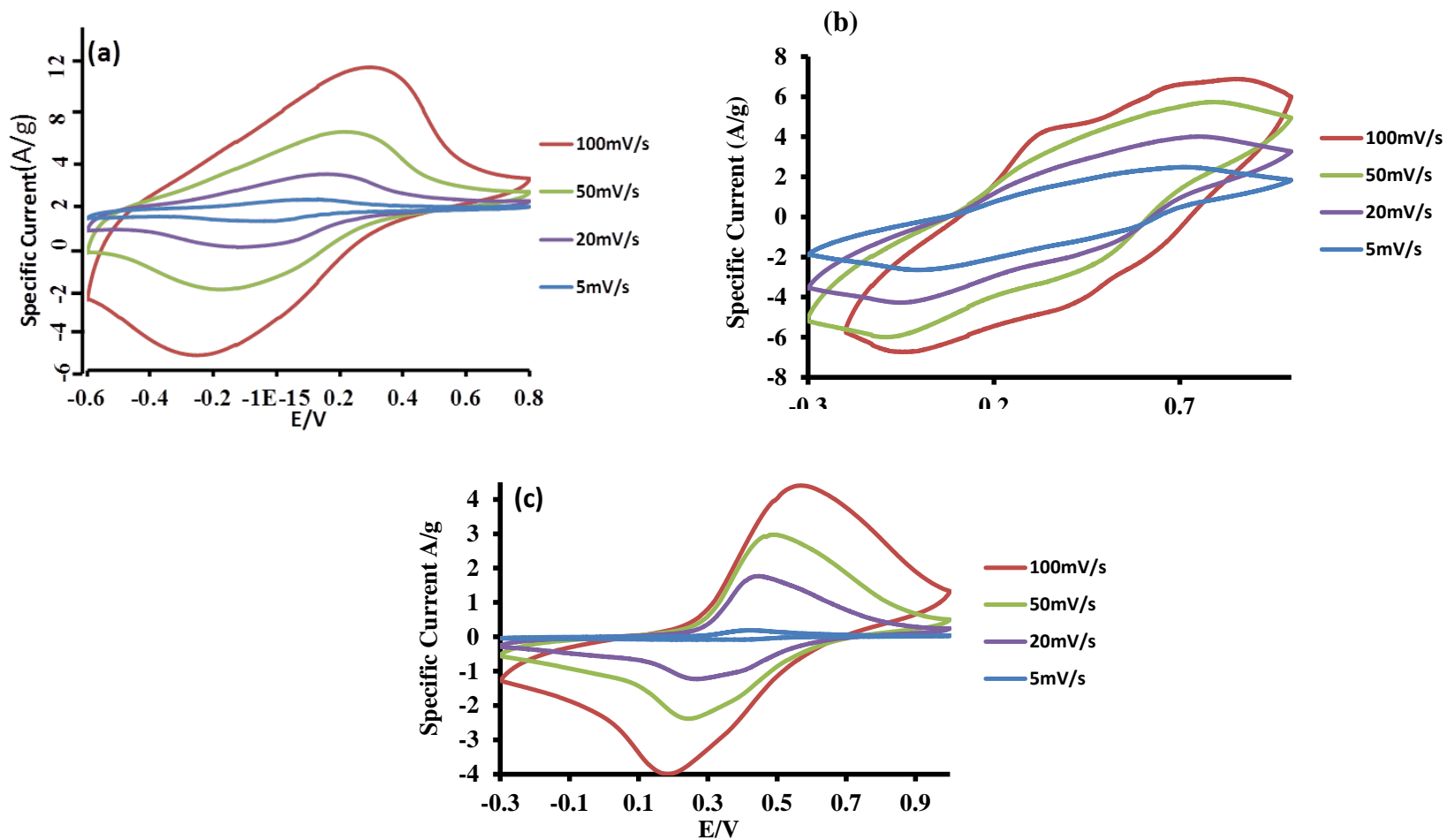


Figure 45. CV response of G-PANI in (a) NMP (b) Nafion and (c) DMF.

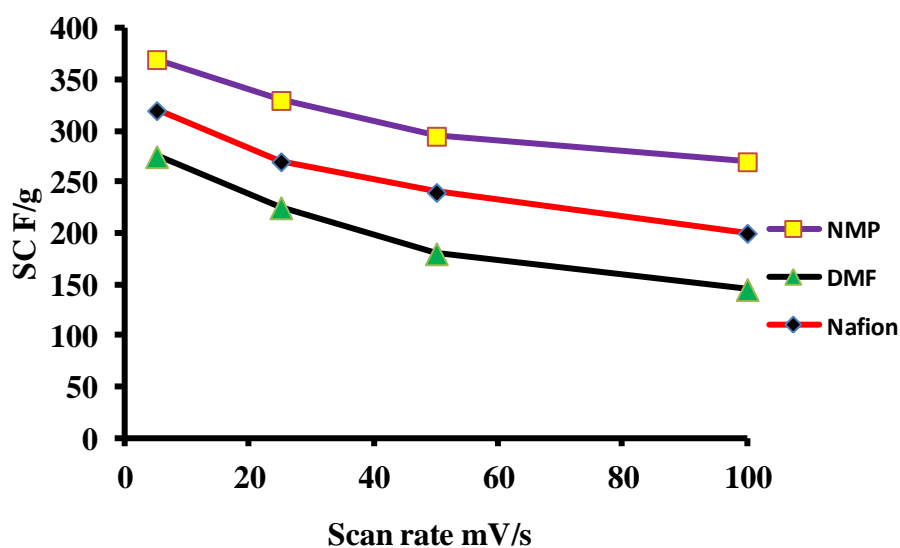


Figure 46. Specific capacitance versus scan rate of G-PANI in NMP, nafion and DMF.

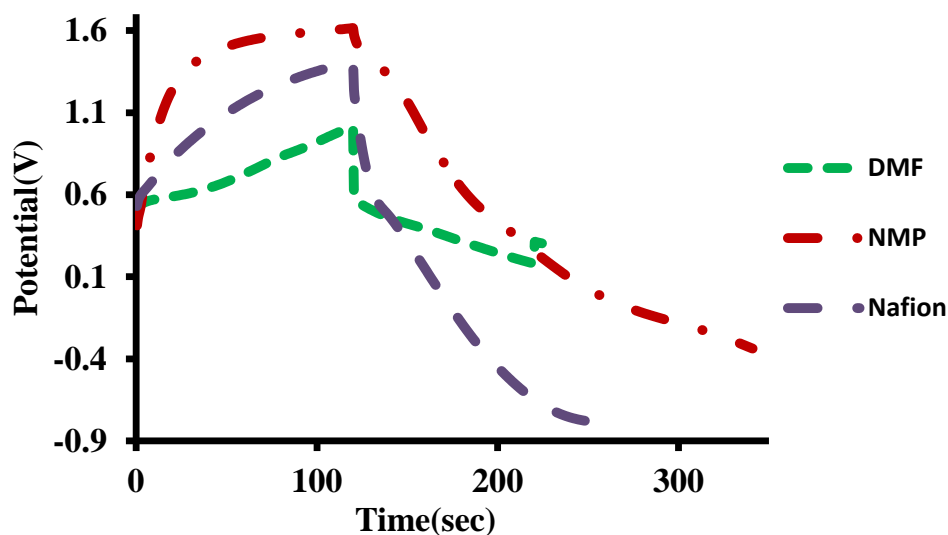


Figure 47. Charging-discharging comparison of G-PANI films in NMP, nafion and DMF.

It clearly supports the CV results that the higher electrochemical property of NMP films yields higher specific capacitance than other solvents. The specific capacitance calculated using discharge curves is given in Figure 48 which depicts the good stability of

films upon cycling for 500 cycles. Specific capacitance values calculated using chronopotentiometry matches, to an extent, to the capacitance values obtained by CV response.

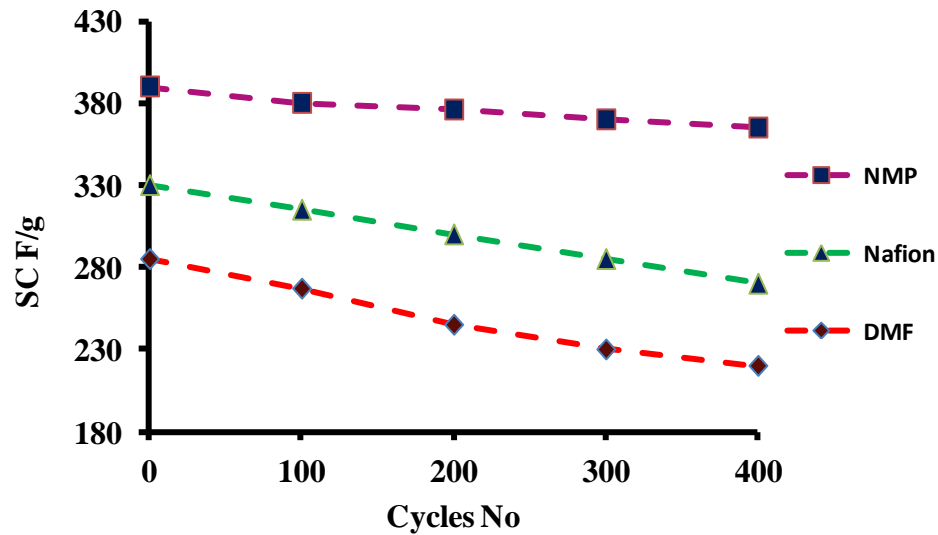


Figure 48. Cycle's stability versus specific capacitance of NMP, nafion and DMF.

Energy density and power density comparison of all three solvents also reveals the higher energy storage performance of supercapacitor with NMP films than with Nafion and DMF. The comparison study of energy density and power density of NMP, Nafion and DMF films are shown in Figure 49. It is examined that NMP films have higher energy and power density. Only 20 percent loss of energy density was observed over 500 cycles, which shows the potential of stable device using NMP as a solvent.

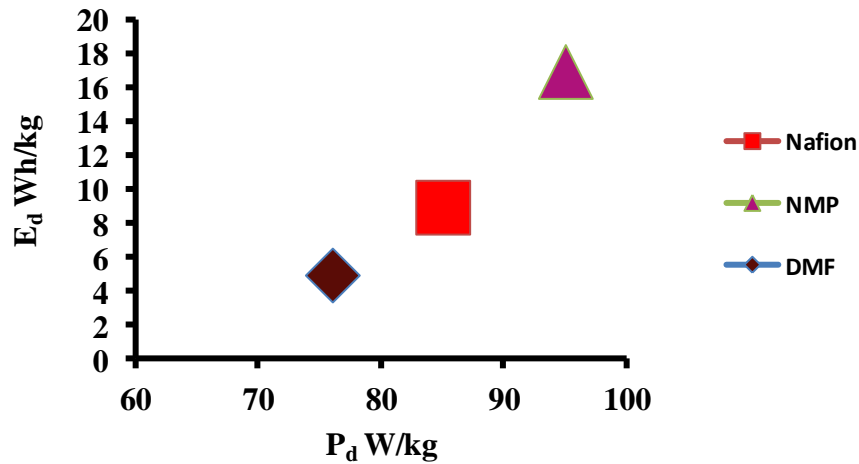


Figure 49. Ragone plot of NMP, nafion and DMF.

By looking at the impedance plot shown in Figure 50 it can infer that all films synthesized of NMP, Nafion and DMF solvents have electroactive surfaces, since they have typical charge transfer response from high to low frequency range in $2\text{MH}_2\text{SO}_4$ respectively. Observed equivalent series resistance (ESR) in impedance plots for NMP, Nafion and DMF films is found at 2, 5 and 15Ω . Lower values of ESR represent the higher charge transfer kinetics in NMP and Nafion based films than in DMF film. In the high frequency region, a small semicircle was observed only for DMF film, which was not seen for NMP and Nafion electrodes. The missing of small circle in NMP and Nafion films reveals the improved charge transfer rate and good chemical affinity between electrode and electrolyte. Besides the small charge transfer resistance NMP, and Nafion films also shows low Warburg impedance since the slopes of these films in small frequency region is more toward the imaginary impedance axis. It simply attributes the

adoption of equal and short diffusion paths by electrolyte ions which are desired to obtain high specific capacitance in supercapacitor [93, 95].

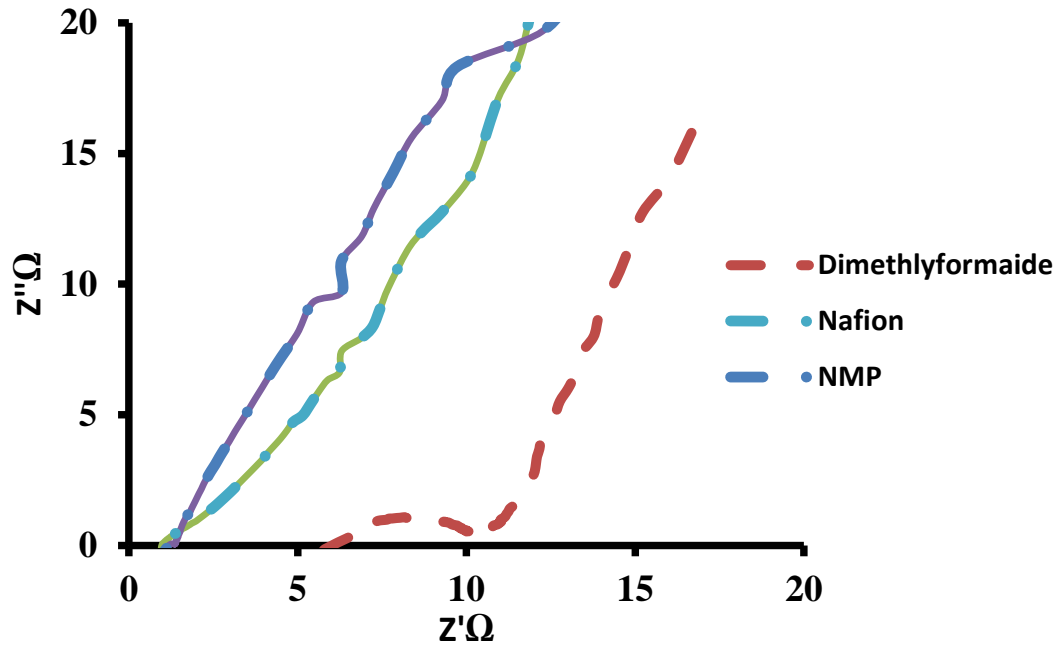


Figure 50. EIS analysis of G-PANI film in NMP, nafion and DMF.

4.4 Summary

In chapter 4 the effect of electrolytes, role of solvents in the fabrication of G-PANI films was also explored. Since different solvents have different packing orientation and solubility characteristics for polyaniline, so it is significant to analyze their solubility and impact on specific capacitance of electrochemical capacitor. Qualitatively the role of electrolytes, concentrations and solvents has been estimated by looking at the electrochemical measurement results including CV, EIS and chronopotentiometry. Further, the effect of electrolytes and role of solvents has also been studied rendering that acidic solution has higher specific capacitance than organic and room temperature ionic liquid (IL). Based on the satisfactory results of acidic solution, the optimum concentration of acidic solution has also been discussed to improve the performance and reliability of device.

CHAPTER 5: HETEROCYCLIC BASED CONDUCTING POLYMER NANOCOMPOSITE FOR ELECTROCHEMICAL CAPACITOR

Supercapacitor technology has been developed to close the gap between conventional capacitors and batteries because of their high energy density and power density. Conducting polymers and metal oxides are realized as the promising choice of materials in the development of efficient redox capacitor. In addition to aromatic based polymers (e.g., polyaniline, o- anisidine, o-toluidine) heterocyclic polymers have also gained significant attention for the application of green energy storage devices. Among them electroactive, polythiophene (PTh) and its derivatives are potentially focused by the researchers due to its ease of synthesis, chemical stability, light weight, corrosion inhibition , environmental stability and good conductivity properties.

Since the PTh is stable in both its doped and undoped states, the good stability of PTh in its oxidized state, high conductivity and amazing electrochemical behavior makes this material an excellent electrode choice for the commercial application of an electrochemical capacitor [96, 97].

In order to utilize the full advantage of polythiophene (PTh) for an electrochemical capacitor application, a composite of conducting polymers is recently in wide use by researchers. Among the metal oxides and carbon materials, currently the graphene is believed to be one of the best materials for composite choice due to high flexibility, large surface area, and excellent thermal and electronic conductivity.

Therefore, in this chapter, we are discussing the synthesis, characterization and electrochemical behavior of graphene-polythiophene (G-PTh) nanocomposite using facile chemical approach.

5.1 Experimental

5.1.1 Synthesis of G-PTh Nanocomposite Material

Here the chemical synthesis of G-PTh nanocomposite is reported by oxidative polymerization of thiophene using ammonium peroxydisulfate $[(\text{NH}_4)_2\text{S}_2\text{O}_8]$ and FeCl_3 under controlled conditions. Initially, the thiophene monomer was dissolved in methanol and water due to the rigid back bone structure of polythiophene (30:70) Percent. The polystyrene sulfonate Na salt (PSS) dissolved in HCl solution was set at 1Ph for two hours. Next, the thiophene monomer in methanol and water (30:70) percent was added to the PSS solution for two hours. The graphene nanoparticles purchased from angstrom materials (USA) were used without any further purification. The thiophene to graphene weight. ratio was kept at 1:1 and added to the PSS solution. Further the PSS Solution was cooled down to -4°C in an ice bath before the drop wise addition of 0.05M ammonium peroxydisulfate and 0.05M FeCl_3 oxidants [98- 99].

Polymerization was observed within 5 minutes of adding the oxidants when the solution starts changing its color from black brown to dark brown. The final reaction was continued for 24 hours under constant stirring. Finally, G-PTh nanocomposite recovered from the reaction vessel was filtered and washed thoroughly using deionized water, methanol (for the elimination of the low molecular weight polymer) and oligomers.

Further, the final precipitate was dried in a temperature-controlled oven at 100°C for 4 hours. Figure 51 shows the possible structure of the synthesized G-PTh polymer.

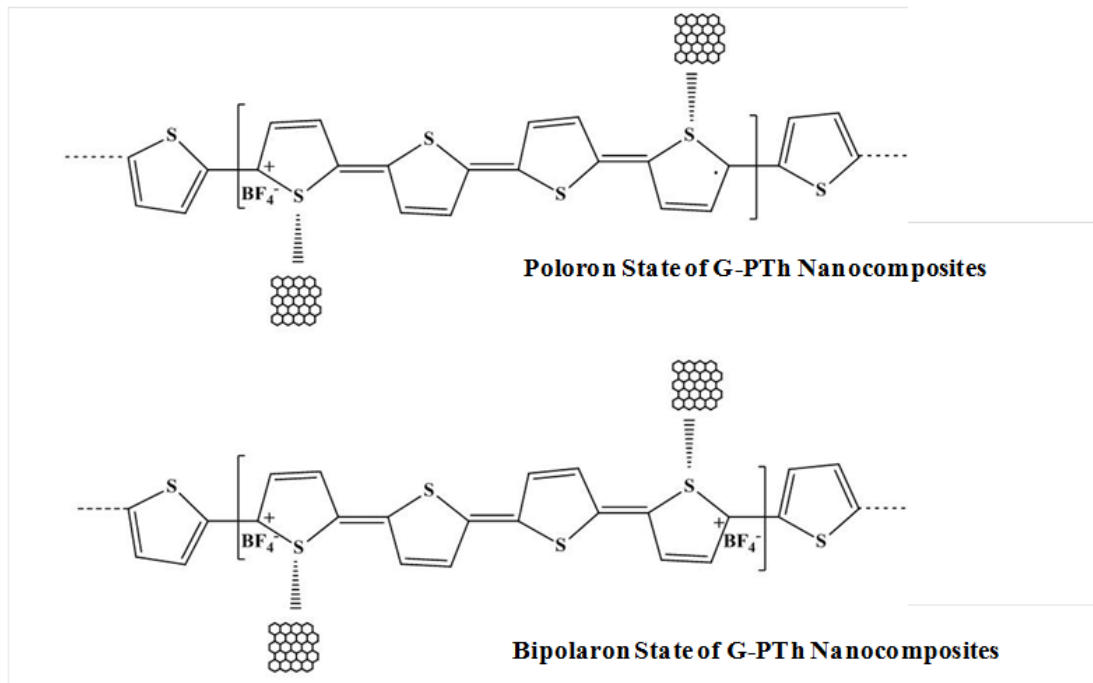


Figure 51. Schematic of chemically synthesized G-PTh nanocomposites.

As shown above the schematic represents the existence of a polaron and a bipolaron state in G-PTh nanocomposites. The CP polymer backbone structure and graphene provide a pathway for free charge to move through the polymer backbone chain via a sequential delocalization with π -bonds (hopping) under an applied electric field. Compared to polaron, a bipolaron state is more stable and promising in the electronic application. However the cause of occurrence of bipolaron state in PTh is due to either n type doping and p type doping and the removal or addition of electrons from π -system [100, 101].

5.1.2 Structural Characterization of G-PTh Films

The structural investigation includes the morphology and feature size of prepared G-PTh nanocomposite studied by Field Emission Scanning Electron Microscopy (FESEM), TEM and XRD. Further the Raman and FTIR study was also carried out to collect the information regarding the Raman Shift and absorption bands of inter and/or intra-gap states. For all characterization the G-PTh film mixed in chloroform was deposited on p-type silicon substrate (100) by drop casting.

5.1.2.1 Scanning Electron Microscope (SEM) and Transmission Electron Microscope (TEM) Studies

SEM images taken with Hitachi S-800 of G-PTh films undoped and doped of different magnifications are shown in Figure 52(a,b). SEM images reflect the sponge-type structure of G-PTh nanocomposite. The sponge like structure is more likely to have a large surface film area. In fact the large surface area is highly desirable for the supercapacitor application. However it has remained difficult to distinguish graphene from polymer in G-CPs SEM image. This kind of porous electrode material is much promoted with electrolyte intercalation in return to good capacitance. Figure 53(a, b) shows TEM and HRTEM images of G-PTh nanocomposite taken by Technai F20. TEM images reveal the graphitic laminar structure in G-PTh material. TEM samples are prepared by adding a small amount of G-PTh dry powder to ethanol, and a drop of solution is dropped on 300 mesh copper TEM grid. Further, it is dried at room temperature for 30minutes. The G-PTh shows different oriented graphene plates in composite within conducting polymer, and exhibits small pores. HRTEM shows the well-arranged graphene sheets around the PTh chain. However, the agglomeration of some

graphene particles with the PTh network can also be examined [102]. The selected area diffraction (SEAD) patterns in TEM images are also the evidence of good crystalline quality of G-PTh nanocomposite. The average calculated particle size of a G-PTh nanocomposite is approximately 40 to 60 nm. The increase in particle size is due to the combined influence of graphene and polythiophene particles in nanocomposite.

5.1.2.2 Raman Studies

Figure 54 shows the Raman spectra of the G-PTh polymer on a silicon substrate. Raman bands can be observed at the peaks of the feeble bands (736, 693), 1238, 1542, 1600, 1728 and 2421 cm^{-1}). The presence of graphene in G-PTh nanocomposite is verified due to the typical intense G band in Raman spectra which is located at 1575 cm^{-1} . However, the band at 1238 cm^{-1} is due to the $\text{C}_\alpha\text{-C}_\alpha$ stretching that occurs in thiophene ring. Similarly, the bands at (736 cm^{-1} and 693) cm^{-1} are the very characteristics C-S-C (rig deformation) of G-PTh [103]. Generally speaking the existence of prominent peaks in G-PTh Raman spectra reflects the successful incorporation of graphene within a polythiophene network during chemical polymerization.

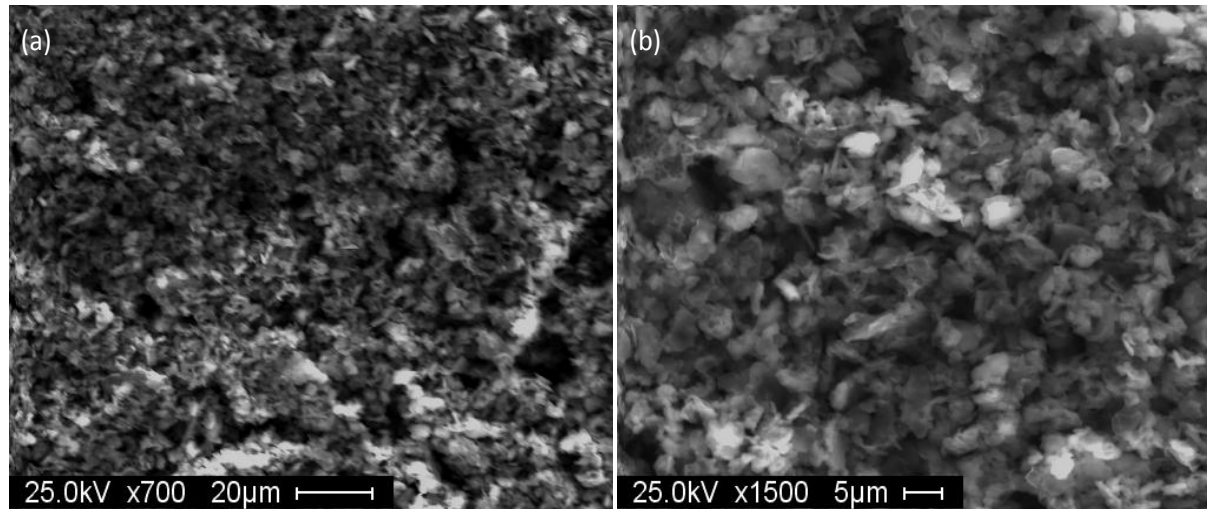


Figure 52. SEM images of (a) undoped (b) doped G-PTh nanocomposite.

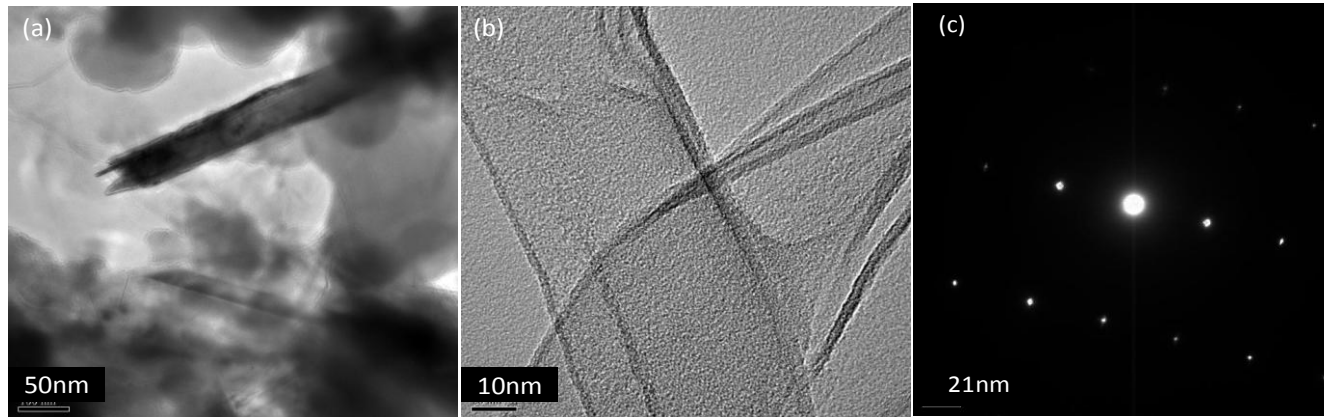


Figure 53. (a) TEM (b) HRTEM and (c) SEAD images of G-PTh nanocomposite

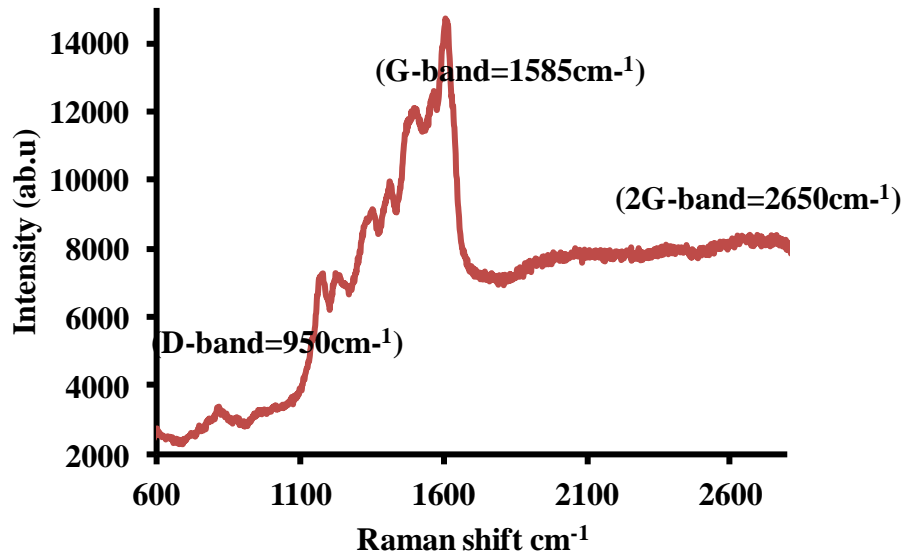


Figure 54. Raman spectra of G-PTh nanocomposites.

5.1.2.3 FTIR

Figure 55 shows the FTIR spectra of the PTh, G and G-PTh nanocomposites measured using a KBr pellet. FTIR spectra shows bands for graphene at 1434, 1649, 2902, 2966, 3447 cm^{-1} , the bands for thiophene at 570, 618, 708, 843, 891, 893, 1000, 1075, 1218, 1226, 1450, 1585, 1698, 2415, 1998, 3452, 3760, 3890 cm^{-1} , and bands at 1458, 1708 cm^{-1} for G-PTh nanocomposite materials. The most notable stretchings in FTIR spectrum are due to (C-H), (C=C), (C-H) and (C-S) stretching vibration bands at 2923 cm^{-1} ; 1458-1596 cm^{-1} ; 1113 cm^{-1} and at 749 cm^{-1} [98]. The origin of C=C stretching vibration caused by the thiophene ring is clearly observed at the band of 1585 cm^{-1} . Band induced due to the doping in the polymer chain arises at 1021 cm^{-1} , whereas the bands due to the counter ions balancing appears at 1113, 1309 and 1458 cm^{-1} [103,104].

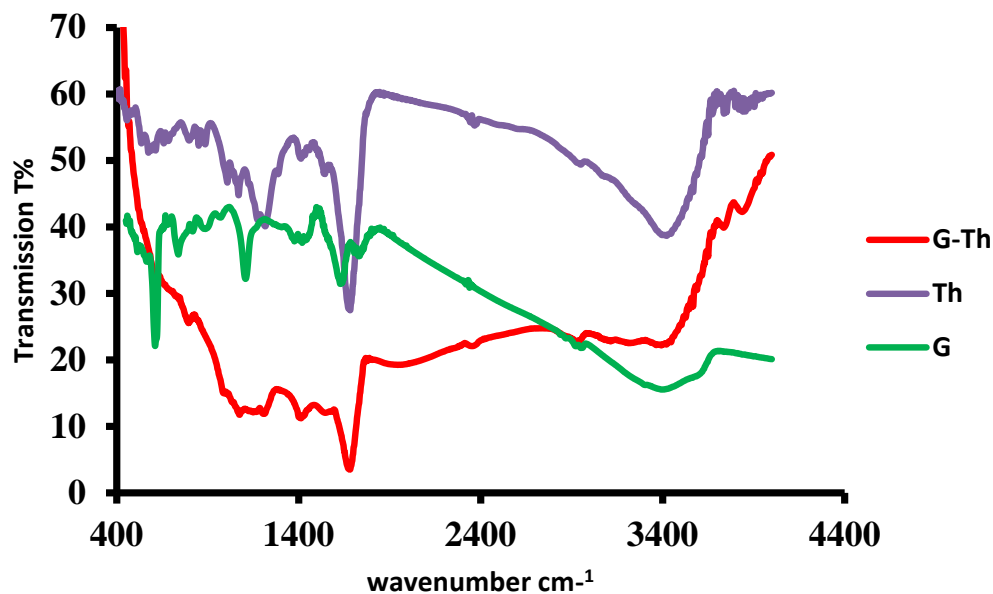


Figure 55. FTIR spectra of G-PTh nanocomposites.

The C-O and C-C vibrations bands are the very characteristics of graphene which are shifted to 1708 cm^{-1} and 1438 cm^{-1} in G-PTh nanocomposite. The increased conjugation shifted to the absorption frequencies and resulted in the polymerization of G-PTh nanocomposite. The broad band at $3000\text{-}3500\text{ cm}^{-1}$ is assigned to N-H and C-H stretchings.

5.1.2.4 X-Ray Diffraction

The XRD result of G-PTh nanocomposite is shown in Figure 56. The obtained XRD pattern indicates the crystallinity of the synthesized material by the appearance of sharp and well-defined peaks, at 7.37 , 8.25 , 13.53 , 15.11 , 20.19 , 22.55 , 23.81 , 26.43 , 37.27 , 38.13 , 41.23 , 61.49 , 65.73 and 69.5 degrees. The obtained diffractogram (Figure 56) exhibits not only the peaks of the PTh situated at the low angle 20° , but also exhibits the presence of graphene in it [104, 105].

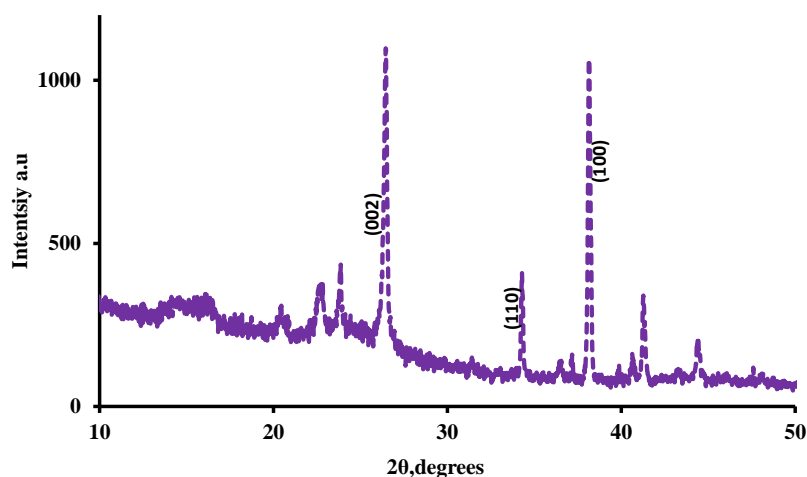


Figure 56. XRD plot of G-PTh nanocomposites.

The presence of plane [002] and [100] at 25° and 37° represents the crystalline nature of G-PTh due to the existence of graphene sheets in it [98, 106]. However, intensity, sharpness and width of these peaks depend upon the amount of graphene in the nanocomposite. The average particle size of the G-PTh film was estimated based on the Scherrer correlation for a particle diameter (d) with peak width. The average size of the particles calculated from the width of the diffraction peak, according to the Scherrer equation, is around 70nm to 90nm for the G-PTh nanocomposite.

5.1.3 Electrochemical Measurements

5.1.3.1 Electrode Preparation and Electrochemical Setup

The synthesized G-PTh material was mixed with chloroform and the film of approximately $30\mu\text{m}$ thickness was cast on graphite substrate. The electrochemical measurements (cyclic voltammetry, charging/discharging and impedance analysis) were

estimated in a cell containing the G-PTh nanocomposite as a working electrode and a counter electrode. We have fabricated a supercapacitor with G-PTh as electrodes materials in the electrolytic solutions of 2MH₂SO₄, 2MHCl, 0.5MLiClO₄ and room temperature IL.

5.1.3.2 Capacitance Evaluation of G-PTh Film

Cyclic voltammetry (CV) responses of G-PTh film coated on graphite electrodes as a function of the scan rates of 10 mV/s (1) 20mV/s (2) 50mV/s (3) and 100 mV/s (4) are shown in Figures 57. All CV measurements for a G-PTh based supercapacitor were recorded at room temperature in a potential window from 0 to 1V. Figure 57(a, b, c, d) gives the comparative study of CV profile of G-PTh films in different electrolytes (e.g., 2MHCl, 2MH₂SO₄, 0.5MLiClO₄ and IL). Moreover, the CV study of G-PTh reveals the pseudocapacitance in aqueous based HCl and H₂SO₄ electrolytes but lacks the pseudocapacitance in 0.5M LiClO₄ and PF₆. It has been noted that with the change in voltage sweep rate from 10 mV/s to 100 mV/s, the cathodic peak (0.45V) shifts positively and the anodic peak (0.65V) shifts negatively in HCl and H₂SO₄ solution. The presence of a distinct peak centered at 0.5 V corresponds to the oxidation of the G-PTh nanocomposite [98, 104]. Faradic transformation in G-PTh is responsible for the existence of doped and undoped states in the G-PTh films and it leads to the formation of peaks. By comparison, all the CV curves show the deformed rectangular shapes which significantly deviate from an ideal rectangular box. However, by comparison, the CV profile for H₂SO₄ has a larger surface area than the CV shapes of HCl, LiClO₄ and IL. It might be due to the higher electronic conductivity and improved diffusion mechanism in H₂SO₄ electrolyte which yields less resistance and a larger surface area. Figure 57(c)

shows the wide oxidation peak at 0.53V in LiClO₄ which describes the reversible redox system in an organic electrolyte. However, no specific oxidation peak was observed for ionic liquid rather than it shows more like EDL behavior. It clearly indicates that among all electrolytes, H₂SO₄ is giving higher specific capacitance due to improved electroactive performance. Capacitance starts decreasing with because of the sweep rate change from 10mV/s to 100mV/s for all electrolytes as given in Figure 58. It ascribes the limitation of electrolyte access in 3D electrode dimension due to the higher pore resistance at higher sweep rate. However, rate of decreases in specific capacitance in 2MH₂SO₄ is less than other electrolytes, which might be due to higher ionic and electronic conductivity besides the low ESR.

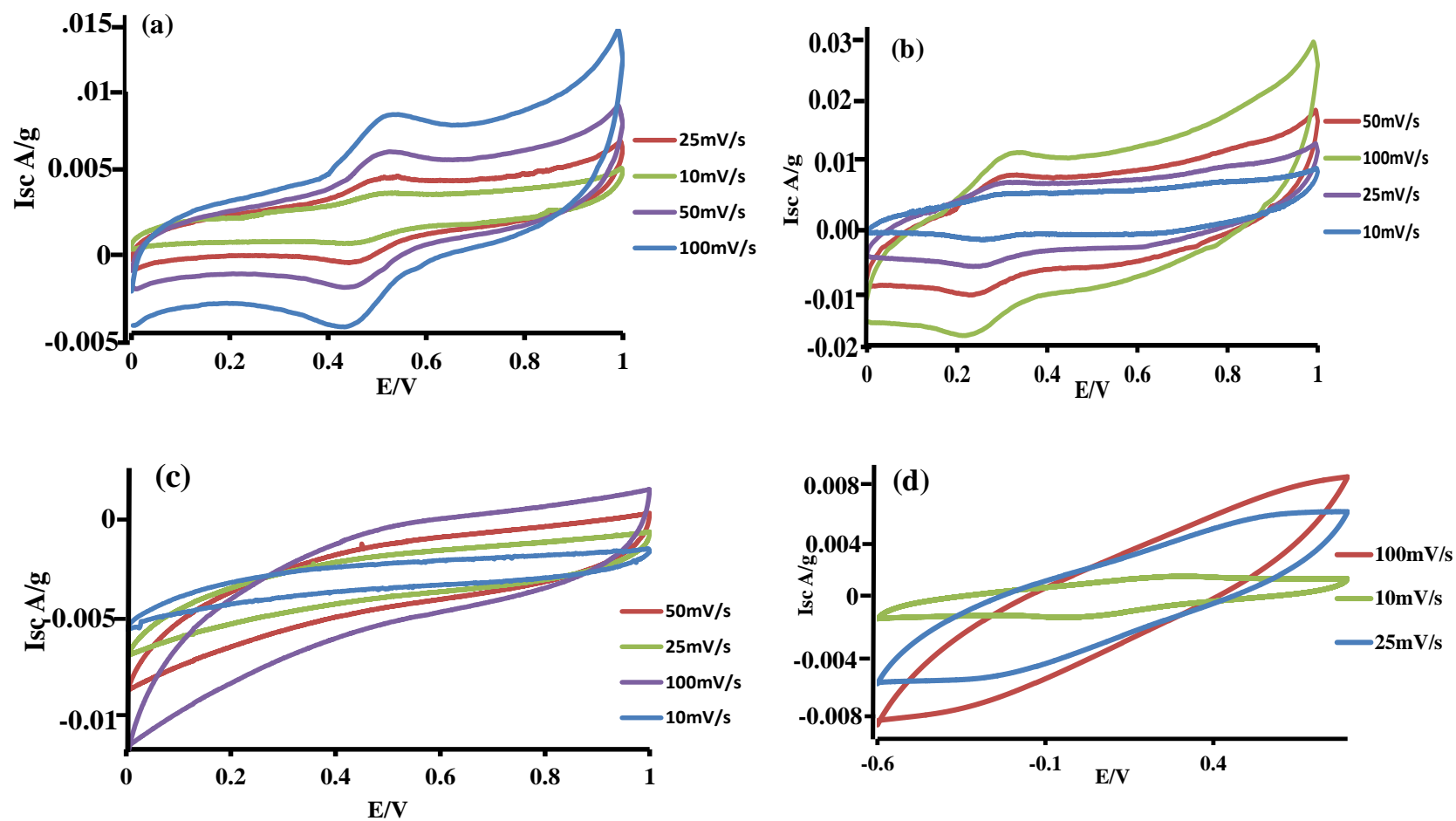


Figure 57. Current-voltage response of G-PTh nanocomposites in (a) 2MHCl (b) 2MH₂SO₄ (c) LiClO₄ (d) IL.

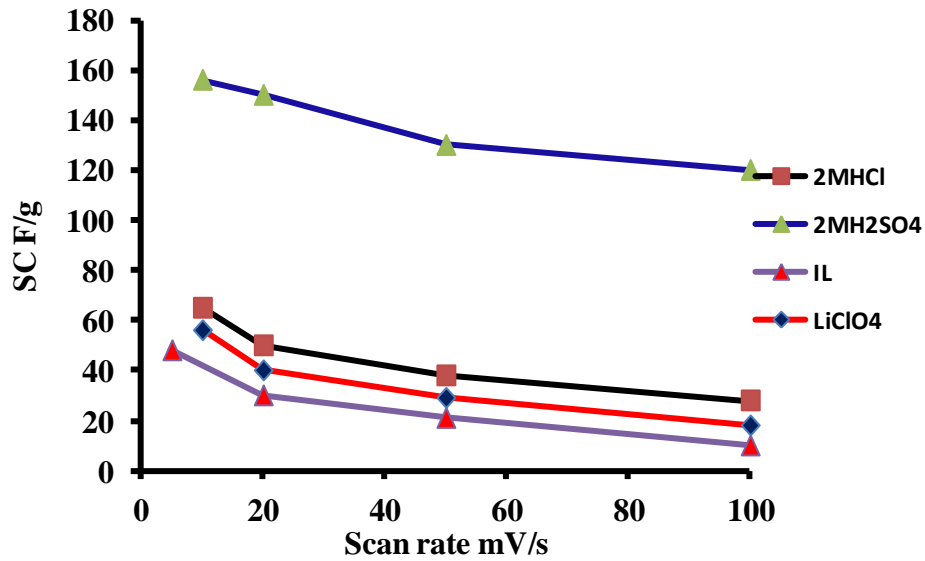


Figure 58. Specific capacitance versus scan rates of G-PTh nanocomposites in (a) 2MHCl (b) 2MH₂SO₄ (c) LiClO₄ (d) IL.

In addition to CV discussion, charge/discharge behavior has also been studied to further understand the capacitance influence for G-PTh nanocomposite. Figure 59 depicts the charging-discharging behavior of G-PTh nanocomposite at a current density of 0.2A/g. The voltage ranges are from 0 to 1.2 V in 2MHCl, 0 to 1.5 V in 2MH₂SO₄, 0 to 2.2 V in 0.5 M LiClO₄ and 0 to 2.75V in IL. The charging and discharging has been found to be quite symmetrical in Figure 59 in spite of different electrolytes. The discharge capacitance 'C_d' has been evaluated from the discharge curves using the equation 18 [98, 104-107].

$$C_d = \frac{I \times \Delta t}{\Delta V \times m} \quad (18)$$

where I is the constant current, Δt is the time interval for a voltage change of ΔV and m is the mass of the film coated over the graphite substrate.

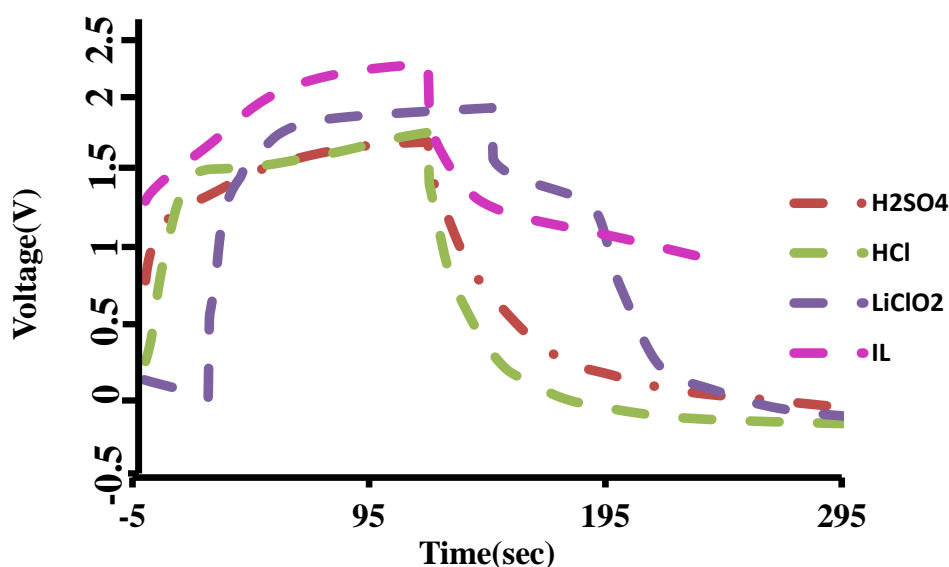


Figure 59. Charging-discharging profile of G-PTh nanocomposites in (a) 2M HCl (b) 2M H₂SO₄ (c) LiClO₄ (d) IL.

The estimated specific capacitances for 2M H₂SO₄, 2M HCl, 0.5M LiClO₄ and IL are as 169, 75, 45 and 30F/g. Specific capacitance results obtained by chrono potentiometry are in agreement with the CV results. The columbic efficiency η of G-PTh electrodes was also calculated for all four electrolytes given in Figure 60. The initial decrease in efficiency is due to irreversible redox reactions, however later it gets stable. The columbic efficiency for H₂SO₄ has been found approximately 89% over the 400 cycles. It clearly indicates the potential of G-PTh electrodes to be used in a fast and durable supercapacitor.

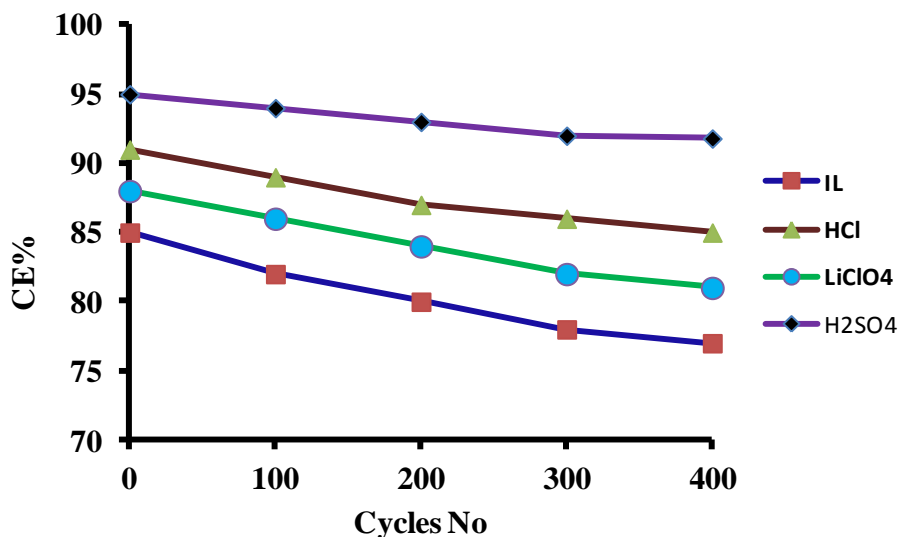


Figure 60. Columbic efficiency versus number of cycles of G-PTh nanocomposites in (a) 2M HCl (b) 2M H₂SO₄ (c) LiClO₄ (d) IL.

Besides the columbic efficiency study of G-PTh electrodes, the cyclic stability of the prepared nanocomposite was also analyzed upon cycling in different electrolytes as shown in Figure 61. The better cyclic stability due to the higher specific capacitance is realized for 2M H₂SO₄ than other electrolytes. This clearly manifests the higher stability and superior electrochemical characteristics of G-PTh in H₂SO₄. Therefore, it is concluded that ions and charge transport capabilities of electrolytes play a dominant role in improving the capacitance.

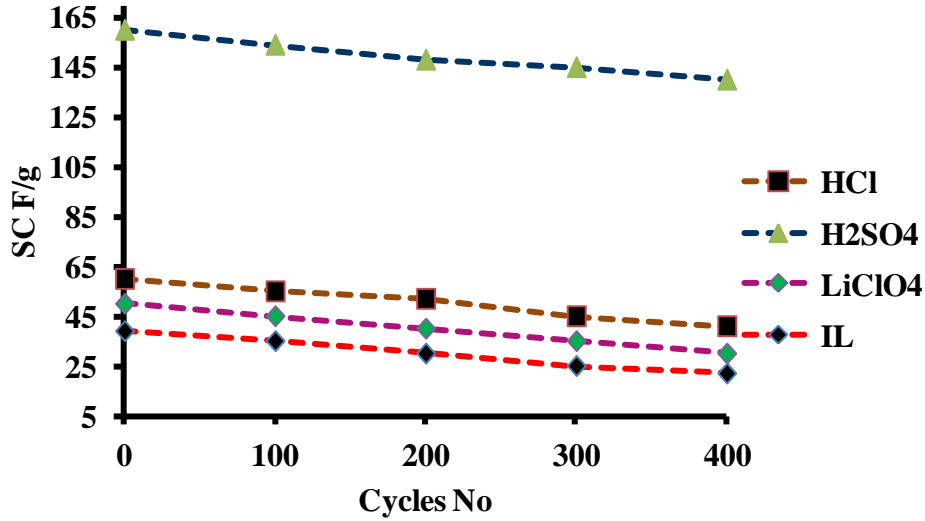


Figure 61. Specific capacitance versus scan rates of G-PTh nanocomposites in (a) 2MHCl (b) 2MH₂SO₄ (c) LiClO₄ (d) IL.

Performance of the G-PTh nanocomposite for the electrochemical capacitor can be better understood by analyzing the Ragone plot given in Figure 62. Ragone plot for G-PTh for H₂SO₄, HCl, LiClO₄ and IL shows the higher energy density for the H₂SO₄ solution where as a higher power density was obtained for IL [108]. It means that the different electrolytes have different significance, but overall enhancement in the performance of G-PTh based capacitor has obtained in H₂SO₄. However, further investigation is still needed in regards to the scope of electrolyte in the performance improvement of the supercapacitor.

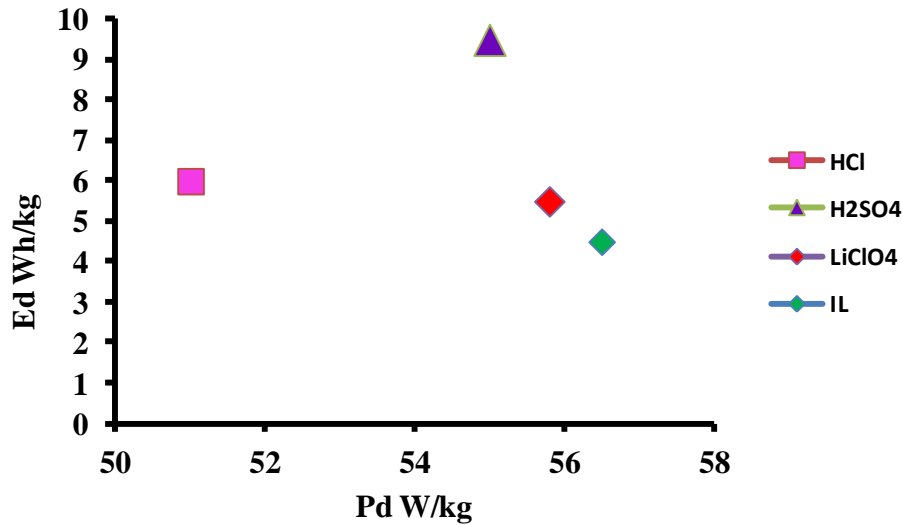


Figure 62. Ragone plot of G-PTh nanocomposites in (a) 2MHCl (b) 2MH₂SO₄ (c) LiClO₄ (d) IL.

5.1.3.3 Impedance Study

Figure 63 reflects the Nyquist plots of G-PTh supercapacitor for a frequency range of 100 mHz to 100 kHz. The good capacity like behavior of G-PTh nanocomposite has been observed in high frequency region. The internal resistances are found to be 0.7, 1.0, 12.6 and 100 Ω in 2M H₂SO₄, 2M HCl, 0.5M LiClO₄ and IL respectively. IL shows the higher internal resistance which is associated with the bigger ionic size of IL and offers high diffusion limitation to the counter ions. The Nyquist plot revealed that H₂SO₄ provides a high conductive medium. A small semicircle was observed in the high frequency region in the 0.5M LiClO₄ and IL electrolytes due to high series resistance and less ionic conductivity.

However, there is no semicircle detected in impedance measurements of aqueous electrolytes in the high frequency range. This implies that both H₂SO₄ and HCl are more conductive than LiClO₄ and IL. The important criteria to exhibit an ideal capacitor

behavior, that the doping/dedoping rates in G-Cps are fast enough to provide a constant current during the redox reaction [109]. The charge (electrons or holes) and ionic transport mechanism are responsible for the doping/dedoping process in the G-PTh nanocomposite. However the charge/discharge mechanism of the G-PTh determined by the ionic transport rate because it is slow compared to the charge transport rate [110]. In comparison to the high frequency response of G-PTh nanocomposites in different electrolytes, it also shows the desirable response in low frequency regions. All the impedance curves are inclined at a certain angle between an imaginary and real impedance axis, which develops due to the existence of Warburg impedance at the electrode and electrolyte interface. However, among all electrolytes, the slope of impedance curve in 2M H₂SO₄ tends more towards the imaginary axis revealing the ideal capacitive behavior of G-PTh film in 2M H₂SO₄.

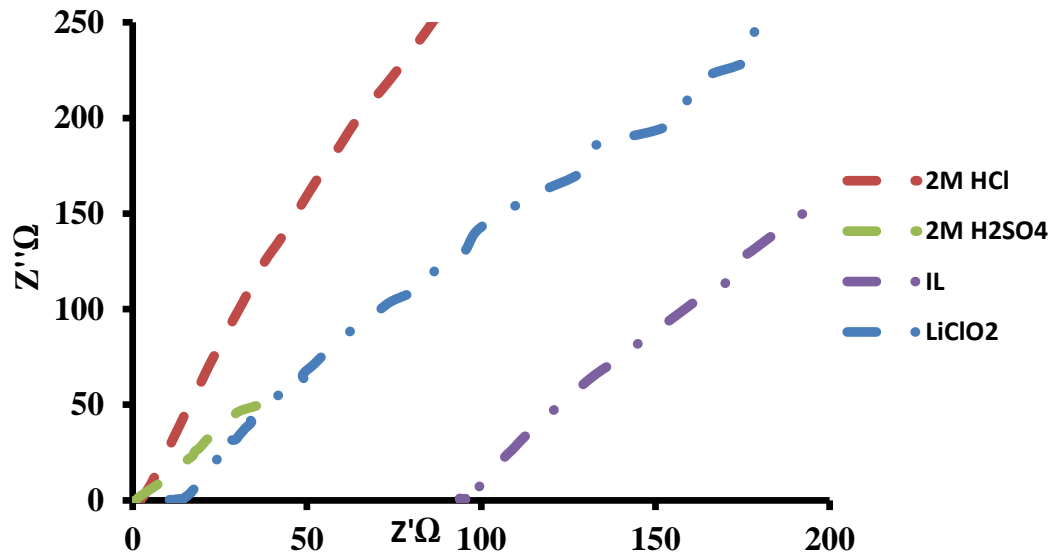


Figure 63. Impedance analysis of G-PTh nanocomposites in (a) 2MHCl (b) 2MH₂SO₄ (c) LiClO₄ (d) IL.

5.2 Summary

G-PTh nanocomposite material was synthesized by the oxidative polymerization technique, and characterized using various physical and electrochemical techniques. The FTIR and Raman studies of G-PTh films have shown that graphene plays a dual role in improving the overall conductivity of a PTh system, by acting as a dopant and also forming nanocomposites with the PTh conducting polymer. The G-PTh structure dramatically improves the electrochemical performance in PTh based supercapacitor. The G-PTh supercapacitor electrode provides a faster electrochemical reaction with an average capacity of 174 F/g. Further improvements in the electrochemical performance of the supercapacitor can be obtained by optimizing the electrolytes, thickness of electrodes materials, cell design and the electrode material containing different ratios of thiophene to graphene in the nanocomposite structure. Nevertheless, at this point this study provides a fundamental understanding for high performance organic electronic devices based on PTh and graphene nanocomposite material.

CHAPTER 6: EFFECT OF SUBSTITUTES IN HETEROCYCLIC BASED CONDUCTING POLYMER

Poly (3, 4-ethylenedioxythiophenes) (PEDOT) among all polythiophene derivatives is the extensively studied material due to its interesting characteristics (e.g. high conductivity, good transparency, moderate band gap, low redox potential and high thermal and chemical stability at room temperature.) [111]. Since the PEDOT has good stability during oxidization in both doped and undoped states, it is considered one of the potential candidates for commercial use in electronic applications.

Further structural modification of the polymer backbone and its high conductivity which is around 300 to 550 S/cm and fast electrochemical switching behavior allows this polymer to be used as electrodes of electrochemical capacitor [112].

However like other polymers PEDOT faces the same challenges related to volume changes (e.g. shrinkage, breaking, cracks due to intercalation/deintercalation of counter ions upon cycling which limits its use in a fast electrochemical capacitor). In order to exploit the full potential of a stable PEDOT polymer in ambient conditions, recent composite material has gained wide attention due to the improvements in the specific capacitance and mechanical and thermal properties of materials. As it has been discussed in detail in chapters 2, 3, 4 and 5 graphene is a promising material due to its extraordinary properties besides from the low cost in the fabrication of nanocomposite. So here we are discussing the synthesis characterization, and application of G-PEDOT material and investigating the role of G-PEDOT nanocomposite as supercapacitor electrodes.

6.1 Synthesis of G-PEDOT

Synthesization of G-PEDOT nanocomposite was done with a facile and low cost, low temperature chemical polymerization approach. In order to play with the tunability of length, porosity and structure of a polymer, the oxidant is one of the significant factors. So during chemical synthesis of PEDOT, we used the ammonium peroxydisulfate $[(\text{NH}_4)_2\text{S}_2\text{O}_8]$ and FeCl_3 as oxidants under controlled conditions. Figure 64(a, b) shows a polymerization schematic of ethylene dioxythiophene (EDOT) with graphene nanoparticles. In order to resolve the solubility of PEDOT, first sodium polystyrene sulfonate Na salt (PSS) was dissolved in IMHCl solution set at 1PH for two hours. Next the EDOT monomer was added in the PSS solution and mixed for another two hours [113].

Graphene, of having a weight ratio of 1:1 to EDOT monomer, was added next to the PSS solution and again mixed for 1hour. Before the addition of oxidants, the PSS resulting solution was kept in an ice bath and temperature was reduced to -4°C . The PSS solution was later followed by the slow addition of oxidants, 0.05M ammonium peroxydisulfate and 0.05M FeCl_3 . The polymerization was observed within 5 to 10 minutes of the drop wise addition of oxidants as the solution changed its color to dark purple-green. After the addition of oxidants, the ice bath was removed around the reaction vessel and the final reaction was stirred for next 24 hours. Finally, the recovered G-PEDOT nanocomposite from the reaction vessel was filtered, and washed thoroughly using deionized water, methanol, acetone, and diethyl ether to eliminate low molecular weight polymers and oligomers [114]. Further recovered doped G-PEDOT precipitate was dried in a temperature-controlled oven at 100°C for 3hours. For the use of G-PEDOT

in ECs it was converted into its undoped form by mixing in the 2M solution of NH_3OH for another 6hours. In the end, again, the desired material of a dark purple-bluish color was washed thoroughly with deionized water, methanol and dried in the oven at 100°C for 2hours.

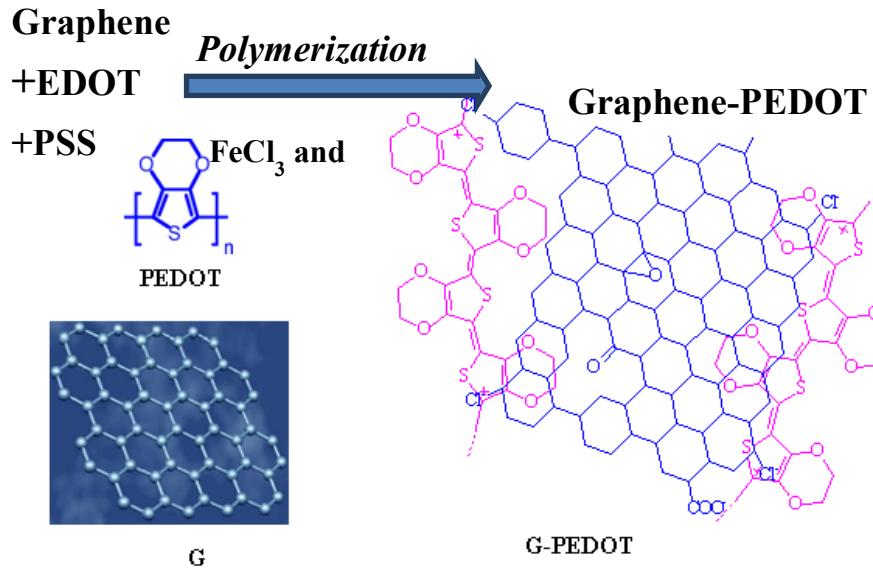


Figure 64. Schematic of G-PEDOT nanocomposites.

The morphology and crystalline structure of synthesized G-PEDOT was then characterized by field emission scanning electron microscopy (FESEM), high-resolution transmission electron microscopy (HRTEM) and X-ray diffraction technique. In addition to structural techniques the G-PEDOT was also optically characterized by Fourier transform infrared (FTIR) spectrophotometer, Raman spectroscopy to collect information regarding the Raman shift, and absorption bands of inter and/or intra-gap states. For all above characterization the G-PEDOT film was deposited using a doctor blade method on a p type 100 silicon substrate.

6.2 Results and Discussion

6.2.1 Characterization of G-PEDOT

Figure 65(a) shows the SEM picture of undoped G-PEDOT nanocomposite having flake-like morphology possibly due to the formation of a nanocomposite structure with G. In order to see the effect of doping the G-PEDOT film was doped in 1M HCl for a couple of minutes. Figure 65(b) simply shows that the HCl doped, G-PEDOT film has a higher surface roughness as well as wide pore size distribution areas. Though no significant difference was observed in the morphology of doped and undoped G-PEDOT films [114, 115], average particle size of synthesized G-PEDOT material is found to be around 80nm to 90 nm. Therefore, from SEM images of G-PEDOT depict the successful synthesis of nanocomposite with the promising, large surface area morphology to attain the good capacitive behavior.

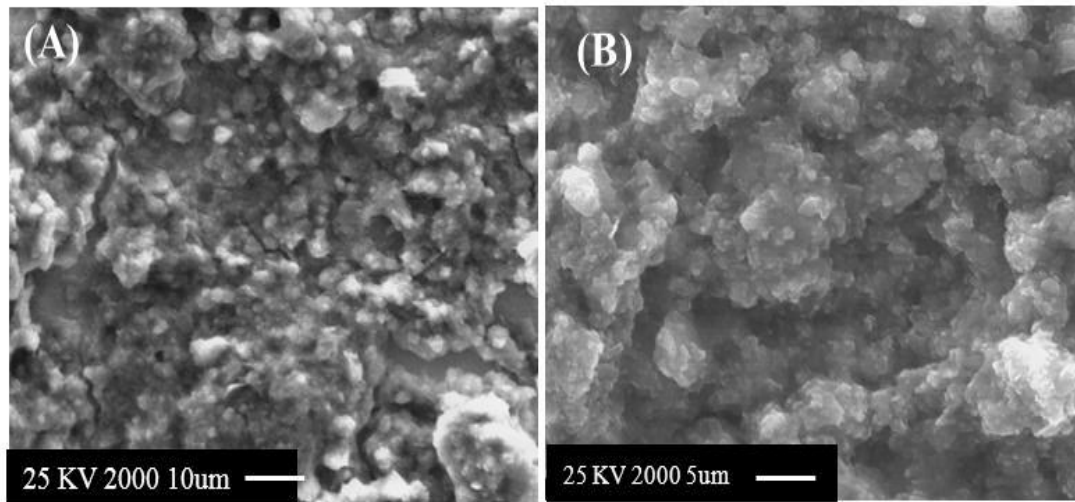


Figure 65. SEM images of undoped (a) and doped (b) G-PEDOT nanocomposites.

In regards to crystallinity of G-PEDOT nanocomposite, Figure 66(a, b) shows the TEM and HRTEM images of G-PEDOT. The graphitic laminar structure could be observed in G-PEDOT nanocomposite material. The TEM image of G-PEDOT depicts

the successful incorporation of graphene within PEDOT particles. However, some of these particles also represent the agglomeration of PEDOT particles within graphene sheets. This may be caused by the synergetic effect of graphene within PEDOT network. An HRTEM image of G-PEDOT reflects the crystalline order of synthesized material which shows the superior hierarchy structure of the synthesized material. Average particle size of the synthesized G-PEDOT was found to be equal to 70 to 100nm, which is consistent with the SEM results. Also, the good crystallinity of prepared G-PEDOT is seen due to the regular SAED diffraction pattern inset in the TEM image.

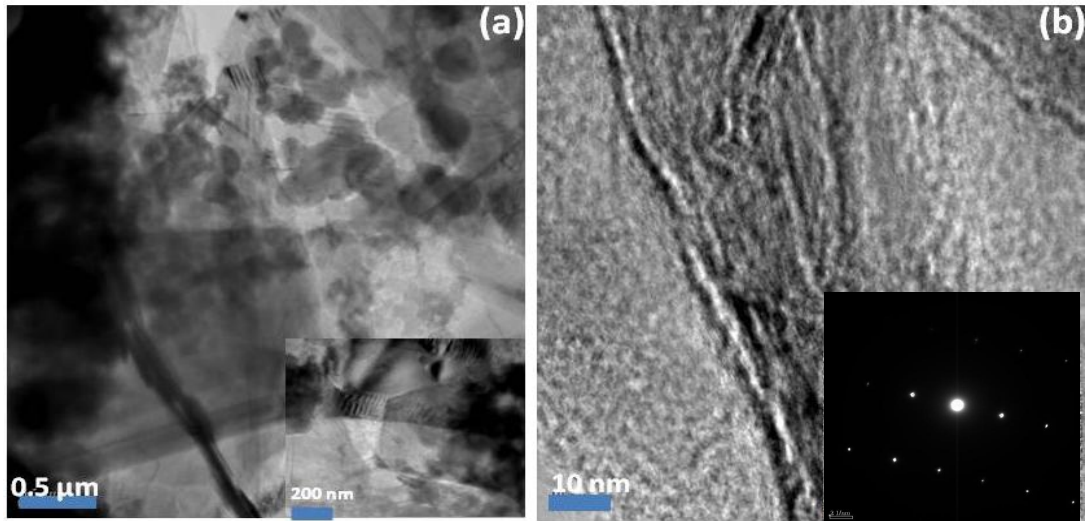


Figure 66. (a) TEM and (b) HRTEM images of G-PEDOT nanocomposites.

6.2.2 FTIR

The FTIR spectra of Graphene and G-PEDOT nanocomposite in potassium bromide (KBr) pellet were measured as shown in Figure 67. FTIR spectra of G-PEDOT exhibits bands at 782, 1178, 1305, 1388, 1524, 1634, 1664, 2900, 2928, 3296, 3476, 3887 and 3785 cm^{-1} [114]. Stretching vibrations of C=C and C-C due to the quinoidal structure of the thiophene ring has been observed at bands at 1634 and 1305 cm^{-1} [116]. Another C-O-C stretching vibration in G-PEDOT spectra was also observed at band 1178 cm^{-1} indicating the successful incorporation of graphene in PEDOT during chemical polymerization. Compared to graphene in G-PEDOT film, the broader peaks due to the C=C and C-C and C-O-C stretching are observed at bands 1650, 1325 and 1190 cm^{-1} which simply explains the higher absorption property of G-PEDOT material.

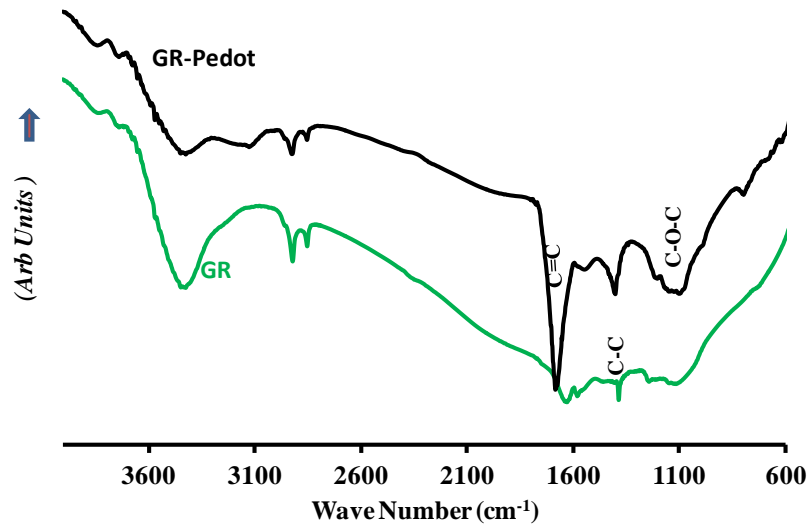


Figure 67. FTIR spectra of G-PEDOT nanocomposites.

6.2.3 Raman Spectroscopy

Figure 68 depicts the Raman spectra for the G-PEDOT film consisting of peaks at 1550, 1590, 1685, 3060 and 3100 cm^{-1} . In G-PEDOT Raman spectra, a broadened G-band was observed at 1590 cm^{-1} . The important thiophene ring vibration was noticed at 1685 due to the α -H bonds and C=S vibration at 3060 and 3100 cm^{-1} . These are found due to the β -H bonds in the thiophene ring. Six dominated bands in thiophene spectra are observed at 1550 (Quinoid structure), 1487, 1424 (Ca=Cb stretching), 1185 (C-C stretching), 986 (C-C alkyl stretching), 891 (C-H bending) and 834, 766 cm^{-1} (C-S-C ring deformation). However, the presence of D, G and 2G bands at 1150, 1545 and 2650 cm^{-1} clearly indicates the successful incorporation of G in the PEDOT structure [114,118].

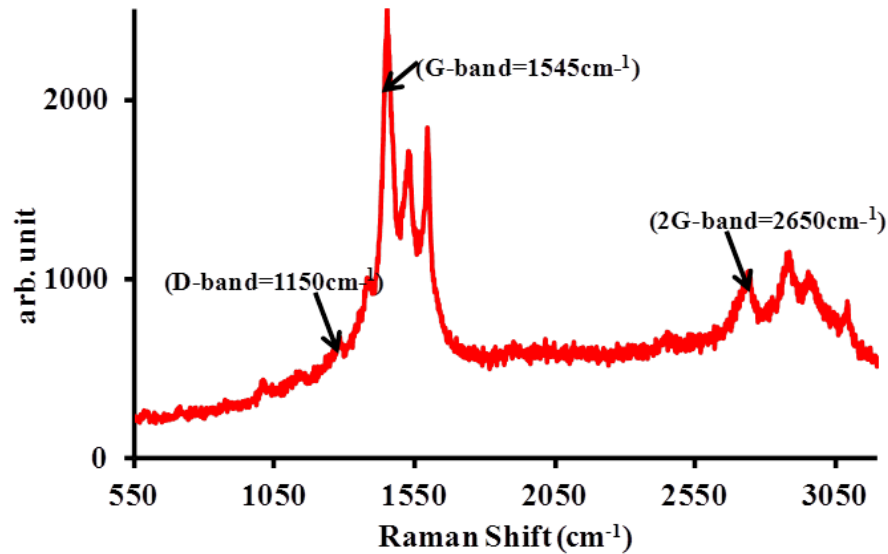


Figure 68. Raman spectra of G-PEDOT nanocomposites.

6.2.4 XRD

As far as crystallographic information is related for G-PEDOT films Figure 69 depicts the X-ray diffraction patterns of G-PEDOT nanocomposites. The sharp and intense peaks can be observed in the obtained XRD which simply indicates the good crystallinity of the synthesized material. Existence of the low angle peak at 20° indicates the amorphous nature of PEDOT. Figure 69 shows the X-ray peaks at 6.34, 13.75, 26.43, 33.45, 37, 57, 43.73, 51.37, 53.91, 61.7, and 63.31 degrees for the doped G-PEDOT films indicating more improved crystalline structure than the undoped G-PEDOT nanocomposites material [114,112,119]. Estimated average particle size of the synthesized material using the Scherrer equation has been found around 70nm. Particle size estimation of G-PEDOT using Scherrer equation is consistent with TEM results.

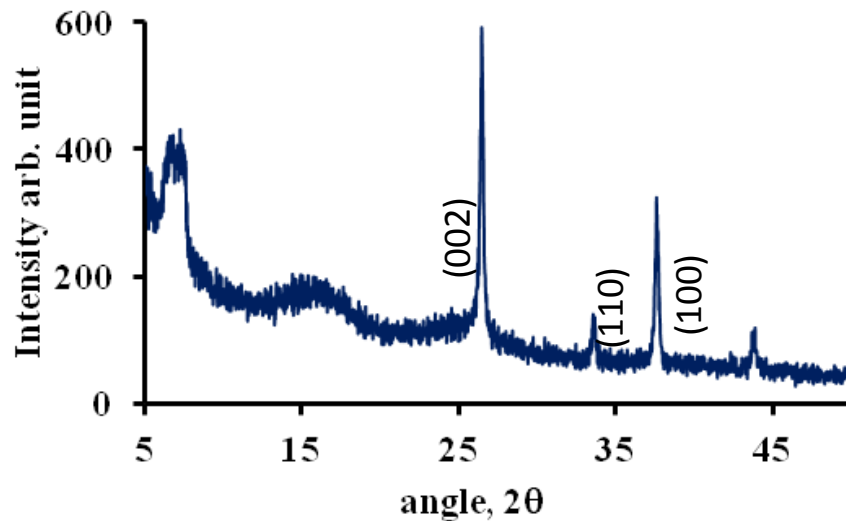


Figure 69. XRD analysis of doped G-PEDOT nanocomposites.

6.3 Electrochemical Measurements

6.3.1 Electrode Fabrication

The solubility of G-PEDOT is a big question. The capacitance study of G-PEDOT film was done with the mixing of G-PEDOT in Nafion. Nafion here, as well, acts as the binder and solvent for G-PEDOT films. G-PEDOT was fabricated on the graphite substrate by a solution cast technique, which is then dried at 100 °C. Since the 30µm was obtained as optimum thickness as discussed in chapter 3 The G-PEDOT films thicknesses was kept at the same value respectively.

6.3.2 Capacitance Evaluation of G-PEDOT Electrodes

Figure 70(a, b, c, d) shows the current-voltage relationship of Nafion mixed G-PEDOT in 2M HCl, 2M H₂SO₄, 0.5M LiClO₄ and IL as a function of scan rates (1) 5 (2) 20, (3) 50 and (4) 100 mV/s coated on graphite electrodes. This indicates the reversibility of G-PEDOT nanocomposites film and good charge propagation within electrode material. The CV profile of the G-PEDOT nanocomposites as seen in Figure 70(a,b,c,d) resembles a good capacitive behavior which reflects the dominant characteristic of a double layered mechanism due to less ohmic loss (greater conductivity) and higher reversibility [120]. A comparative study shows the deformed rectangular shape of CV profile for all electrolytes, however, a larger surface area was observed in the 2MHCl solution. Therefore, the larger CV area is associated with the good chemical affinity between the G-PEDOT and HCl ions and higher electrochemical stability. The oxidation and reduction peaks, potential were observed at 0.2, 0.45, and 0.67V for 2MH₂SO₄ and 2M HCl. For instance, no prominent oxidation peaks were observed for G-PEDOT in

0.5M LiClO₄ and IL. The lower reduction peak in HCl compared to other electrolytes provides the good electrochemical response at electrode and electrolyte interface.

It is noted that the cathodic peak (0.35V) and anodic peak (0.67) has shifted to slightly towards the right and left directions when potential sweeps change incremental from 5 to 100 mV/sec. Furthermore, the doped and undoped states of G-PEDOT initiate the redox behavior, which is responsible for the formation of peaks in the CV profile. Hence the resultant anodic current increases proportionally with scan rates in the CV measurements.

The CV plot depicts more like double capacitor behavior attributing to the synergetic effect of the incorporation of G particles in a polymer network chain [121]. However, the CVs curves show the successful doping of Cl⁻, ClO₄⁻ and SO₄⁻ ions in G-PEDOT material, reflecting the porous with high conductivity property of the synthesized material.

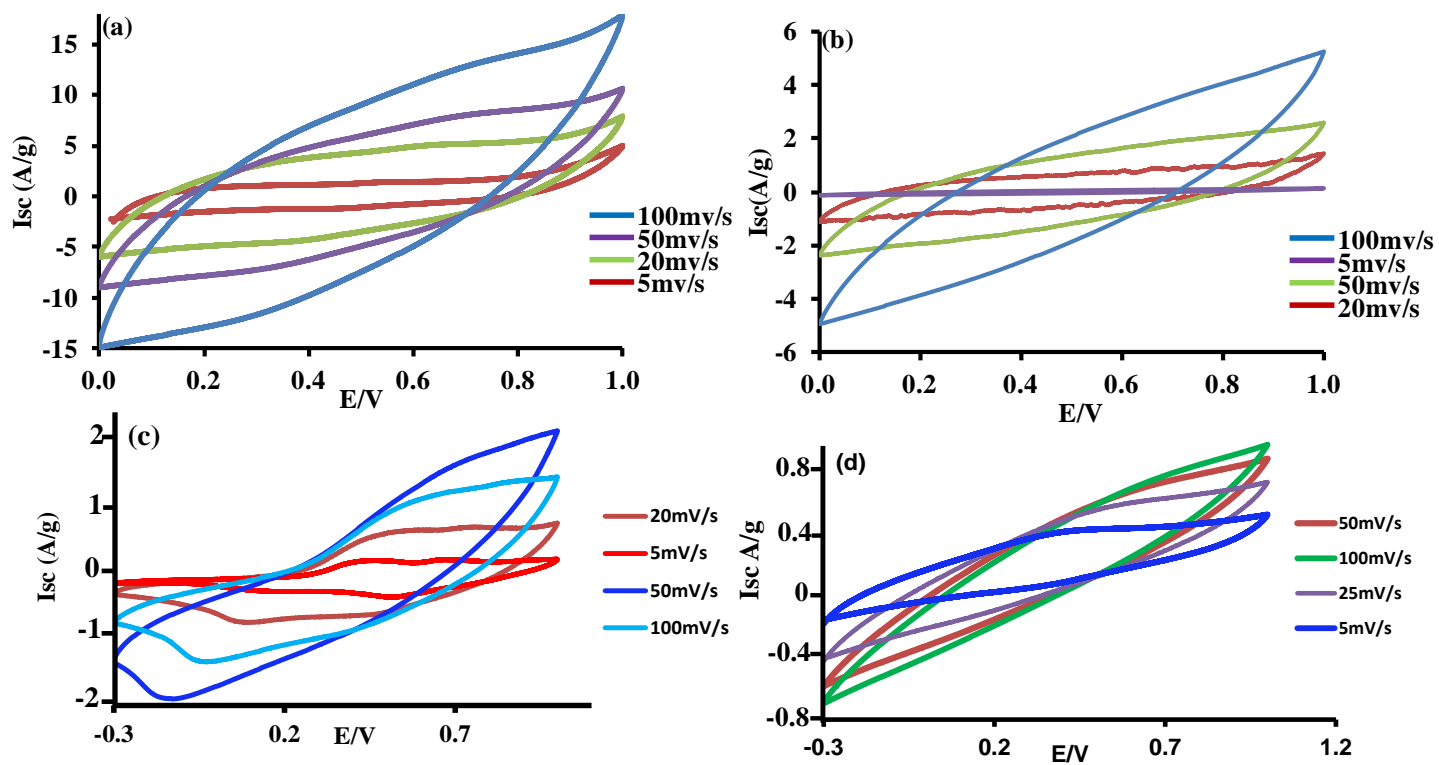


Figure 70. Current-voltage response of G-PEDOT nanocomposites in (a) 2M HCl (b) 2M H₂SO₄ (c) LiClO₄ (d) IL.

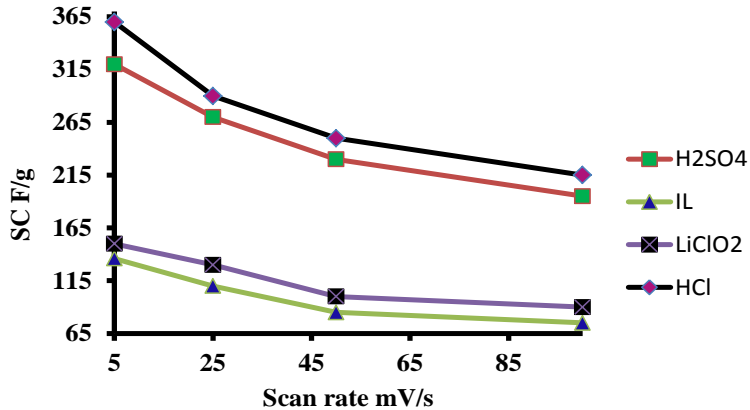


Figure 71. Scan rate versus specific capacitance of G-PEDOT nanocomposites for 5, 25, 50 and 100 mV/s.

Contrary to G-PANI and G-PTh, the specific capacitance value of G-PEDOT nanocomposite is higher in HCl than in H₂SO₄ illustrating a higher electrochemical reaction of an electroactive electrode in an HCl electrolytic medium. Figure 71 shows the decrease in the specific capacitance with the increase in scan rate for HCl, H₂SO₄, LiClO₄ and IL. The decrease in specific capacitance highlights the limitations of ionic diffusion and the reduction in charge storage property of G-PEDOT electrodes at a higher scan rate. However, the rate of decrease in specific capacitance in HCl was found to be less compared to H₂SO₄, LiClO₄ and IL. This clearly indicates the higher electronic and ionic conductivity of G-PEDOT in HCl. The specific capacitance values calculated using CV profile for HCl, H₂SO₄, LiClO₄ and IL at 5 mV/s are 375, 320, 150, and 115 F/g. Figure 72(a, b, c, d) gives the comparison study of the charging-discharging of G-PEDOT in HCl, H₂SO₄, LiClO₄ and IL. Figure 72(a, b) shows the charging-discharging response of G-PEDOT in HCl and H₂SO₄ at the current density of 0.2 A/g. All the charging-discharging curves are triangular in shape and lie within the voltage range of 0.2 to 1.5 V and 0 to 3.5 V. It shows a specific discharge capacitance of 355 F/g for an asymmetric

redox-type supercapacitor with the G-PEDOT nanocomposite in HCl solution, which is close to the value, reported by cyclic voltammetry of 374 F/g. From Figure 72, it is observed that the initial voltage drop during discharging is prominent, and the voltage of the capacitor varies with time during both charging and discharging processes for various numbers of cycles. The low IR drop in HCl charging-discharging curve shows the higher ionic mobility within the G-PEDOT electrode and gives rise to the low diffusion resistance and to the higher specific capacitance. Figure 73 illustrates the comparison analysis of columbic efficiency of G-PEDOT in HCl, H₂SO₄, LiClO₄ and IL. The high linearity and symmetry in the charge/discharge curve of a G-PEDOT based supercapacitor indicates higher columbic efficiency (η) of 95.2%, in HCl than in other electrolytes, which is the ratio of discharge time t_d to charge time t_c . Besides the columbic efficiency the cyclic stability of the G-PEDOT electrode was also studied and is given in Figure 74. The G-PEDOT electrode reflects the good stability in all electrolytes upon cycling for 500 cycles, but the maximum capacity retention was observed in HCl. This ascribes the higher electroactive property of H⁺ and Cl⁻ ions within the G-PEDOT electrode. The detailed estimation of energy storage parameters (e.g., power density and energy density of G-PEDOT nanocomposite in four electrolytes) is given in Figure 75. The average power density for G-PEDOT in HCl, H₂SO₄, LiClO₄ and IL is calculated to be 97W/kg and energy density is estimated to be 12Wh/kg. By comparison the high power capability of G-PEDOT in HCl is attributed to the fast kinetic reaction of porous flake-like structures of G-PEDOT nanocomposite permitting counter-ions to diffuse into the polymer and provides a short diffusion distance to facilitate the ion transport [114, 122].

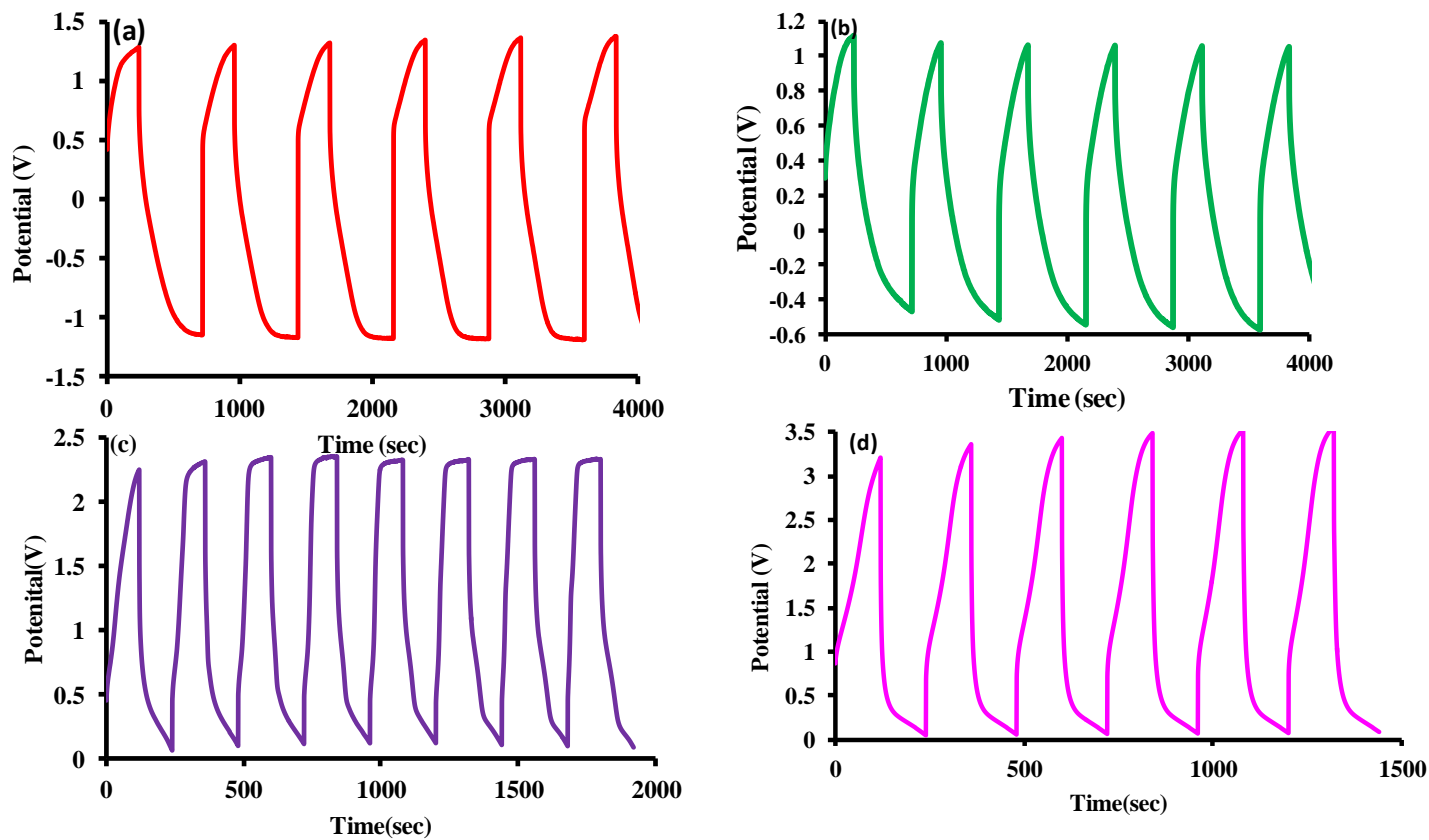


Figure 72. Charging-discharging of G-PEDOT nanocomposites in (a) 2M HCl (b) 2M H₂SO₄ (c) LiClO₄ (d) IL.

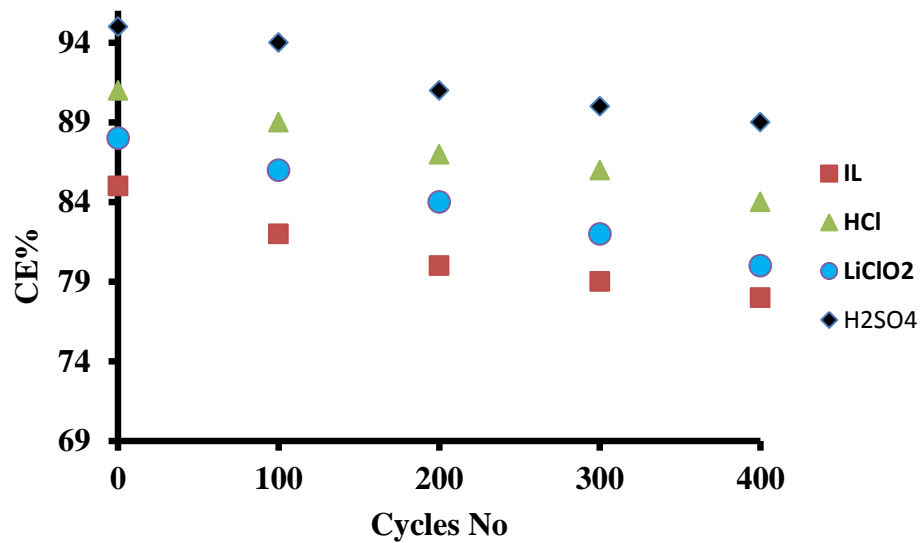


Figure 73. CE% of G-PEDOT nanocomposites versus cycles numbers in (a) 2M HCl (b) 2M H₂SO₄ (c) LiClO₄ (d) IL.

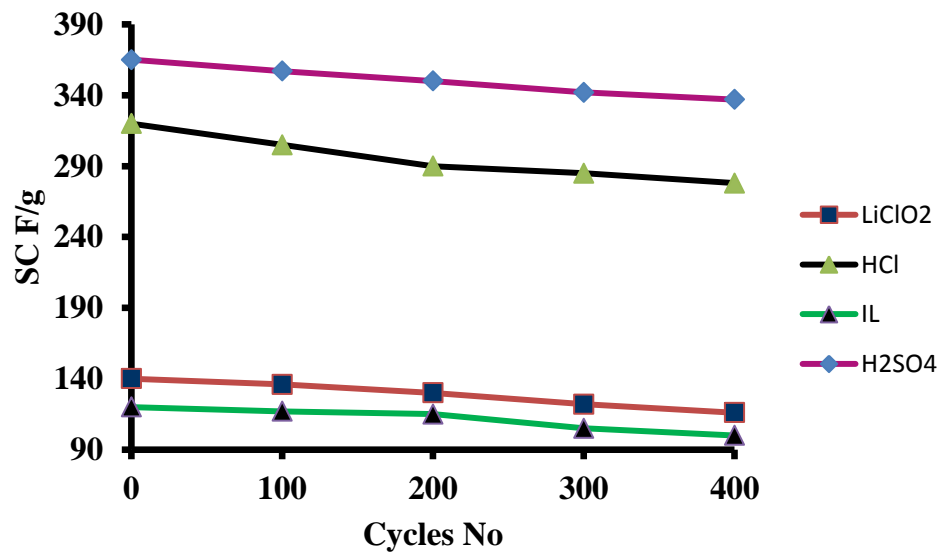


Figure 74. Specific capacitance versus scan rate of G-PEDOT nanocomposites in (a) 2M HCl (b) 2M H₂SO₄ (c) LiClO₄ (d) IL.

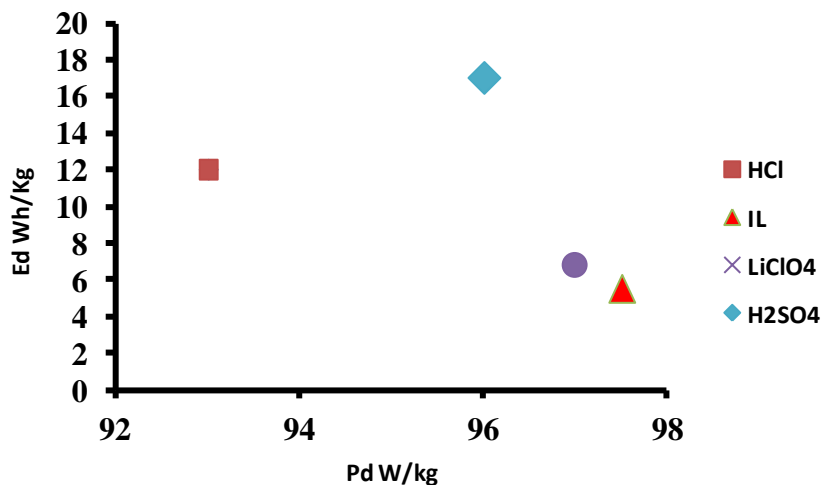


Figure 75. Ragone plot of G-PEDOT nanocomposites in (a) 2M HCl (b) 2M H₂SO₄ (c) LiClO₄ (d) IL.

In addition to CV and chronopotentiometry results, the capacitive behavior of G-PEDOT electrodes was also estimated using impedance spectroscopy technique in a frequency range of 100 mHz to 100 KHz. Figure 76 shows the impedance comparison of G-PEDOT in HCl, H₂SO₄, LiClO₄, and IL electrolytes. The bulk electrical conductivity at the interface of electrode/electrolyte solution could be evaluated by EIS method. The EIS analysis is taken into account, to estimate the fundamental behavior of electrode material for a supercapacitor. An AC impedance spectrum has shown to influence in all three high, medium and low frequency regions.

A small semicircle arc and a straight line are observed besides the interfacial polarization effect in Nyquist plots. The faradic reaction across the electrode and electrolyte ions is responsible for the formation of the semicircle in high frequency. Whereas in medium and low frequencies, pseudo-transfer resistance is responsible for the formation of a semicircle pattern and inclined slope, associated mainly with the porosity

and conductivity of the electrodes. For instance a fast doping/dedoping process due to redox reactions in G-PEDOT-based supercapacitor exhibits good capacitive behavior. The transport of electrons or holes in addition to ionic transport originates the doping/dedoping process in a polymer based supercapacitor. Ion transport is important since it determines the charge-discharge capacity of a supercapacitor [114]. The G-PEDOT nanocomposites in HCl presents a phase angle close to 90 degrees in a high frequency region, following the trend of ideal capacitive behavior, and agrees to CV results. The improvement in the proton diffusion into the G-PEDOT nanocomposites electrode during the charge storage/delivery process is due to the incorporation of graphene in the PEDOT matrix [122].

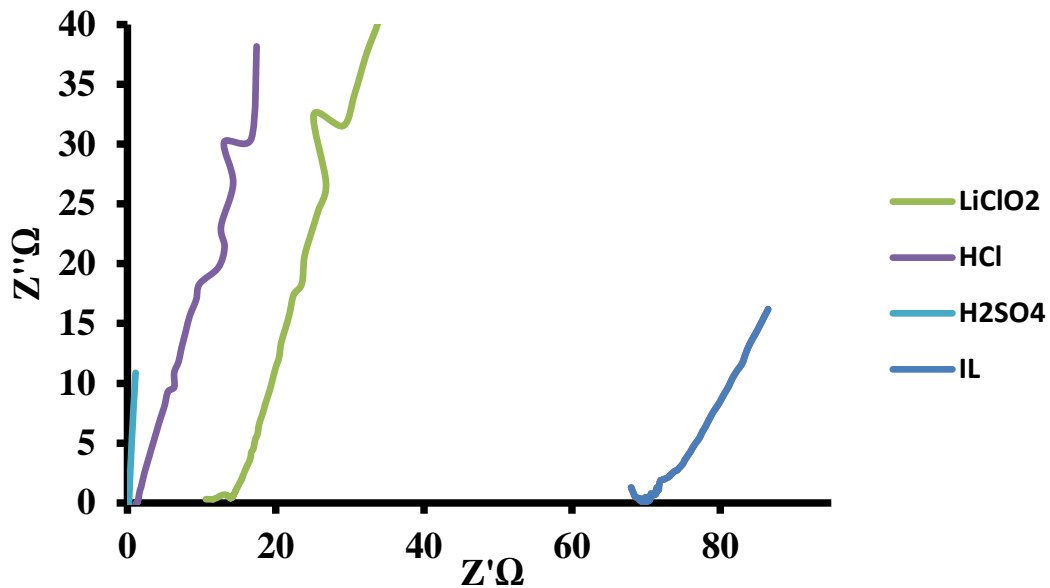


Figure 76. Impedance analysis of G-PEDOT nanocomposites in (a) 2MHCl (b) 2MH₂SO₄ (c) LiClO₄ (d) IL.

The above discussion clearly supports the importance of electrolytes in the supercapacitor in order to improve the specific capacitance to obtain the best performance of the supercapacitor. Here we have made an attempt to understand the rapid response of the interface electrode potential and high reversibility in the G-PEDOT EDLC system.

6.4 Summary

G-PEDOT nanocomposites material is synthesized using an oxidative polymerization technique. The FTIR and Raman studies of G-PEDOT films have shown that G not only makes the nanocomposites material but also acts as a dopant to the PEDOT system. The G-PEDOT compact morphology enhances the electrochemical performance dramatically in a PEDOT based supercapacitor. The G-PEDOT has provided a faster electrochemical reaction with an average capacity of 380 F/g in HCl medium. However, except for HCl, G-PEDOT also shows the good capacitive behavior in organic and ionic liquid electrolytes. The electrochemical performance of the G-PEDOT based supercapacitor could be further enhanced by optimizing the electrolyte role, electrode material, and cell design. This study provides the fundamental understanding for high performance organic electronic devices of G and PEDOT based nanocomposite electrode material.

CHAPTER 7: CONCLUSION

The objective of this doctoral study was to explore the role and deepen the knowledge of the nanocomposites materials regarding its electrochemical properties used as supercapacitor electrodes. In order to understand the role of nanocomposites in detail they were studied by means of physical, structural and electrochemical approaches. The nanocomposites show several advantages used as the supercapacitor electrode due to the high surface area, large flexibility, high reactivity and shorter ionic diffusion paths. The main advantage of the graphene based nanocomposites material is high conductivity which tailors the electron transport within the electrode material and enhances the cycle life and high rate capability. Following is the summary of the outcomes related to nanocomposites research discussed in this doctoral dissertation.

7.1 Electrochemical Capacitor

The main aspect of this research is to explore the synergetic effect of nanocomposites in order to analyze the performance of the electrochemical capacitor. The selection of stable and widely used conducting polymers were made to see their potential in the enhancement of the efficiency and stability of the supercapacitor. During this research, the effect of aromatic conducting polymer nanocomposites with the selection of several inorganic materials has been studied and tested. The most notable aromatic conducting polymer nanocomposites used in present research work are ZnO-

PANI, RuO₂-PANI, G/ZnO-PANI and G-PANI. For instance, almost all synthesized C-Ps nanocomposites have shown great potential to be used as fast supercapacitor electrodes. However the high theoretical capacity, larger surface area, higher flexibility, low cost and superior electrochemical properties of graphene has rendered the best results of G-PANI among other nanocomposites materials.

Moreover, the amount of graphene plays a key role in the enhancement of the overall synergetic effect of synthesized material. The detailed investigation has been made by adding the different proportions of graphene to the monomer weight percent as discussed in chapter 3rd. Based on the obtained results, it has been realized that equal weight percent ratio of graphene to monomer has provided the optimum result in terms of electronic and ionic conductivity, reliability, and specific capacitance of the supercapacitor. Contrary to the concept of high electronic conductivity, it is evident that beyond a certain limit the electronic conductivity does not play any significant role in the performance enhancement of the supercapacitor since there are many other reasons, to obtain overall performance of a device.

In addition to the amount of graphene, other important parameters are also examined during this research to evaluate and analyze their influence in the performance of a device. Since the formation of the electric double layer depends on the surface area and morphology of the electrode material, the optimum electrode thickness is very essential to obtain efficient working device. Here three random thicknesses of G-PANI nanocomposites which involve 10 μ m, 30 μ m and 50 μ m were selected to observe their electrochemical behavior. Among these three thicknesses, 30 μ m electrode has shown promising results with the highest specific capacitance and the improved electroactive

and electrochemical response. Thus, on the basis of thicknesses comparison it has been concluded that appropriate surface area or film thickness is a highly significant factor to increasing the width of the electric double layer and, therefore, preventing the degradation of the device.

Furthermore, the nature of electrolytes and packing of electrolytes are of utmost importance to achieving improvement in the energy density and power density of the electrochemical capacitor. In order to get the comprehensive idea of the electrolyte role in the supercapacitor, the three most widely used electrolytes are acidic solution (H_2SO_4), organic electrolyte ($LiClO_4$), and room temperature ionic liquid IL. These were selected and tested as explained in chapter 4. Since having different ionic conductivity and permittivity of electrolytes, it has been noted that the acidic electrolyte has provided the maximum energy density with a reasonable power density due to less diffusion limitations and high conductivity. Whereas the trend of maximum power density has been observed in ionic liquid due to high decomposition voltage range. Thus, following the advantages and disadvantages of electrolytes it has been found that an acidic electrolyte, with a smaller ionic size and higher electroactive characteristic is one of the favorite choices of electrolytes to achieve the maximum output of the device. However, the low evaporation rate and the lesser corrosion risk factor of the organic electrolyte and ionic liquid have shown improvement in the stability and life of the device.

During this research the concentration of electrolyte and effect of solvent was also discussed in chapter 4. In order to see the influence of electrolyte concentration, the electrochemical measurements were performed for different concentrations and later it was concluded that the presence of an optimal amount of ions in electrolytes is very

important, not only to improve the conductivity of electrolytes, but it also helps in increasing the electric double layer capacity due to the reasonable width formation of the electric double layer. Nevertheless, too less and too high of an electrolyte concentration may degrade the device performance.

Further the solubility impact of solvents for graphene-polyaniline nanocomposites was also investigated to improve the durability and output of the device. Among the selection of the three most favorable solvents for aromatic polymers which are: NMP, Nafion and DMF. The NMP has shown the maximum solubility and least grain boundaries, which leads to the fabrication of fast and reliable electrochemical capacitor. Detailed comparative electrochemical study of widely known and stable conducting polymers involves Polyaniline, Polythiophene and Poly (3, 4-ethylenedioxythiophenes) has been established to understand their reaction kinetics. By comparison, the Graphene nanocomposites of Polyaniline, Polythiophene and Poly (3, 4-ethylenedioxythiophenes) have shown the reasonable specific capacitance for the electrochemical device. However, the maximum efficiency and specific capacitance are examined for G-PANI and G-PEDOT nanocomposites. This clearly demonstrates the higher atmosphere stability, higher conductivity, superior structural hierarchy and faster reaction kinetics of the Polyaniline and Poly (3, 4-ethylenedioxythiophenes).

7.2 Future Work and Limitations

The nanocomposites materials have advantages to being used in supercapacitor electrodes in the commercial sector. I have studied the synthesis of nanomaterials, fabrication of supercapacitor cell, the charging and discharging cycles and specific capacitance in detail over several important nanocomposites materials. I have observed

that the larger surface area and small particle size, in nanocomposites systems leads to higher reactivity due to excessive side reactions with the electrolyte. Therefore, it is important to control the shape as well as the size of nanocomposites during synthesis. Besides the correct size of the particles, the surface modification of the synthesized material should be investigated to prevent the disadvantages of nanocomposites and enhance the overall performance of the device.

However, in order to fabricate durable, flexible electrochemical capacitors in addition to acidic, organic and ionic liquid, the further use of solid state electrolytes needs to be explored. Moreover, to reduce the amount of leakage current and to enhance the capacity retention in the electrochemical capacitor, the use of high k dielectric will be beneficial. Further, the investigation related to micro contacts research should be anticipated to reduce the equivalent series resistance of the device and improve the overall efficiency and performance of the device.

REFERENCES

- [1] R. Katz and M. Carlen, "Principles and applications of electrochemical capacitor" *Electrochimica Acta*, Vol 45 (2000) p2483.
- [2] <http://en.wikipedia.org/wiki/Electricdouble-layercapacitor>.
- [3] C. C. Lin and C. L. Yang, "Carbon nanotubes grown on nanoporous alumina templates/aluminum foil for electrodes of aluminum electrolytic capacitors" *Journal of Electrochemical Society*, 157(2010) A237.
- [4] http://en.wikipedia.org/wiki/Electrolytic_capacitor
- [5] <http://electronics.howstuffworks.com/capacitor.htm>
- [6] <http://energyphysics.wikispaces.com/Ultracapacitors>.
- [7] H. E. Becker. U.S. Patent 2800 616, 1957.
- [8] D. I. Boos. U.S. Patent 3 536 963, 1970.
- [9] B. E. Conway. "Transition from supercapacitor to battery behavior in electrochemical energy storage" *Journal of Electrochemical Society*, 138(1991)1539.
- [10] W. Shi, J. Zhu, D. J. Kharistal, W. Zhao, B. S. Lalia, H. H. Hng, and Q. Yan, "High-power and high-energy-density flexible pseudocapacitor electrodes made from porous CuO nanobelts and single-walled carbon nanotubes" *ACS Nano*, 5(2011)2013.
- [11] C. C. Hu, K. H. Chang, M.C. Lin, and Y. T. Wu, "Design and tailoring of the nanotubular arrayed architecture of hydrous RuO₂ for next generation supercapacitors" *Nano Letters*, 6(2006)2690.
- [12] http://batteryuniversity.com/learn/article/whats_the_role_of_the_supercapacitor.
- [13] A. Schneuwly and R. Gallay, "Properties and applications of supercapacitors from the state-of-the-art to future trends" *PCIM Proceedings Europe Official Proceedings of the Forty-First International Power Conversion Conference*,(2000)115.

- [14] B. E. Conway and E. Gileadi “Steady state theory of adsorption pseudocapacitance in electrochemical radical-ion reactions” *Canadian Journal of Chemistry*, 42(1964).
- [15] B.E. Conway, V. Birss and J. Wojtowicz, “The role and utilization of pseudocapacitance for energy storage by supercapacitors” *J. Power Source*, 66(1997)1.
- [16] J. Huang, B.G. Sumpter, and V. Meunier, “A universal model for nanoporous carbon supercapacitors applicable to diverse pore regimes, carbon materials, and electrolytes” *Chem. Eur. J.* 14(2008)6614.
- [17] P .W. Ruch, R. Kötz and A. Wokaun “Electrochemical characterization of single-walled carbon nanotubes for electrochemical double layer capacitors using non-aqueous electrolyte” *Electrochimica Acta* ,54(2009)4451.
- [18] A. Braun, M. Bartsch, O. Merlo, B. Schnyder, B. Schaffner, R. Kotz , O. Haas and A. Wokaun, “Exponential growth of electrochemical double layer capacitance in glassy carbon during thermal oxidation” *Carbon* , 41(2003)759.
- [19] J. P. Valleau and G. M. Torrie, “The electrical double layer. III. Modified gouy chapman theory with unequal ion sizes” *J. Chem. Phys*, 76(1982)4623.
- [20] J. P. Zheng, J. Huang and T.R. Jow, “The limitations of energy density for electrochemical capacitors” *Journal of Electrochemical Society*, 144(1997)2026.
- [21] N. Georgi, A.A. Kornyshev and M.V. Fedorov “The anatomy of the double layer and capacitance in ionic liquids with anisotropic ions” *Journal of Electroanalytical Chemistry*, 649(2010)261.
- [22] D.C. Grahame. “The electrical double layer and the theory of electrocapillarity” *Chem. Rev*, 4(1947)441.
- [23] B. E .Conway and W. G .Pell, “Double-layer and pseudocapacitance types of electrochemical capacitors and their applications to the development of hybrid devices” *Journal of Solid State Electrochemistry*, 7(2003)637.
- [24] G. Feng, “Molecular physics of electrical double layers in electrochemical capacitors” dissertation, Clemson University, December 2010.
- [25] A. Rudge, J. Davey, I. Raistrick, S. Gottesfeld and J. P. Ferraris, “Conducting polymers as active materials in electrochemical capacitors” *J. Power Source*, 47(1994)89.
- [26] H. J. Ahonen, J. Lukkari, and J. Kankare, “N- and p-doped Poly (3ethylenedioxythiophene) two electronically states of the polymer” *Macromolecules*, 33(2000)6787.

- [27] J. Liu, J. Essner and J. Li, "Hybrid supercapacitor based on coaxially coated manganese oxide on vertically aligned carbon nanofiber arrays" *Chem. Mater.*, 22(2010)5022.
- [28] I. Hadjipaschalis, A. Poullikkas and V. Efthimiou, "Overview of current and future energy storage technologies for electric power applications" *Renewable and Sustainable Energy Reviews*, 13(2009)1513.
- [29] M. Eikerling, A. A. Kornyshev, and E. Lust, "Optimized structure of nanoporous carbon-based double-layer capacitors" *Journal of Electrochemical Society*, 152(2005)1-E24.
- [30] A. K. Geim and K. S. Novoselov, "The rise of graphene" *Nat.Mater.*, 6(2007)183.
- [31] Y. Tian, J. W. Yan, R. Xue, and B. Yi, "Capacitive properties of activated carbon in $K_4Fe(CN)_6$ " *Journal of Electrochemical Society*, 158(2011)A818.
- [32] X. Y. Zhao, J. P. Cao, K. Morishita, J. I. Ozaki and T. Takarada, "Electric double-layer capacitors from activated carbon derived from black liquor" *Energy Fuels*, 24(2010)1889.
- [33] D. Qu and H. Shi, "Studies of activated carbons used in double-layer capacitors" *J. Power Source*, 74(1998)99.
- [34] E. Frackowiak and F. Beguin, "Carbon materials for the electrochemical storage of energy in capacitors" *Carbon*, 39(2001)937.
- [35] R. Saliger, U. Fischer, C. Herta, and J. Fricke, "High surface area carbon aerogels for supercapacitors" *Journal of Non-Crystalline Solids*, 225(1998)81.
- [36] <http://en.wikipedia.org/wiki/Carbon-nanotube>.
- [37] C. Emmenegger, P. Mauron, P. Sudan, P. Wenger, V. Herman, R. Gallay and A. Züttel, "Investigation of electrochemical double layer (ECDL) capacitors electrodes based on carbon nanotubes and activated carbon materials" *J. Power Source*, 124(2003)321.
- [38] A. I. Najafabadi, T. Yamada, D. N. Futaba, M. Yudasaka, H. Takagi, H. Hatori, S. Iijima, and K. Hata, "High-power supercapacitor electrodes from single-walled carbon nanohorn/nanotube composite" *ACS Nano*, 5(2011)811.
- [39] J. R. McDonough, J. W. Choi, Y. Yang, F. L. Mantia, Y. Zhang, and Y. Cui, "Carbon nanofiber supercapacitors with large areal capacitances" *Applied Physics Letters*, 95(2009)243109.
- [40] S. R. C. Vivekchand, C. S. Rout, K. S. Subrahmanyam, A. G. Raj and C. N. R. Rao, "Graphene-based electrochemical supercapacitors" *J. Chem. Sci.*, 120(2008)9.

- [41] J. P. Zheng, P. J. Cygan, and T. R. Jow, "Hydrous ruthenium oxide as an electrode material for electrochemical capacitors" *Journal of Electrochemical Society*, 142(1995)2699.
- [42] W. Sugimoto, H. Iwata and K. Yokoshima, "Proton and electron conductivity in hydrous ruthenium oxides evaluated by electrochemical impedance spectroscopy" *J. Phys.Chem. B*, 109(2005)07330.
- [43] C. C. Hu and T. W. Tsou. "Ideal capacitive behavior of hydrous manganese oxide prepared by anodic deposition" *ElectrochemCommun*, 4(2002)105.
- [44] E. Frackowiak, V. Khomenko, K. Jurewicz, K. Lota and F. Béguin, "Supercapacitors based on conducting polymers/nanotubes composites" *J. Power Source*, 153(2006)413.
- [45] M. Graeme, B.Supes, A. Deore, S. Michael and S. Freund, "Porous conducting polymer/heteropolyoxometalate hybrid material for electrochemical supercapacitor applications" *Langmuir*, 24(2008)1064.
- [46] N. Gospodinova and L. Terlemezyan, "Conducting polymers prepared by oxidative polymerization polyaniline" *Prog. Polym.Sci*, 23(1998)1443.
- [47] M.E. G. Lyons, H. G. Fay, T. McCabe and J. Corish. "Charge percolation in electroactive polymer films" *J. Chem.Soc. Faraday Trans*, 86(1990)2905.
- [48] S. Bhadra, D. Khastgir, K. N. Singha, and H. J. Lee, "Progress in preparation, processing and applications of polyaniline" *Prog. Polym. Sci*, 34(2009)783.
- [49] J. X. Huang and R. B. Kaner, "Nanofiber formation in the chemical polymerization of aniline" *Angew. Chem*, 43(2004)5817.
- [50] J. Jang, M. Bae S. Choi and H. Yoon, "Fabrication and characterization of polyaniline coated carbon nanofiber for supercapacitor" *Carbon*, 43(2005)2730.
- [51] J. X. Huang and R. B. Kaner, "A general chemical route to polyaniline nanofibers" *J. Am. Chem. Soc*, 126(2004)851.
- [52] H. Gómez, M. K. Ram, F. Alvi, P. Villalba, E. Stefanakos and A. Kumar, "Graphene-conducting polymer nanocomposite as novel electrode for supercapacitors" *J. Power Source*, 196(2011)4102.
- [53] O. Monticelli, Z. Musina, S. Russo and S. Bals, "On the use of TEM in the characterization of nanocomposites" *Materials Letters*, 61(2007)3446.

- [54] D. A. Dikin, K. M. Kohlhaas, G. H. B. Dommett, S. Stankovich and R. S. Ruoff, "Scanning electron microscopy methods for analysis of polymer nanocomposites" *Microscopy and Microanalysis*, 12(2006)674.
- [55] M. K. Ram, E. Maccioni and C. Nicolini, "The electrochromic response of polyaniline and its copolymeric systems" *Thin Solid Films*, 303(1997)27.
- [56] J. B. M. Krishna, A. Saha, G. S. Okram, A. Soni, S. Purakayastha and B. Ghosh, "Electrical properties of polyaniline doped with metal ions" *J. Phys. D.* 42(2009)095404.
- [57] J. Yan, T. Wei, T.B. Shao, B.Z. Fan, Z.W. Qian, M. Zhang, and F. Wei, "Preparation of a graphene nanosheet/polyaniline composite with high specific capacitance" *Carbon*, 48(2010)487.
- [58] S. L. Patil, S. G. Pawar, M. A. Chougule, B.T. Raut, V. S. Karande, R. N. Mulik and V. B. Patil, "PANI- ZnO nanocomposites: synthesis and characterization" *Applied Physics Letters*, 1391(2011)621.
- [59] F. Alvi, M. K. Ram, H. Gomez, R. K. Joshi and A. Kumar "Evaluating the chemio-physio properties of novel zinc oxide-polyaniline nanocomposite polymer films" *Polymer Journal*, 42(2010)935.
- [60] L. j. Meng, V. Teixeira and M. P. d. Santos, "Raman spectroscopy analysis of magnetron sputtered RuO₂ thin films" *Thin Solid Films*, 442(2003)93.
- [61] J. Zhang, L. B. Kong, Wang, Y.C. Luo and L. Kang, "In-situ electrochemical polymerization of multi-walled carbon nanotube/polyaniline composite films for electrochemical supercapacitors" *Synthetic Metals*, 159(2009)260.
- [62] L. Li, H. Song, Q. Zhang, J. Yao and X. Chen. "Effect of compounding process on the structure and electrochemical properties of ordered mesoporous carbon/polyaniline composites as electrodes for supercapacitors" *J. Power Source*, 187(2009)268.
- [63] A. S. Sarac, M. Ates and B. Kilic, " Electrochemical impedance spectroscopic study of polyaniline on platinum, glassy carbon and carbon fiber microelectrodes" *Int. J. Electrochem Sci.* 3(2008)777.
- [64] D.W. Wang, F. Li, P. J. Zhao, C.W. Ren, G. Z. Chen, J. Tan, S. Z. Wu, I. Gentle, Q. G. Lu and M. H. Cheng, "Fabrication of graphene/polyaniline composite paper via in situ anodic electropolymerization for high-performance flexible electrode" *ACS Nano*, 3(2009)1745.
- [65] L. L. Zhang, S. Li, J. Zhang, P. Guo, J. Zheng and X. S. Zhao, "Enhancement of electrochemical performance of macroporous carbon by surface coating of polyaniline" *Chem. Mater.* 22(2010)1195.

- [66] Y. Wang, Z. Shi, Y. Huang, Y. Ma, C. Wang, M. Chen and Y. Chen, "Supercapacitor devices based on graphene materials" *J. Phys. Chem.C*, 113(2009)13103.
- [67] H. Mi, X. Zhang, S. Yang, X. Ye, J. Luo, "Polyaniline nanofibers as the electrode material for supercapacitors" *Materials Chemistry and Physics*, 112(2008)127.
- [68] H. Bai, X. Y. Xu, L. Zhao, C. Li and Q.G. Shi, "Non-covalent functionalization of graphene sheets by sulfonated polyaniline" *Chem. Commun.* (2009)1667.
- [69] C. N. R. Rao, K. Biswas, K.S. Subrahmanyam and A. Govindaraj, "Graphene, the new nanocarbon" *J. Mater. Chem*, 19(2009)2457.
- [70] H. Wang, Q. Hao, X. Yang, L. Lu and X. Wang, "Graphene oxide doped polyaniline for supercapacitors" *Electrochem. Commun*, 11(2009)1158.
- [71] S. Stankovich, D.A. Dikin, R. D. Piner K. A. Kohlhaas, A. Kleinhammes, Y. Jia, Y. Wu, S. T. Nguyen and R. S. Ruoff, "Synthesis of graphene-based nanosheets via chemical reduction of exfoliated graphite oxide" *Carbon*, 45(2007)1558.
- [72] S. E. Bourdo and T. Viswanathan, "Graphite/polyaniline (GP) composites: synthesis and characterization" *Carbon*, 43(2005)2983.
- [73] G. Wang, Z. Yang, X. Li and C. Li, "Synthesis of poly(aniline-co-o-anisidine)-intercalated graphite oxide composite by delamination/reassembling method" *Carbon*, 43(2005)2564.
- [74] K. Zhang, L. L. Zhang, X. S. Zhao, and J. Wu, "Graphene/Polyaniline nanofiber composites as supercapacitor electrodes" *Chem. Mater.* 22(2010)1392.
- [75] M. Baibarac, I. Baltog and S. Lefrant, "Photoluminescence and raman spectroscopy studies on polyaniline/PbI₂ composite" *Journal of Solid State Chemistry*, 182(2009)827.
- [76] A. C. Ferrari, J. C. Meyer, V. Scardaci, C. Casiraghi, M. Lazzeri, F. Mauri, S. Piscanec, D. Jiang, K. S. Novoselov, S. Roth and A. K. Geim, "Raman spectrum of graphene and graphene layers" *Physical review letters*, 97(2006)187401.
- [77] L. Mao, K. Zhang, H.S. O. Chan and J. Wu, "Surfactant-stabilized graphene/polyaniline nanofiber composites for high performance supercapacitor electrode" *J. Mater. Chem*, 22(2012)80.
- [78] A. Yu, I. Roes, A. Davies, and Z. Chen, "Ultrathin, transparent, and flexible graphene films for supercapacitor application" *Applied Physics Letters*, 96(2010)253105.

- [79] T.Y. Kim, H. W. Lee, M. Stoller, D. R. Dreyer, C.W. Bielawski, R.S. Ruoff, and K. S. Suh, "High-performance supercapacitors based on poly (ionic liquid)-modified graphene electrodes" *ACS Nano*, 5(2011)436.
- [80] H. An, Y. Wang, X. Wang, N. Li and L. Zheng, "The preparation of PANI/CA composite electrode material for supercapacitors and its electrochemical performance" *J Solid State Electrochem*, 14(2010)651.
- [81] Q. Wu, Y. Xu, Z. Yao, A. Liu and G. Shi, "Supercapacitors based on flexible graphene/polyaniline nanofiber composite films" *ACS Nano*, 4(2010)1963.
- [82] A. L.M. Reddy, F. E. Amitha, I. Jafri and S. Ramaprabhu, "Asymmetric flexible supercapacitor stack" *Nanoscale Res Lett*, 3(2008)145.
- [83] P. Kurzweil and M. Chwistek "Electrochemical stability of organic electrolytes in supercapacitors: Spectroscopy and gas analysis of decomposition products" *J. Power Source*, 176(2008)555.
- [84] Y. Chen, X. Zhang, D. Zhang and Y. Ma, "High power density of graphene-based supercapacitors in ionic liquid electrolytes" *Materials Letters*, 68(2012)475.
- [85] Y. Yin, "An experimental study on PEO polymer electrolyte based all-solid-state supercapacitor" dissertation, University of Miami, 2010-06-25.
- [86] Q. Cheng, J. Tang, J. Ma, H. Zhang, N. Shinya, and L.C. Qin, "Polyaniline-coated electro-etched carbon fiber cloth electrodes for supercapacitors" *Journal of Physical Chemistry C*,(2011).
- [87] T. C. Girija and M. V. Sangaranarayanan, "Investigation of polyaniline-coated stainless steel electrodes for electrochemical supercapacitors" *Synthetic Metals*, 156(2006)244.
- [88] X. M. Feng, R. M. Li, Y.W. Ma, R. F. Chen, N.E. Shi, Q. L. Fan and W. Huang, "One-Step electrochemical synthesis of graphene/polyaniline composite film and its applications" *Adv. Funct. Mater*, 21(2011)2989.
- [89] Y. Chen, X. Zhang, D. Zhang, P. Yu and Y. Ma, "High performance supercapacitors based on reduced graphene oxide in aqueous and ionic liquid electrolytes" *Carbon*, 49(2011)573.
- [90] W. Lu, K. Henry, C. Turchi and J. Pellegrino, "Incorporating ionic liquid electrolytes into polymer gels for Solid-state ultracapacitors" *Journal of Electrochemical Society*, 155(2008)A361.
- [91] E. Frackowiak, G. Lota, and J. Pernak, "Room-temperature phosphonium ionic liquids for supercapacitor application" *Applied Physics Letters*, 86(2005)164104.

- [92] C. Liu, Z. Yu, D. Neff, A. Zhamu, and B. Z. Jang, "Graphene-based supercapacitor with an ultrahigh energy density" *Nano Letters*, 10(2010)4863.
- [93] P. Kurzweil and H.J. Fischle, "A new monitoring method for electrochemical aggregates by impedance spectroscopy" *J. of Power Source*, 127(2004)331.
- [94] M. Yang, B. Cheng and H. Song, X. Chen, "Preparation and electrochemical performance of polyaniline-based carbon nanotubes as electrode material for supercapacitor" *Electrochimica Acta*, 55(2010)7021.
- [95] A. B. Afzal, M. J. Akhtar, M. Nadeem, M. Ahmad, M.M .Hassan, T. Yasin and M. Mehmood. "Structural and electrical properties of polyaniline/silver nanocomposites" *J. Phys. D.* 42(2009)015411.
- [96] A. D. Marani and A.A. Entezami, "New synthesis method of polythiophenes" *iranian journal of polymer science and technology*, 3(1994)2.
- [97] S. R. P. Gnanakan, N. Muruganatham and A. Subramania, "Organic acid doped polythiophene nanoparticles as electrode material for redox supercapacitors" *Polym. Adv. Technol.* 22(2011)788.
- [98] F. Alvi, P.A. Basnayaka, M. K. Ram, H. Gomez, E. Stefanako, Y. Goswami and A. Kumar "Graphene-polythiophene nanocomposite as novel supercapacitor electrode material" *Journal of New Materials for Electrochemical Systems* 15(2012)2.
- [99] Q. Lu and Y. Zhou, "Synthesis of mesoporous polythiophene/MnO₂ nanocomposite and its enhanced pseudocapacitive properties" *J of Power Source*, 196(2011)4088.
- [100] T. Xiao, W. Cui, J. Andereg, J. Shinar and R. Shinar, "Simple routes for improving polythiophene:fullerene-based organic solar cells" *Organic Electronics*, 12(2011)257.
- [101] O. Bertran, E. Armelin, F. Estrany, A. Gomes, J. Torras and C.Aleman "Poly (2-thiophen-3-yl-malonic acid), a polythiophene with two carboxylic acids per repeating unit" *J. Phys. Chem. B*, 114(2010)6281.
- [102] N. Ballav and M. Biswas, "Preparation and evaluation of nanocomposites of polythiophene with Al₂O₃" *Polym Int*, 52(2003)179.
- [103] G. Shi, J. Xu, and M. Fu, "Raman spectroscopic and electrochemical studies on the doping level changes of polythiophene films during their electrochemical growth processes" *Journal of Physical Chemistry B*, 106(2001)288.
- [104] A. Acharya, R. Mishra, and G.S. Roy," Characterization of CdSe/Polythiophene nanocomposite by TGA/DTA, XRD, UV-Vis Spectroscopy, SEM-EDXA and FTIR, *Armenian Journal of Physics*, 3(2010)195.

- [105] A. U. O. Turkoglu, S. Sen, E. Ersoy, A. G. Yavuz and G. G. Batir, "The electrical conductivity properties of polythiophene/TiO₂ nanocomposites prepared in the presence of surfactants" *Current Applied Physics*, 9(2009)865.
- [106] H. M. Ju, S. H. Choi and S. H. Huh, "X-ray diffraction patterns of thermally-reduced graphene" *Journal of the Korean Physical Society*, 57(2010)1649.
- [107] S. R. P. Gnanakan, M. Rajasekhar and A. Subramania, "Synthesis of polythiophene nanoparticles by surfactant -assisted dilute polymerization method for high performance redox supercapacitors" *Int. J. Electrochem. Sci*, 4(2009)1289.
- [108] C. Y. Wang, A. M. Ballantyne, S.B. Hall, C.O. Too, D.L. Officer and G.G. Wallace, "Functionalized polythiophene-coated textile: A new anode material for a flexible battery" *J. Power Sources*, 156(2006)610.
- [109] M. F. S. Herrera and J. M. Feliu, "Electrochemical properties of thin films of polythiophene polymerized on basal plane platinum electrodes in nonaqueous media" *J. Phys. Chem. B*, 113(2009)1899.
- [110] H. Ding, Z. Pan, L. Pigani, R. Seeber and C. Zanardi, "An electrochemical impedance spectroscopy study, p- and n-doping processes in polythiophene with reduced bandgap" *Electrochimica Acta*, 46(2001)2721.
- [111] J. Vaillant, M. L. Cantu, K. C. Gallegos, N. C. Pastor and P. G. Romero, "Chemical synthesis of hybrid materials based on PANI and PEDOT with polyoxometalates for electrochemical supercapacitors" *Progress in Solid State Chemistry*, 34(2006)147.
- [112] R. Liu, S. Il. Cho and S. B. Lee, "Poly (3, 4-ethylenedioxythiophene) nanotubes as electrode materials for a high-powered supercapacitor" *Nanotechnology*, 19(2008)215710.
- [113] G. Greczynski, T. Kugler, M. Keil, W. Osikowicz, M. Fahlman and W.R. Salaneck, "Photoelectron spectroscopy of thin films of PEDOT-PSS conjugated polymer blend" *Journal of Electron Spectroscopy and Related Phenomena*, 121(2001)1.
- [114] F. Alvi, M. K. Ram, P. A. Basnayaka, E. Stefanakos, Y. Goswami and A. Kumar "Graphene-polyethylenedioxythiophene conducting polymer nanocomposite based supercapacitor" *Electrochimica Acta*, 56(2011)9406.
- [115] S. Patra and N. Munichandraiah "Supercapacitor studies of electrochemically deposited PEDOT on stainless steel substrate" *Journal of Applied Polymer Science*, 106 (2007)1160.
- [116] S. V. Selvaganesh, J. Mathiyarasu, K. L. N. Phani and V. Yegnaraman, "Chemical synthesis of PEDOT-Au nanocomposite" *Nanoscale Res Lett*, 2(2007)546.

- [117] L. Zhan, Z. Song, J. Zhang, J. Tang, H. Zhan, Y. Zhou and C. Zhan “PEDOT: cathode active material with high specific capacity in novel electrolyte system” *Electrochimica Acta*, 53(2008)8319.
- [118] S. Sakamoto, M. Okumura, Z. Zhao and Y. Furukawa, “Raman spectral changes of PEDOT-PSS in polymer light-emitting diodes upon operation” *Chemical Physics Letters*, 412(2005)395.
- [119] W. Feng, Y. Li, J. Wu, H. Noda, A. Fujii, M. Ozaki and K. Yoshino, “Improved electrical and optical properties of poly (3,4-ethylenedioxythiophene) via ordered microstructure” *J. Phys. Condens. Matter*, 19(2007)186220.
- [120] K. S. Ryu, Y. G. Lee, Y. S. Hong, Y. J. Park, X. Wu, K. M. Kim, M.G. Kang, N.G. Park and S. H. Chang, “Poly(ethylenedioxythiophene) (PEDOT) as polymer electrode in redox supercapacitor” *Electrochimica Acta*, 50(2004)843.
- [121] A. Laforgue, “All-textile flexible supercapacitors using electrospun poly (3,4-ethylenedioxythiophene) nanofibers” *J. Power Source*, 196(2011)559.
- [122] J. L. Duvail, P. Retho, S. Garreau, G. Louarn, C. Godon and S. D.Champagne, “Transport and vibrational properties of poly (3,4ethylenedioxythiophene) nanofibers” *Synthetic Metals*, 131(2002)123.

APPENDIX A: PERMISSIONS

Permission of journal of nature materials for Figure7 used in my dissertation.

NATURE PUBLISHING GROUP LICENSE TERMS AND CONDITIONS

Jul 05, 2012

This is a License Agreement between farah alvi ("You") and Nature Publishing Group ("Nature Publishing Group") provided by Copyright Clearance Center ("CCC"). The license consists of your order details, the terms and conditions provided by Nature Publishing Group, and the payment terms and conditions.

All payments must be made in full to CCC. For payment instructions, please see information listed at the bottom of this form.

License Number	2941991312875
License date	Jul 04, 2012
Licensed content publisher	Nature Publishing Group
Licensed content publication	Nature Materials
Licensed content title	The rise of graphene
Licensed content author	A. K. Geim, K. S. Novoselov
Licensed content date	Mar 1, 2007
Volume number	6
Issue number	3
Type of Use	reuse in a thesis/dissertation
Requestor type	academic/educational
Format	electronic
Portion	figures/tables/illustrations
Number of figures/tables/illustrations	1
High-res required	n/a
Figures	Figure 1: Mother of all graphitic forms. Graphene is a 2D building material for carbon materials of all other dimensionalities. It can be wrapped up into 0D buckyballs, rolled into 1D nanotubes or stacked into 3D graphite.
Author of this NPG article	no
Your reference number	
Title of your thesis / dissertation	Synthesis and Characterization of Nanocomposites for Electrochemical Capacitors
Expected completion date	Jul 2012
Estimated size (number of pages)	150
Total	0.00 USD